3-21-2013

Modeling the Thermosphere as a Driven-Dissipative Thermodynamic System

William R. Frey

Follow this and additional works at: https://scholar.afit.edu/etd

Part of the Physics Commons

MODELING THE THERMOSPHERE AS A DRIVEN-DISSIPATIVE THERMODYNAMIC SYSTEM

THESIS

William R. Frey, Captain, USAF

AFIT-ENP-13-M-11

DEPARTMENT OF THE AIR FORCE
AIR UNIVERSITY

AIR FORCE INSTITUTE OF TECHNOLOGY

Wright-Patterson Air Force Base, Ohio

AFIT-ENP-13-M-11

MODELING THE THERMOSPHERE AS A DRIVEN-DISSIPATIVE THERMODYNAMIC SYSTEM

THESIS

Presented to the Faculty

Department of Engineering Physics

Graduate School of Engineering and Management

Air Force Institute of Technology

Air University

Air Education and Training Command

In Partial Fulfillment of the Requirements for the

Degree of Master of Science in Applied Physics

William R. Frey, BS, MA

Captain, USAF

March 2013

MODELING THE THERMOSPHERE AS A DRIVEN-DISSIPATIVE THERMODYNAMIC SYSTEM

William R. Frey, BS, MA
Captain, USAF

Approved:

_____   4 Mar 13
Matthew B. Garvin, Capt, PhD (Chairman)   Date

_____   7 MAR 13
Ariel O. Acebal, Lt Col, PhD (Member)   Date

_____   6 Mar 13
Chin S. Lin, PhD, AFRL (Member)   Date

Abstract

Thermospheric density impacts satellite position and lifetime through atmospheric drag. More accurate specification of thermospheric temperature, a key input to current models such as the High Accuracy Satellite Drag Model (HASDM), can decrease model density errors. This thesis builds on Burke et al.'s driven-dissipative model (2009) to model the arithmetic mean temperature, $T_{1/2}$, defined by the Jacchia, 1977 model (J77), using the magnetospheric electric field as a driver. Three methods of treating the UV contribution to $T_{1/2}$ ($T_{1/2UV}$) are tested. Two model parameters, the coupling and relaxation constants, are adjusted for 38 storms from 2002 - 2008 to minimize modeled $T_{1/2}$ errors. Observed $T_{1/2}$ values are derived from densities and heights measured by the GRACE satellite. It is found that allowing $T_{1/2\,UV}$ to vary produces the lowest errors for 27 of 38 storms in the sample and 27 of 28 storms with decreasing UV contributions over the storm period. Treating $T_{1/2UV}$ as a constant produces the lowest errors for 7 of 10 storms with increasing UV contributions. The coupling and relaxation constants were found to vary over the solar cycle and are fit well as quadratic functions of $\sqrt{F_{10.7a}}$. By using the J77 model to convert the model $T_{1/2}$ values to density values, the driven-dissipative model produces density errors slightly lower than HASDM storm time errors.

Acknowledgments

Thanks to Capt Garvin, my advisor, for all of his guidance and insight throughout this process. I would also like to thank my committee members. Without Dr. Chin Lin this work would not have been possible. As a subject matter expert he answered all of my questions, provided me with or helped me to find all needed data, and helped me determine if my results were reasonable. Lt Col Acebal was also very helpful, most notably in pointing me towards some research dealing with the 2008 solar minimum as a possible explanation for some of my density results. Finally, I would like to thank my wife who still loves me even after listening to my hour-long defense presentation on 10 consecutive days.

<div align="right">William R. Frey, Capt, USAF</div>

Table of Contents

List of Figures

List of Tables

MODELING THE THERMOSPHERE AS A DRIVEN-DISSIPATIVE

THERMODYNAMIC SYSTEM

I. Introduction

Motivation

The thermosphere is defined as the neutral part of the Earth's upper atmosphere from roughly 95 – 1000 km above sea level. Hundreds of Department of Defense and other low-Earth orbit satellites operate at these altitudes. The ability to accurately characterize the thermospheric environment is critical in an era when the Department of Defense's dependence on satellites for communications, intelligence and other capabilities has never been higher. Likewise as the thermosphere becomes more crowded with low-Earth orbit satellites and space debris the consequences of inaccurate forecasts are becoming more significant. Several recent events illustrate these consequences. The destruction of the defunct Feng Yun 1C satellite by an anti-satellite weapons test in January, 2007 resulted in more than 2500 new pieces of debris in low earth orbit (Burke, et al., 2009). The risk posed to operational satellites by space debris was illustrated in 2009 when the Iridium 33 satellite was destroyed by a collision with the non-operational Cosmos 2251 satellite (Burke, et al., 2010). There have been several instances, such as 12 March and 1 December, 2009, where the risk of collision with debris has forced the crew of the International Space Station to take emergency actions to ensure their safety

(Weimer, et al., 2011). Improved characterization of the thermospheric environment is necessary to increase space object tracking accuracy and allow satellite operators and manned spaceflight missions to anticipate and avoid collisions (Wright, 2007).

Satellite Drag

Variations in thermospheric density impact satellite orbit trajectories through increased drag. The acceleration due to atmospheric drag is given by

$$a_{drag} = C_D \left(\frac{A_{sc}}{M_{sc}} \right) \rho V^2 \tag{1}$$

where A_{sc} and M_{sc} are the cross-sectional area and mass of the spacecraft, respectively, ρ is the neutral mass density of the atmosphere, and V is the spacecraft velocity relative to the neutral atmosphere. The drag coefficient C_D depends on the angle of flow to the spacecraft surface, the ratio of the temperatures of the spacecraft surface and the local atmosphere, and the ratio of the mean mass of atoms in the atmosphere to those on the spacecraft surface (Bruinsma and Biancale, 2003).

An increase in atmospheric drag decreases orbit altitude and increases orbit velocity. Thus, an inaccurate drag forecast will result in inaccurate position forecasts for satellites in low-earth orbit. In addition, increased drag over longer periods of time will decrease a satellite's operational lifetime by decreasing its orbit altitude until it experiences re-entry (Owens, et al., 2000). Accurate characterization of thermospheric density is necessary in the short term for accurate position modeling and in the long term for accurate satellite lifetime projections.

Thermospheric Density Measurements

Accurate and continuous measurements of thermospheric density have become readily available over the last 10 years from the Challenging Minisatellite Payload (CHAMP) (Bruinsma, et al., 2004) and Gravity Recovery and Climate Experiment (GRACE) (Tapley, et al., 2004) satellites. Densities are derived from on-board accelerometers that measure the electrostatic force needed to maintain a proof mass at the center of a cage located within 2 mm of the spacecraft's center of mass. Since the spacecraft and the proof mass respond to gravity in the same way, the changes in the electrostatic force needed to maintain the proof mass's position reflect the spacecraft's response to non-gravitational forces such as thermospheric drag (Bruinsma and Biancale, 2003). The availability of reliable in-situ thermospheric density measurements allows relevant comparisons with current modeled densities as well as "ground truth" data with which to test new methods of modeling the thermospheric environment.

Thermosphere as a Driven-Dissipative Thermodynamic System

One approach for modeling the thermosphere was developed by Burke et al., 2009 in which the thermosphere is assumed to be a driven-dissipative thermodynamic system. The term "driven-dissipative" simply describes the behavior of a system which gains energy from an input source, or "driver", but then contains a mechanism which dissipates the excess energy once the driver is lessened. This type of system is described by a differential equation of the same form as that governing the behavior of the disturbance storm time index (Dst), an index that monitors geomagnetic activity at low latitudes. The driven-dissipative approach uses empirical coupling and relaxation constants to model the

3

input of energy to the thermosphere from the solar wind during geomagnetic storms and the recovery of the thermosphere back to quiet conditions after the storm period, respectively. Values for these empirical constants were determined by Burke et al., 2009 by examining just two storm periods during 2004. Similar differential equations and constants can be used to model thermospheric energy, exospheric temperature, and Dst. Many existing thermospheric density models use exospheric temperature as a key input. By obtaining a predicted value of exospheric temperature from solar wind data, this approach seeks to provide a more accurate input for existing density models that can be linked to solar wind models to provide improved forecast capabilities.

Problem

While the driven-dissipative model approach of Burke et al., 2009 showed promising results when compared to observed data from GRACE, it was not applied to a large enough sample of storm events to establish its general applicability. In later work Burke, 2011 used the driven-dissipative model to establish coupling constants for 38 geomagnetic storms between 2002 and 2008. Burke's approach leaves several areas open to improvement. This thesis expands on the approach of Burke et al., 2009 in the following main areas:

1. Burke used two storms in 2004 to determine the value of the relaxation constant and did not allow it to vary for other storms. This value is suspect because Burke et. al, 2009 used an early version of GRACE data that has been replaced by a revised calibration (Burke, 2011) (Sutton, 2011). It is also likely that different storms will have different optimal relaxation constants. In addition, Burke used "trial and error

4

comparisons" (Burke, et al., 2009) to determine values for the coupling constant by attempting to generally align model results with the peak values in observed data. A more rigorous approach to determine the optimal values for both the coupling and relaxation constants is applied here.

2. Burke et al., 2009 treated energy input to the thermosphere from solar extreme ultra-violet (EUV) irradiance as a constant through each storm period. In this thesis, it is allowed to vary.

3. Burke used a simplified method of calculating observed orbit-averaged GRACE densities and exospheric temperatures (Burke, et al., 2009). In Burke's approach orbit-averaged values of density and height were calculated from raw GRACE measurements and then a quadratic fit to the Jacchia, 1977 model (J77) was applied to determine an orbit-averaged exospheric temperature. This thesis modifies the orbit-averaging technique and uses a different application of J77 to produce more physically accurate temperatures.

4. Burke modeled exospheric temperature but current thermospheric models use a global temperature parameter to model the EUV contribution to the thermospheric energy budget. J77 uses a parameter known as the arithmetic mean temperature, $T_{1/2}$. This thesis modifies Burke's approach to model the arithmetic mean temperature.

Overview

By modifying Burke's approach, this thesis provides a more rigorous test of the applicability of the driven-dissipative system model. The result is a more accurate, generalized model of thermospheric temperatures using solar wind inputs as a driver.

5

Since exospheric temperature is used as a parameter in existing thermospheric models to determine densities (Wise, et al., 2012), a more accurate specification of exospheric temperature can be used to improve density forecasts.

The remainder of this thesis is structured as follows. Section II provides background information on the thermospheric energy budget, thermospheric variability, current thermospheric models, and Burke's driven-dissipative system model. Section III details the methodology used to develop the model formulation of this thesis. Section IV presents the results of the updated model formulation and where appropriate compares the results with Burke's earlier work. Finally section V presents conclusions and recommendations for future research.

II. Background

The Thermosphere

The thermosphere is generally defined as the neutral part of the Earth's upper atmosphere from 95 to 1000 km above sea level. It is characterized by a temperature profile that increases with height in its lower levels to a maximum constant value which is maintained to the top of the atmosphere (Schunk and Nagy, 2009). The top of the thermosphere is defined as the altitude at which neutral densities become low enough that collisions become negligible, the atmosphere can no longer be treated as a fluid and individual atoms and molecules have a realistic probability of escaping the atmosphere all together (Schunk and Nagy, 2009). This level is referred to as the exobase and the temperature at this level, the exospheric temperature, is a major input for many current thermospheric models.

Thermospheric Energy Input

There are three main sources of energy input to the thermosphere: Extreme ultraviolet (EUV, $\lambda < 175$nm) irradiance from the sun, joule heating, and particle precipitation (Knipp, et al., 2004). Figure 1 shows the contribution of each energy input over the period of solar cycles 21-23 from 1975 through 2003. The lower gray curve in Figure 1 shows the power input to the thermosphere from particle precipitation, the blue curve represents the joule power input and the upper red curve depicts power input from EUV irradiance. EUV irradiance in general dominates the day side of the thermosphere and is closely associated with the 11-year solar cycle. Joule heating and particle

precipitation are most important in the auroral zones and are closely associated with

geomagnetic activity (Knipp, et al., 2004). Each of the three energy sources is discussed

in the subsequent sections.
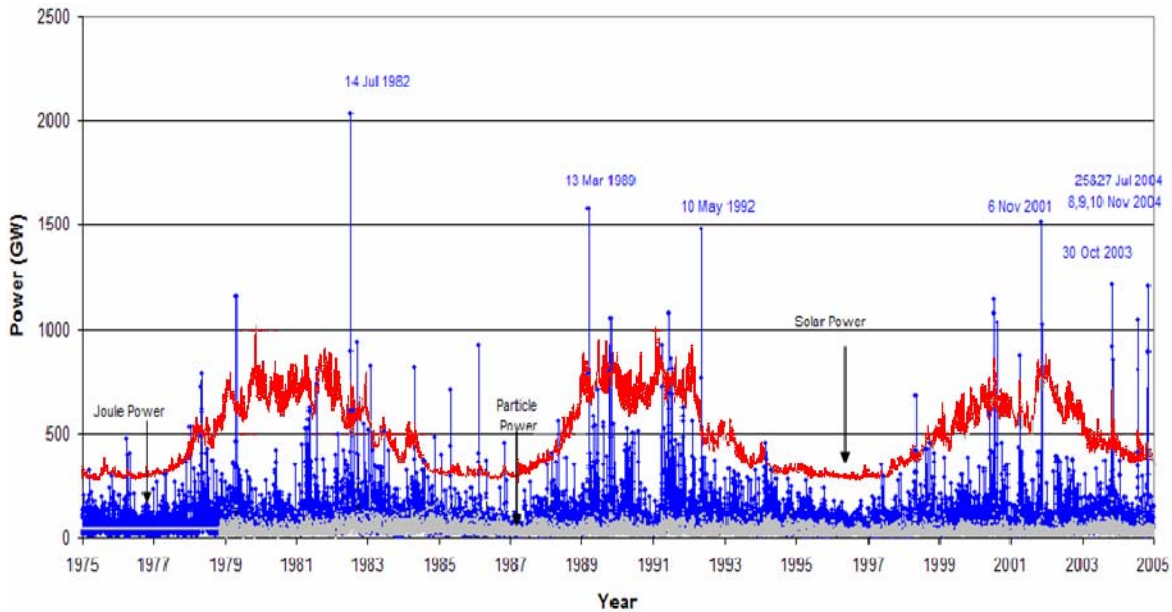
Figure 1: Power input to the thermosphere by particle precipitation (bottom gray line), joule heating (blue line), and EUV irradiance (red line) for each day from 1975 to 2003. Adapted from Knipp, et al., 2004.

Solar EUV Irradiance

Solar EUV irradiance, emitted from the sun's chromosphere and corona, is

usually the dominant contributor to thermospheric energy. From 1975-2003 solar

irradiance made up an average of 78% of the total energy input to the thermosphere

(Knipp, et al., 2004). The energy is deposited mainly in the layer from 150-200 km

(Knipp, et al., 2004) via absorption by neutrals, primarily O_2 and N_2 (Schunk and Nagy,

2009). Because a portion of the absorbed energy goes into dissociation and ionization, the heating efficiency is limited to around 50% (Knipp, et al., 2004). The solar irradiance contribution to thermospheric energy varies by 100% or more over the course of a solar cycle as seen in Figure 1. The day to day variation is much smaller during solar minimum than near solar maximum.

Joule Heating

Joule heating is the process in which an electric current passes through the thermosphere resulting in resistance and heating of the neutral gas (Qian and Solomon, 2011). On average, joule heating accounts for 16% of the total energy input to the thermosphere via deposition mainly from 110-140 km (Knipp, et al., 2004). The energy source for thermospheric joule heating is the solar wind which interacts with the magnetosphere to create electric fields that map into the thermosphere and drive currents. Lu et al., 1998 showed that on average about 60% of the solar wind energy that is transferred to the magnetosphere is deposited in the thermosphere. During storm times the amount of solar wind energy deposited in the thermosphere through the magnetosphere can reach 80% (Lu, et al., 1998). Since joule power input is caused by currents, it can be monitored with indices that respond to ionospheric or magnetospheric currents such as the AE index, which monitors the auroral electrojet, and the Dst index, which monitors the ring current (Knipp, et al., 2004).

While joule power input is generally much smaller than solar irradiance, it exhibits more variability. Since joule heating is over 90% efficient in transferring power to the thermosphere (compared to 50% efficiency for the solar and particle inputs) any

9

change in available power is readily transferred to the thermosphere (Knipp, et al., 2004; Thayer and Semeter, 2004). When looking at the 100 days with the highest total power inputs of from solar cycles 21 - 23, Knipp, et al., 2004 found that solar irradiance increased 50% above its average value while joule power increased by over 600% above its average. During large geomagnetic storms the joule power input becomes the dominant power source for the thermosphere and when combined with the particle precipitation power input, the power input due to geomagnetic activity accounts for 65% of the total (Knipp, et al., 2004). When examining thermospheric variability on short time scales joule power becomes the most important term.

Particle Precipitation

Another way that energy is transferred from the solar wind to the thermosphere is via precipitation of electrons. Solar wind electrons travel along open magnetic field lines or through the magnetotail into the auroral zone where they are absorbed (Prölss, 2004), primarily from 100-120 km (Knipp, et al., 2004). Since some of the electron energy goes into ionization, rotational, or vibrational states the heating efficiency for particle precipitation is limited to around 50%. On average, particle precipitation accounts for 6% of the total power input to the thermosphere (Knipp, et al., 2004). During geomagnetic activity, the magnetosphere interacts with the solar wind magnetic field resulting in more open field lines and more available paths for electrons to reach and transfer power to the thermosphere (Prölss, 2004). Strong geomagnetic storms result in an increase in power input due to particle precipitation of up to 200% compared with average values (Knipp, et al., 2004).

Thermospheric Energy Loss

On long time scales the thermospheric system is in a state of equilibrium where the energy input is equal to the energy loss as evidenced by observations that show thermospheric temperatures do not increase or decrease indefinitely. One of the major loss mechanisms for thermospheric energy is emission by nitric oxide (NO) at 5.3 μm (Sharma, et al., 1996). Radiation at 5.3 μm is not readily absorbed by any major atmospheric constituent so energy at this wavelength is able to escape into space.

To maintain equilibrium, there must be a mechanism during storm time by which the excess energy input to the thermosphere via joule heating and particle precipitation is dissipated as the thermosphere relaxes to its pre-storm state. Since the production rate of NO is highly dependent on temperature (Bailey, et al., 2002), the high thermospheric temperature during geomagnetic storms leads to increased NO densities resulting in increased cooling rates. Mlynczak et al., 2005 found that increased NO emissions during geomagnetic storming accounted for roughly 94% of the added thermospheric energy loss during the recovery period. The rest of the energy loss increase can be accounted for by increased CO_2 emissions at 15 μm (2%) and increased conduction between the thermosphere and mesosphere (4%) (Mlynczak, et al., 2005).

Thermospheric Variability

Solar EUV irradiance is the primary energy input to the thermosphere, while joule heating and particle precipitation are secondary the majority of the time. Both the primary and secondary drivers result in variability in thermospheric densities and temperatures on different time scales and each can be accounted for through the use of various

observations and proxies. Variations on specific temporal and spatial time scales will be discussed below.

Solar Cycle Variability

The sun exhibits a cycle between solar minimum and solar maximum with a period of roughly 11 years, characterized in part by changes in solar irradiance (Figure 1). During solar maximum there are many more active regions on the sun resulting in increased irradiance, increased flaring, and more frequent coronal mass ejections which in turn increase geomagnetic activity. This periodic irradiance variation, along with the increase in geomagnetic activity as a lesser factor, generates a similar variation in exospheric temperature, thermospheric energy and density at the earth. The thermospheric density at a given altitude during solar max can be up to ten times more than the density at that same altitude during solar min (Qian and Solomon, 2011).

Semiannual Variability

Thermospheric density varies on a semiannual basis with maximums at the equinoxes and minimums near the solstices. This variation was first identified by Paetzold and Zchorner, 1961 when they showed that the difference between minimum and maximum is more than 100%. Semi-annual variability is driven primarily by the variation in the distance from the sun to the earth which causes differences in solar irradiation. Between this variation and the solar cycle variation described above, it is clear that even with geomagnetic activity removed from consideration the density of the thermosphere fluctuates. Any attempt to model densities accurately must account for

variations in both the solar and geomagnetic contributions if it is to accurately

characterize the thermospheric environment.

Solar-Rotation Variability

The sun rotates differentially with an average period of 27 days and during this

rotational period active regions of the sun appear and disappear from the Earth's view.

Since active regions can persist for several months they may come into and disappear

from the Earth's view multiple times during their lifetime. Active regions are associated

with increased solar irradiance and geomagnetic activity and therefore solar rotation

results in periodic changes in irradiance and geomagnetic activity. This periodic

variability in irradiance and geomagnetic activity results in a variability of up to 100% in

thermospheric density during solar maximum (Qian and Solomon, 2011).

Multi-Day Variability

Variations in the solar wind caused by high-speed streams (HSS) result in low

levels of geomagnetic activity and can therefore impact the thermosphere via increased

joule heating and particle precipitation. Observations during the declining phase of solar

cycle 23 showed periodic variations in the source of HSS, coronal holes (Temmer, et al.,

2007). Similarly Lei et al., 2008, found a 9-day periodic variation in neutral density

observations from the CHAMP satellite in 2005. The magnitude of these variations is

smaller than those due to solar rotation, roughly 30 – 50% in density.

Diurnal Variability

As expected, the large disparity in solar irradiance between the day and night

sides of the thermosphere results in a large density variation between the two. Mueller et

al., 2009, found that during geomagnetic quiet periods the density on the day side was roughly twice that on the night side. By taking orbit averages of density measurements from polar orbiting satellites such as GRACE the diurnal variation can be effectively averaged out of observed data.

Short Term Variability

Density variations on time scales of minutes to hours can be caused by rapidly changing energy inputs to the system from solar flares or geomagnetic storms associated with coronal mass ejections (CMEs) or high-speed streams. Solar flares cause rapid increases in EUV and X-ray irradiance leading to heating and expansion of the upper atmosphere (Pawlowski and Ridley, 2008). Thermospheric density increases depend on the flare's intensity, location, and the details of the flare's spectral enhancement. Density increases of up to 40% have been observed in response to long duration (> 40 min) X-class flares (Qian and Solomon, 2011).

Geomagnetic storms also result in increased energy inputs to the thermosphere however the process by which the energy is deposited is different. During geomagnetic storms energy is transferred from the solar wind to the thermosphere via joule heating and particle precipitation at high (auroral) latitudes. Joule heating in the thermosphere is the dominant form of energy transfer over particle precipitation during geomagnetic storms (Wilson, et al., 2006). The energy deposited at high latitudes is propagated throughout the thermosphere via circulation and atmospheric gravity waves over a time period of several hours (Bruimsma, et al., 2006). The focus of this research is to better characterize the impact of geomagnetic storms on the thermosphere.

Geomagnetic Storming

       A geomagnetic storm has been defined by Prölss, 2004 as "an event of strongly

enhanced dissipation of solar wind energy in the near-Earth space environment." During

geomagnetic storming both the joule heating and particle precipitation energy inputs to

the thermosphere are enhanced. The dominant factors in determining the amount of

energy transfer, and therefore the strength of a geomagnetic storming event, is the

component of the interplanetary magnetic field in the z direction, B_z and the length of

time B_z is in the negative z direction. The z direction is defined by Geocentric Solar

Magnetospheric (GSM) coordinates shown in Figure 2.
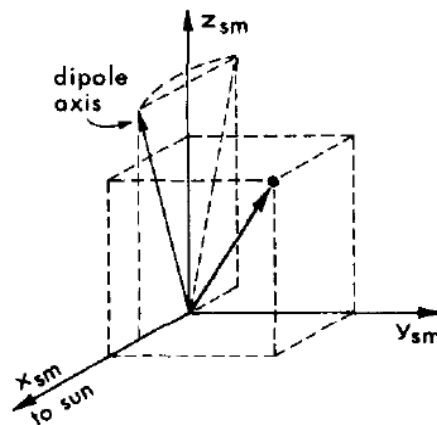
Figure 2: Illustration of the geocentric solar magnetospheric (GSM) coordinate system. The origin is the center of the earth, the x axis points toward the sun, the y axis is perpendicular to both x and the geomagnetic dipole axis, and the z axis completes the set with positive pointing north. (Knecht and Shuman, 1985)

       Solar wind energy is transferred to the thermosphere through the magnetosphere

via a dynamo of conductive solar wind plasma moving across the Earth's magnetic field

lines. This dynamo is made possible by an "open magnetosphere" magnetic field

configuration created by the interaction between a southward interplanetary magnetic

15

field and the Earth's dipole magnetic field shown in Figure 3. The southward B_z interacts

with Earth's northward-pointing magnetic field, weakening the field on the day side of

Earth and resulting in an increased number of open magnetic field lines (Prölss, 2004).

An open magnetic field line has one footpoint on Earth in the auroral region and the other

in space (Prölss, 2004). These open magnetic field lines provide pathways that allow

energetic particles to reach the thermosphere, increasing power input from particle

precipitation, and allow an electric dynamo to transfer energy from the solar wind to the

thermosphere via joule heating.
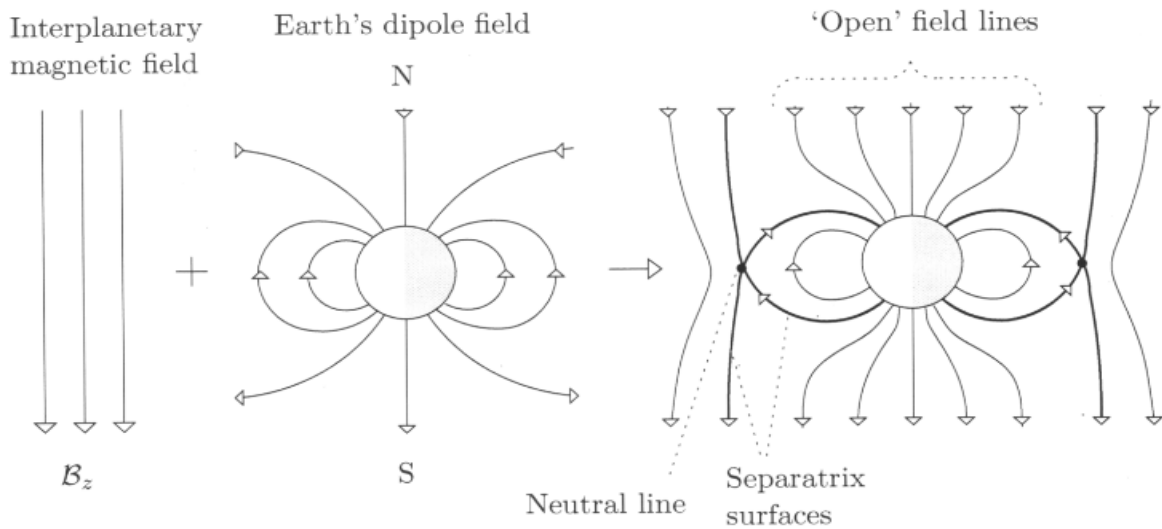
Figure 3: The interaction between a southward Interplanetary Magnetic Field (B_z south) and the Earth's dipole magnetic field is shown. The result is open magnetic field lines, with one footpoint near the polar cap and the other in interplanetary space. This configuration is referred to as the open magnetosphere. Figure from Prölss, 2004.

Prölss, 2004 describes the energy transfer process as follows. With an open

magnetosphere the Earth's magnetic field lines originating near the polar cap are not

16

closed but open extending into the interplanetary medium, as shown in Figure 4. As the

solar wind flows across this magnetic field the charged particles experience a Lorentz
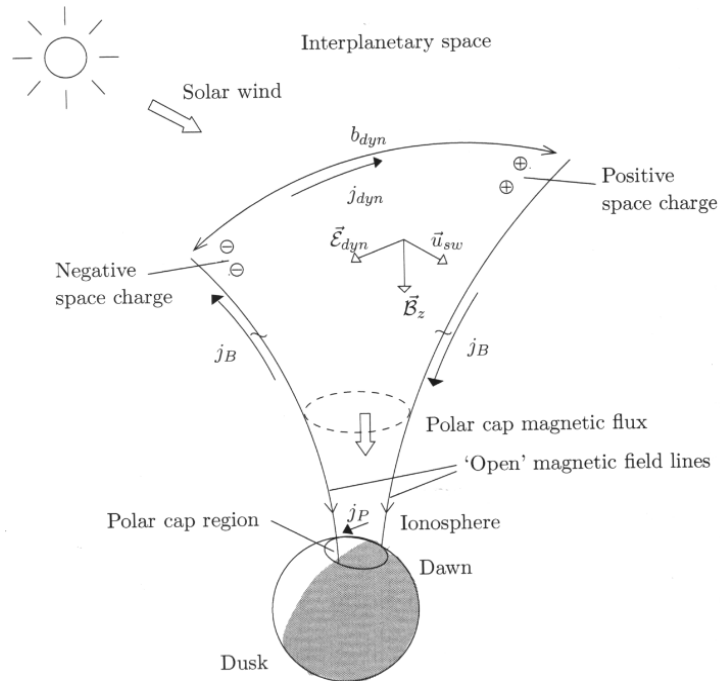
Figure 4: The interaction between the solar wind and the open magnetosphere configuration is shown. Figure from Prölss, 2004.

force, causing the positively charged particles to be deflected towards the dawn side and

the negative particles to be deflected towards the dusk side. The resultant charge

separation creates a polarization electric field, $\vec{\mathcal{E}}_P$, which builds up until the force on

charged particles due to the polarization field matches that due to the Lorentz force, as

shown in Equation (2)

$$n_s q_s \vec{\mathcal{E}}_P + n_s q_s \vec{u}_{sw} \times \vec{B}_z = 0 \qquad (2)$$

where n_s is the number density of a given species, q_s is the charge of a given species, and $\vec{u}_{sw}$ is the solar wind velocity. Solving, we see that the polarization electric field is equal to the negative solar wind velocity crossed with the z component of the magnetic field.

$$\vec{\mathcal{E}}_P = -\vec{u}_{sw} \times \vec{B}_z = \vec{\mathcal{E}}_{dyn} \qquad (3)$$

This quantity is also known as the electric dynamo field, $\vec{\mathcal{E}}_{dyn}$, and is shown in Figure 4. The dawn to dusk electric dynamo field maps along the magnetic field lines to the polar cap region where it drives a current, denoted in Figure 4 as j_P, that deposits energy into the thermosphere/ionosphere system via joule heating.

The energy input to the thermosphere by joule heating is extracted from the solar wind and manifested through a reduction in solar wind velocity. The electric dynamo field drives a current in the magnetosphere, denoted in Figure 4 by j_{dyn}, which interacts with the interplanetary magnetic field to produce a force in the direction opposing the solar wind flow and decreasing the flow velocity.

$$\vec{F}_B = \vec{j}_{dyn} \times \vec{B}_z \qquad (4)$$

The current loop between the polar cap current, j_p, and the dynamo current, j_{dyn}, is closed by the region one Birkeland currents, j_B, shown in Figure 4. Region one currents are defined as currents originating on the poleward boundary of the auroral oval (Prölss, 2004).

An open magnetosphere configuration is necessary to create the enhanced joule heating and particle precipitation power input to the thermosphere observed during geomagnetic storming. The two main solar phenomena which lead to strong southward B_z, creating an open magnetosphere and geomagnetic storming, are coronal mass ejections (CMEs) and co-rotating interaction regions (CIRs).

Coronal Mass Ejections

A CME is a large emission of mass from the sun, on the order of $10^{12} - 10^{13}$ kg, at speeds of $50 - 1800$ km/s with an average kinetic energy ranging from 10^{23} to 10^{25} J (Prölss, 2004). CMEs are accelerated outward from the sun by magnetic forces in the sun's corona. Depending on the orientation of the magnetic field within the ejected material, a CME's encounter with earth can produce a southward B_z along with enhanced solar wind velocity and density resulting in geomagnetic storming (Prölss, 2004).

Co-Rotating Interaction Regions

CIRs have their source on the sun at the boundaries between coronal holes and coronal streamers. Coronal holes are a source of high-speed solar wind streams while coronal streamers are a source of low-speed solar wind flow (Prölss, 2004). As the solar wind propagates out from the sun towards Earth the difference in velocity between the two regions results in a compression of the solar wind plasma in the area where the high-speed stream interacts with the low-speed flow. This area of compression is defined as a CIR. When solar plasma leaves the sun as the solar wind it carries with it a "frozen-in" magnetic field with the same orientation as its source region on the sun. The magnetic field is compressed along with the plasma inside the CIR. If the frozen-in magnetic field

19

was already oriented southwards, the amplification inside the CIR is sufficient to produce geomagnetic storming when the CIR encounters Earth's magnetic field (Prölss, 2004).

Storm Type Characteristics

A geomagnetic storm produced by a CME is distinct from one produced by a CIR in several ways (Borovsky and Denton, 2006). The rate of CME-driven storm occurrence peaks during solar maximum and is smallest during solar minimum (Webb, 1991) while the frequency of CIR-driven storms is the highest during the declining phase of the solar cycle (Mursula and Zeiger, 1996). The occurrence pattern for CME-driven storms is irregular with no characteristic spacing between events while CIR-driven storms are characterized by a 27-day periodicity due to the rotation of their source regions, coronal holes, on the sun (Borovsky and Denton, 2006). CME-driven storms are more effective than CIR-driven storms in producing highly negative Dst values (Dst < -100 nT) and are usually characterized by a shock in the solar wind flow, evidenced by a sharp increase in solar wind velocity and density (Borovsky and Denton, 2006). CIR-driven storms normally produce less extreme Dst values and exhibit a more gradual commencement. These differences were used to classify the storms used in this thesis as either CME or CIR storms.

Figure 5 shows typical solar wind profiles for both CME (top) and CIR (bottom) storms. The CME storm has an extreme Dst minima of -181 nT while the CIR storm does not drop below -50 nT. The start of the CME storm is evident in the rapid rise in solar wind pressure and velocity around JD 250.7. In contrast, the CIR storm exhibits a gradual increase in solar wind pressure and veolcity between JD 191.5 and 192.

20
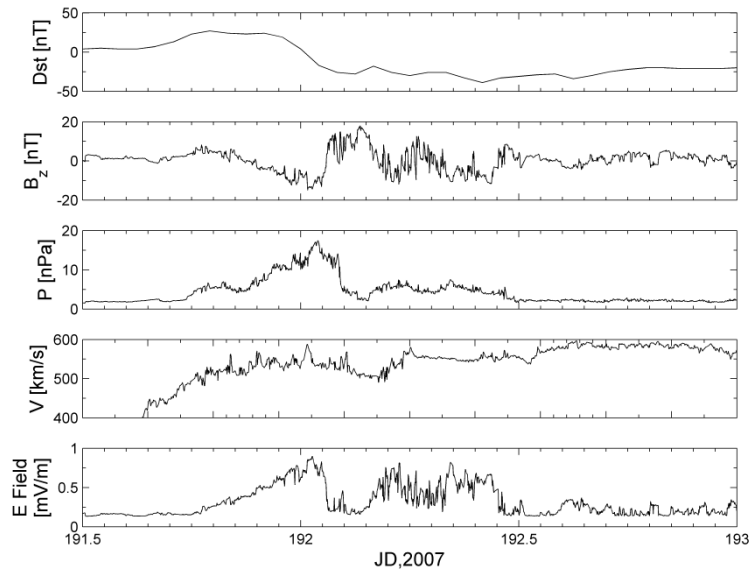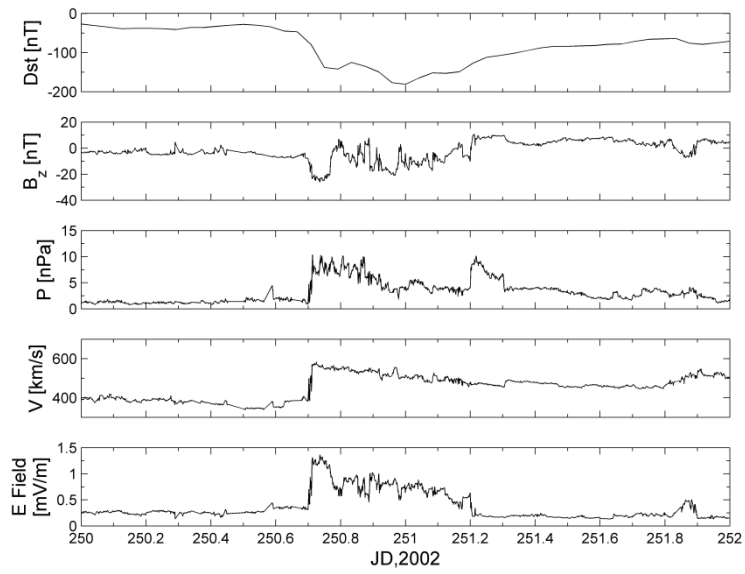
Figure 5: Typical solar wind signatures resulting from a coronal mass ejection (CME) driven geomagnetic storm (top) and a co-rotating interaction region (CIR) driven geomagnetic storm (bottom). From top to bottom the plots show Dst in nano-Tesla, the z-component of the interplanetary magnetic field in nano-Tesla (GSM coordinates), solar wind pressure (P) in nano-pascals, solar wind velocity (V) in km/s, and the resulting magnetospheric electric field value, in milivolts/meter as functions of julian date (JD) counted as days since 1 January of the given year.

21

Thermospheric Driver Proxies

Since both the primary (solar EUV irradiance) and secondary (geomagnetic activity) sources of thermospheric energy have historically been difficult to measure directly various proxies and indices are used to quantify their variation for use in models. In some thermospheric models geomagnetic activity has been accounted for through the use of the a_p index. The a_p index is a linear index ranging from zero to 400 that is derived using the deviation from the standard magnetic field values measured at 13 locations worldwide at geomagnetic latitudes ranging from 42 to 62 degrees (Helmholtz Centre Potsdam GFZ, 2012). Values are computed every three hours for a_p and daily averages are computed and reported as A_p. The fact that the a_p index is measured at mid latitudes results in a failure to detect the full impact of large geomagnetic storms (Bowman, et al., 2008) due to distortion from the equatorward movement of the auroral electrojet.

Another measure of geomagnetic activity is the disturbance storm time index (Dst). Dst is measured hourly at four different near-equatorial observatories and it measures the variations in the Earth's magnetic field resulting from changes in the magnetospheric ring current. Since the ring current responds directly to energy inputs from the solar wind, it is enhanced during periods of geomagnetic storming. Dst is measured in nano-Tesla (nT) and during quiet conditions it is usually near zero. Storming conditions are indicated by negative values and the more negative the value the stronger the storm. Because of the equatorial location of its observation stations, Dst is not influenced by the auroral zone and is able to detect more fully the energy enhancements to the ring current caused by strong geomagnetic storms. The Dst index has been adopted

22

for use in some recent thermospheric models such as Jacchia-Bowman 2008 (Bowman, et al., 2008).

The $F_{10.7}$ index has long been the standard proxy for EUV flux. Since the atmosphere absorbs virtually all of the EUV radiation before reaches the surface it is not possible to measure EUV flux at a surface based observatory. Instead, EUV flux values can be inferred using measurements of the solar radio flux at a wavelength of 10.7 cm at the Earth's surface. This 10.7 cm flux has been shown to correlate well with actual EUV flux. $F_{10.7}$ values are observed at the Pentictin Radio Observatory in British Columbia, Canada daily at 2000Z (local noon). Daily $F_{10.7}$ values, along with a longer term 81 or 162-day average, have been used in many models to account for the variation in EUV flux (Tascione, 1994). Unfortunately, the observed nature of the $F_{10.7}$ index and its once-daily time resolution have limited models making use of it as a input.

Partly in an effort to overcome these limitations, the first full-spectrum solar irradiance model, SOLAR2000, was developed by Tobiska et al. in 2000. This model includes a new EUV proxy index, $E_{10.7}$, which is in the same units of the standard $F_{10.7}$ index so as to enable its use in existing modeling applications. The $E_{10.7}$ has several advantages over the $F_{10.7}$ including the availability of high temporal resolution data rather than the once-daily $F_{10.7}$ and the ability to forecast $E_{10.7}$ values into the future which does not exist with the observed $F_{10.7}$ index. Some recent models, such as HASDM, have adopted $E_{10.7}$ to replace $F_{10.7}$ for these and other reasons (Storz, et al., 2005).

The $E_{10.7}$ models total integrated EUV emissions from both the chromosphere and the corona while the $F_{10.7}$ proxy only captures coronal emissions. By providing a more

complete picture of total EUV irradiance the $E_{10.7}$ is a more representative proxy for the impact of EUV irradiance on the thermosphere. However, it leads to differences when compared with the longtime-standard $F_{10.7}$. Tobiska et al., 2000 found that $F_{10.7}$ exhibited more variability than $E_{10.7}$, as much as +/- 20% during comparisons ran for July, 1982. The increased variability of the $F_{10.7}$ was due to the fact that it does not measure chromospheric emissions, which tend to smooth out the $E_{10.7}$ values.

Thermospheric Models

These indices and proxies, along with historic and real-time observations, have been used to create many different models of the thermosphere. The following sections briefly describe three thermospheric models relevant to this thesis.

Jacchia Models

Jacchia developed a model of the thermosphere in 1970 (J70) (Jacchia, 1970) and an updated version in 1977 (J77) (Jacchia, 1977) that are still used as a baseline today. The Jacchia models are static models which were developed using thermospheric densities calculated from satellite drag and mass spectrometer measurements. They are based on the assumption that the thermosphere is in thermal diffusion equilibrium, meaning that the heat inputs to the thermosphere equal heat losses. The J77 model assumes the mesopause, the bottom of the thermosphere, is at an altitude of 90 km with a temperature of 188K and a mass density of 3.43 $\frac{g}{cm^3}$. Model temperatures rise as a function of altitude from the minimum value at 90km, pass through an inflection point at 125km, and increase asymptotically to the given exospheric temperature, T_∞ . T_∞

24

uniquely defines the temperature profile. Once the temperature profile is determined,

densities are calculated by integrating the thermal diffusion equation, Equation (5),

$$\frac{dn_i}{n_i} = -\frac{m_i g}{R^* T} dz - \frac{dT}{T}(1 + a_i) \tag{5}$$

where the index i denotes the ith species, n is the number density, m is the mass, g is

gravity, a is the thermal diffusion coefficient, T is the temperature and R^* is the universal

gas constant. The J77 model includes six species: N_2, O_2, O, Ar, He, and H. The total

mass density at a given altitude can be calculated by simply summing the product $n_i m_i$

over all species (Wise, et al., 2012). Through this process, tables are produced that give

density profiles for a given exospheric temperature input.

Variations due to solar changes and geomagnetic activity are accounted for in the

Jacchia models either solely through perturbations to the temperature profile (J70) or

through perturbations to both the temperature and resulting density profiles (J77). The

J77 model accounts for variations in EUV energy input by using the $F_{10.7}$ proxy and an

$F_{10.7}$ index value averaged over six solar rotations (162-days), $F_{10.7a}$, to compute a

geomagnetic-quiet (defined as $A_p = 0$) arithmetic-mean exospheric temperature, $T_{1/2UV}$.

The arithmetic mean temperature, $T_{1/2}$, is defined as the average of the nighttime

minimum exospheric temperature, T_0, and the daytime maximum exospheric temperature,

T_M, which occur in opposite hemispheres at 0524 and 1648 Local Standard Time (LST),

respectively (Jacchia, 1977). $T_{1/2}$ is related to T_∞ at any given location via a conversion

factor dependent on latitude, local time and solar declination angle. Using the J77 model,

unique temperature and density profiles can be computed for any location given $T_{1/2}$. The

J70 model uses a similar process but instead of $T_{1/2}$ its global temperature parameter is T_0. The tables in the J70 and J77 models form the basis of many current thermospheric models. For this thesis, J77 serves as the link between observed neutral density measurements from GRACE data and an "observed" exospheric temperature used for comparison with the exospheric temperature calculated using Burke's driven-dissipative model.

High Accuracy Satellite Drag Model (HASDM)

The Jacchia models have been improved through the years but continue to be limited by their use of proxies to measure actual thermospheric conditions as well as their reliance on a static and limited set of observed data upon which their empirical fits are based. These limitations, along with others, prevent satellite position error from decreasing below 15% (Marcos, et al., 2007). To address this problem the Air Force Space Command Battlelab created HASDM, the Air Force's current operational thermospheric density model, in 2004 (Storz, et al., 2005).

HASDM makes use of the a_p index to characterize geomagnetic activity. To characterize EUV flux HASDM uses the $E_{10.7}$ index from the SOLAR2000 model described by Tobiska et al., 2000. The critical advance of the HASDM approach is the use of near real-time observed density data. The model uses data from the observed drag on a set of about 80 calibration satellites to create spatially varying density corrections every three hours. These corrections are used in conjunction with a modified J70 model to produce a global density forecast up to 72 hours into the future. This approach of relying on observed data in real time to dynamically update and correct density

26

predictions helped reduce positional errors down to 5% for the calibration satellites and down to 8% for all tracked objects during quiet conditions (Storz, et al., 2005). Unfortunately, HASDM does not perform as well during geomagnetic storming conditions. During storm periods neutral density errors increase by roughly 30%, from 13% during quiet conditions ($A_p = 0$) to 17% during storming conditions ($A_p > 100$) (Marcos, et al., 2010). HASDM leaves room for improved characterization of storming conditions.

Jacchia-Bowman 2008 (JB2008) Model

JB2008 is an empirical model which uses density inputs from Air Force daily density values (computed using tracking data from around 100 calibration satellites) and HASDM as well as CHAMP and GRACE accelerometer data (Bowman, et al., 2008). JB2008 uses the $F_{10.7}$ index and the 81-day average $F_{10.7}$ index along with 26 - 34 nm integrated EUV flux data from the Solar Heliospheric Observatory (SOHO) satellite, chromospheric and photospheric active region activity data measured by the Solar Backscatter Ultraviolet (SBUV) spectrometer, and X-ray emission data from GOES X-ray spectrometers to compute T_0. This approach allows the JB2008 model to capture not only solar cycle and semi-annual solar irradiance variations but also measure shorter term variations on the scale of the 27-day solar rotation period.

Another advance of the JB2008 model is its use of Dst to measure geomagnetic activity rather than the a_p index used by previous models. It is a better input to thermospheric models than a_p because a_p responds mainly to ionospheric currents rather than magnetospheric ones. Since the energy deposited into the thermosphere during

27

geomagnetic storms comes from the solar wind through the magnetosphere it is reasonable to use an input that primarily measures magnetospheric conditions like Dst. In addition, a_p is determined by observatories at latitudes from 42 to 62 degrees which can incorrectly characterize energy inputs during severe storms due to the equatorward movement of the auroral electrojet. Since ground-based observatories are immobile, significant electrojet movement during storm time leads to underestimates of storm impacts (Huang and Burke, 2004). Dst responds to the ring current and is derived from measurements at four equatorial observatories not impacted by auroral electrojets. Using Dst as an input, a geomagnetic activity contribution to T_0 is calculated and then used to generate a density profile.

Modeling the Thermosphere as a Driven-Dissipative Thermodynamic System

While thermospheric models have made advances in accuracy recently, they are still physically limited by the lack of a direct link between the solar wind and the thermosphere which is the dominant source of energy during geomagnetic storming. The driven-dissipative approach attempts to solve this problem by linking the thermosphere to the solar wind using the electric field of the magnetosphere as the primary driver during geomagnetic storm conditions.

Burke et al., 2009 used neutral density observations from the GRACE satellite along with the J77 model (Jacchia, 1977) to calculate thermospheric energies, E_{th}, as a function of time during 2004. Magnetospheric electric field magnitudes, ε_{VS}, were computed using observed solar wind data and plotted as a function of time along with the E_{th} data. Figure 6 (Burke, et al., 2009) shows that E_{th} decays to pre-disturbance levels

when ε_{VS} drops to pre-disturbance levels and the rate of decay, at least for the two cases

shown, was the same. This behavior matches that of a driven-dissipative system. The e-

fold relaxation time of E_{th}, τ_E, was calculated to be 6.5 hours. Burton et al., 1975

proposed that Dst behaved in a similar way and could be described by a simple

differential equation. Burke et al., 2009 applied this technique to modeling E_{th} using ε_{VS}

as the driver. Since E_{th} is related to the exospheric temperature (T_∞) linearly, T_∞ can also

be modeled in this way. The following sections will detail the Burke et al., 2009 approach

and highlight some of the simplifying assumptions that were made during its

development.
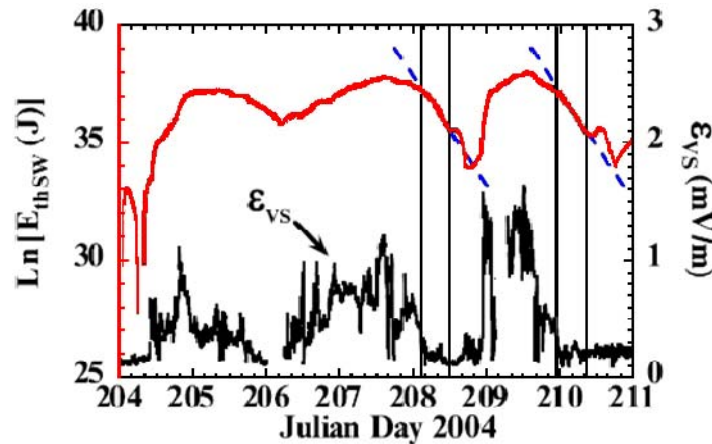
Figure 6: Plots of magnetospheric electric field ε_{VS} (black) and the natural logarithm of $E_{th\ SW}$ (red) for the disturbance on JD 204-211, 2004. Vertical lines mark times of electric field decrease. The slanted blue lines have the same slopes indicating that $E_{th\ SW}$ decays exponentially when ε_{VS} turns off. The estimated e-fold relaxation time is 6.5 hrs. (Adapted from Burke et al., 2009)

Observed Data

Burke et al., 2009 used measured thermospheric orbit-averaged density and orbit-

averaged altitude from the GRACE satellite as ground truth data. These data were used to

calculate exospheric temperature using a quadratic fit to the Jacchia 1977 model (Burke, 2008), namely

$$T_\infty = \sum_{i=0}^{2} a_i\left(\overline{h}\right)\rho^i\left(\overline{h}\right) \qquad (6)$$

where T_∞ is the exospheric temperature and $\rho^i\left(\overline{h}\right)$ is the orbit averaged neutral density in g/cm^3 raised to the ith power. The term $a_i\left(\overline{h}\right)$ is a coefficient described by the matrix equation

$$\begin{pmatrix} a_0\left(\overline{h}\right) \\ a_1\left(\overline{h}\right) \\ a_2\left(\overline{h}\right) \end{pmatrix} = \begin{pmatrix} -28.10 & 2.69 & -2.03\times10^{-3} & 0 & 0 & 0 \\ -4.733\times10^{17} & 4.312\times10^{15} & -1.372\times10^{13} & 1.60\times10^{10} & 0 & 0 \\ 3.2695\times10^{32} & -4.620\times10^{30} & 2.618\times10^{28} & -7.456\times10^{25} & 1.071\times10^{23} & -6.237\times10^{19} \end{pmatrix} \times \begin{pmatrix} 1 \\ \overline{h} \\ \left(\overline{h}\right)^2 \\ \left(\overline{h}\right)^3 \\ \left(\overline{h}\right)^4 \\ \left(\overline{h}\right)^5 \end{pmatrix} \qquad (7)$$

where $\overline{h}$ is the orbit averaged altitude in km. Burke (Burke, et al., 2009) took an orbit average of density and height before calculating the orbit averaged exospheric temperature.

Once the exospheric temperature is calculated, the total energy of the thermosphere can be calculated using the empirical formula

$$E_{th}\left(h \geq 100km\right) = 5.365\times10^{17} + \left(8.727\times10^{13}\right)\overline{T}_\infty \qquad (8)$$

Where E_{th} is the energy of the thermosphere in Joules and $\bar{T}_\infty$ is the orbit-averaged exospheric temperature. These values of E_{th} and $\bar{T}_\infty$ were used as the "observed" data for comparison with the results of the driven-dissipative model (Burke, et al., 2009).

Differential Equations

As shown in Figure 6, E_{th} responds to changes in magnetospheric electric field in a way reminiscent of a driven-dissipative thermodynamic system. Burton et al., 1975, suggested that Dst evolves in a similar way and developed a differential equation for the pressure corrected Dst (Dst*)

$$\frac{dDst^*}{dt} = \alpha_D \varepsilon_I - \frac{Dst^*}{\tau_{RC}} \tag{9}$$

where α_D is the coupling coefficient, ε_I is the interplanetary magnetic field magnitude and τ_{RC} is the relaxation time constant of the ring current. Dst* is defined as $Dst^* = Dst - b\sqrt{P_{SW}} + c$ where b and c are empirical constants and P_{SW} is the dynamic pressure of the solar wind (Burton, et al., 1975). The term "driven-dissipative system" is illustrated by the form of Equation (9). The term $\alpha_D \varepsilon_I$ models the driver of energy input to the system and the term $\frac{D_{st}^*}{\tau_{RC}}$ models the dissipation of energy from the system.

Burke et al., 2009 used this approach to create a differential equation for E_{th} using magnetospheric electric field as the driver. Using this equation along with the linear relationship between E_{th} and $\bar{T}_\infty$ from Equation (8) yields a similar equation for $\bar{T}_\infty$. To simplify the model, E_{th} and T_∞ were broken into two independent components, one due to the EUV radiation and one due to the solar wind given by

$$E_{th} = E_{th\,UV} + E_{th\,SW} \tag{10}$$

$$\bar{T}_\infty = \bar{T}_{\infty\,UV} + \bar{T}_{\infty\,SW} \tag{11}$$

where $E_{th\,UV} = 6.1 \times 10^{17}\,J$ and $\bar{T}_{\infty\,UV} = 850\,K$, both considered constant. Then $E_{th\,SW}$

and $\bar{T}_{\infty\,SW}$ were both modeled using the differential equations

$$\frac{dE_{th\,SW}}{dt} = \alpha_E \varepsilon_{VS} - \frac{E_{th\,SW}}{\tau} \tag{12}$$

$$\frac{d\bar{T}_{\infty\,SW}}{dt} = \alpha_T \varepsilon_{VS} - \frac{\bar{T}_{\infty\,SW}}{\tau} \tag{13}$$

where α_E and α_T are the coupling constants and for thermospheric energy and exospheric

temperature respectively, τ is the relaxation time constant, the same for both parameters,

and ε_{VS} is the magnetospheric electric field calculated from solar wind data.

Equations (12) and (13) can be solved numerically for any time in the future using

the simple Euler method.

$$E_{th\,SW}(t_{n+1}) = E_{th\,SW}(t_n) + \Delta t \left(\alpha_E \varepsilon_{VS}(t_n) - \frac{E_{th\,SW}(t_n)}{\tau} \right) \tag{14}$$

$$\bar{T}_{\infty\,SW}(t_{n+1}) = \bar{T}_{\infty\,SW}(t_n) + \Delta t \left(\alpha_T \varepsilon_{VS}(t_n) - \frac{\bar{T}_{\infty\,SW}(t_n)}{\tau} \right) \tag{15}$$

Burke et al., 2009 used a time step (Δt) of 1 hour in their analysis.

Relaxation Constant

The relaxation constant (τ) is defined as the e-fold relaxation time of E_{th} and determined by the linear fit to a plot of the natural logarithm of $E_{th\,SW}$ during periods of low ε_{VS} after storming periods seen in Figure 6. Using two relaxation periods in 2004, the constant's value was determined to be $\tau \approx 6.5\ hrs$. This value is the same when applied to model either E_{th} or T_∞.

Coupling Constant

Burke, et al., 2009 used comparisons with GRACE data from JD 150-230, 2004 to determine the value of the coupling constant for thermospheric energy, α_E.

$$\alpha_E = 5.5 \times 10^{15}\ \frac{J \bullet m}{hr \bullet mV} \tag{16}$$

Using this value good agreement was shown between modeled thermospheric energy using Equation (14) and GRACE-derived thermospheric energy using Equation (8) during two storming periods in 2004, as shown in Figure 7.

Using the relationship between E_{th} and $\bar{T}_\infty$ shown in Equation (8), the coupling coefficient for exospheric temperature was found to be:

$$\alpha_T = \frac{\alpha_E}{8.727 \times 10^{13}} \approx 63 \frac{K \bullet m}{hr \bullet mV} \tag{17}$$

Using this value, relatively good agreement was shown between modeled, Equation (15), and GRACE-derived, Equation (6), exospheric temperatures during two storming periods in 2004, as shown in Figure 8.
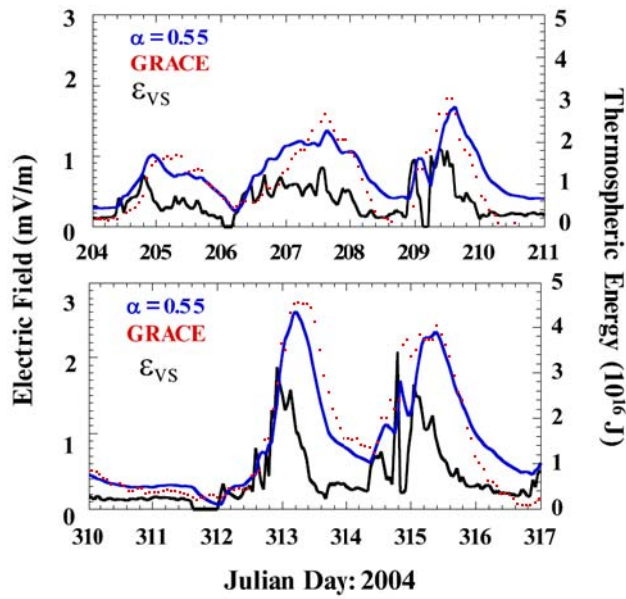
Figure 7: Comparison of ε_{VS} (black), modeled $E_{th\,SW}$ (blue), and $E_{th\,SW}$ values inferred from GRACE measurements (red dots) plotted as functions of Universal Time during the magnetically disturbed periods of July (top) and November (bottom) 2004. $E_{th\,SW}$ is plotted in units of 10^{16} J (Burke, et al., 2009).
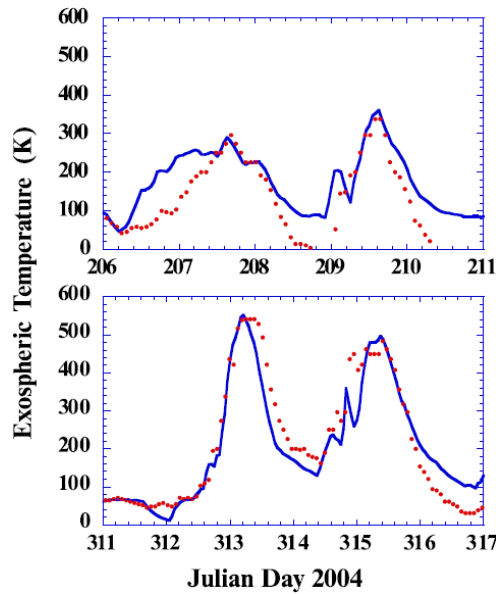
Figure 8: Modeled $\overline{T}_{\infty\,SW}$ (blue) and values inferred from GRACE measurements of orbit averaged neutral density (red dots), plotted as functions of Universal Time during July (top) and November (bottom) 2004. $\overline{T}_{\infty\,SW}$ was approximated by subtracting 850 K from GRACE-based estimates of $\overline{T}_{\infty}$ (Burke, et al., 2009).

34

To further test the validity of the coupling constant α_E, Burke et al., 2009 compared the term $\alpha_E \varepsilon_{VS}$, which represents the rate at which energy is input into the thermosphere from the solar wind, to predictions from the independent W5 model (Wiemer, 2005). The W5 model uses IMF and solar wind measurements to predict the Poynting flux into the ionosphere. By integrating this flux over the polar caps, the total rate of power input to the ionosphere can be determined and compared with the predictions from the term $\alpha_E \varepsilon_{VS}$ in the driven-dissipative model (Burke, et al., 2009). Figure 9 shows that during two storm periods in 2004 these two independent models produce similar results, validating the value for α_E.
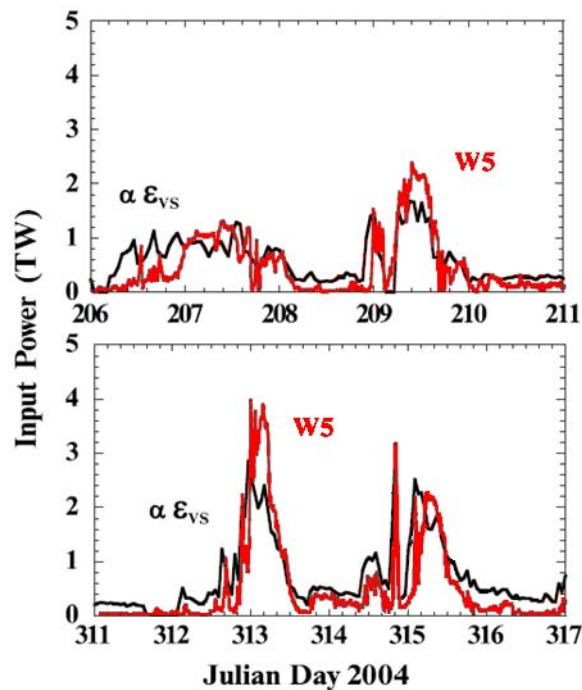
Figure 9: Comparison of storm time power into the global thermosphere predicted by the W5 model (red) and $\alpha_E \varepsilon_{VS}$ (black) plotted as functions of UT during July (top) and November (bottom), 2004 (Burke et al., 2009).

Overview

The success of the driven-dissipative model in predicting $T_{\infty SW}$ and E_{thSW} for the storm periods in 2004 is promising but to establish general applicability, a larger sample of storms needs to be studied. This section outlines the methodology used to test the driven-dissipative model in this thesis. First, a general schematic of the model is discussed. Then, the procedures utilized to determine the observed thermospheric temperatures and magnetospheric electric field values used in the model are outlined. Second, the model's governing equation is developed and solved. Next, the procedure used to determine optimal coupling and relaxation constant values for each storm is presented. Finally, a method to convert model temperature values to model density values is discussed.

Model Schematic

A general schematic of the model is shown in Figure 10. The model uses observed data from the GRACE satellite to derive orbit-average $T_{1/2}$ values which are used as the data the model attempts to replicate. Observed solar wind data from the ACE satellite is used to calculate magnetospheric electric field magnitudes which serve as the driver of energy input to the thermosphere in the model. The governing equation is then solved using one of three UV methods and an error minimization routine which selects values for the coupling and relaxation constants for each storm. This process results in model $T_{1/2}$ data for each method and each storm. Model $T_{1/2}$ data is then converted to

model density values via the J77 model. Each step is explained in subsequent sections of this chapter.
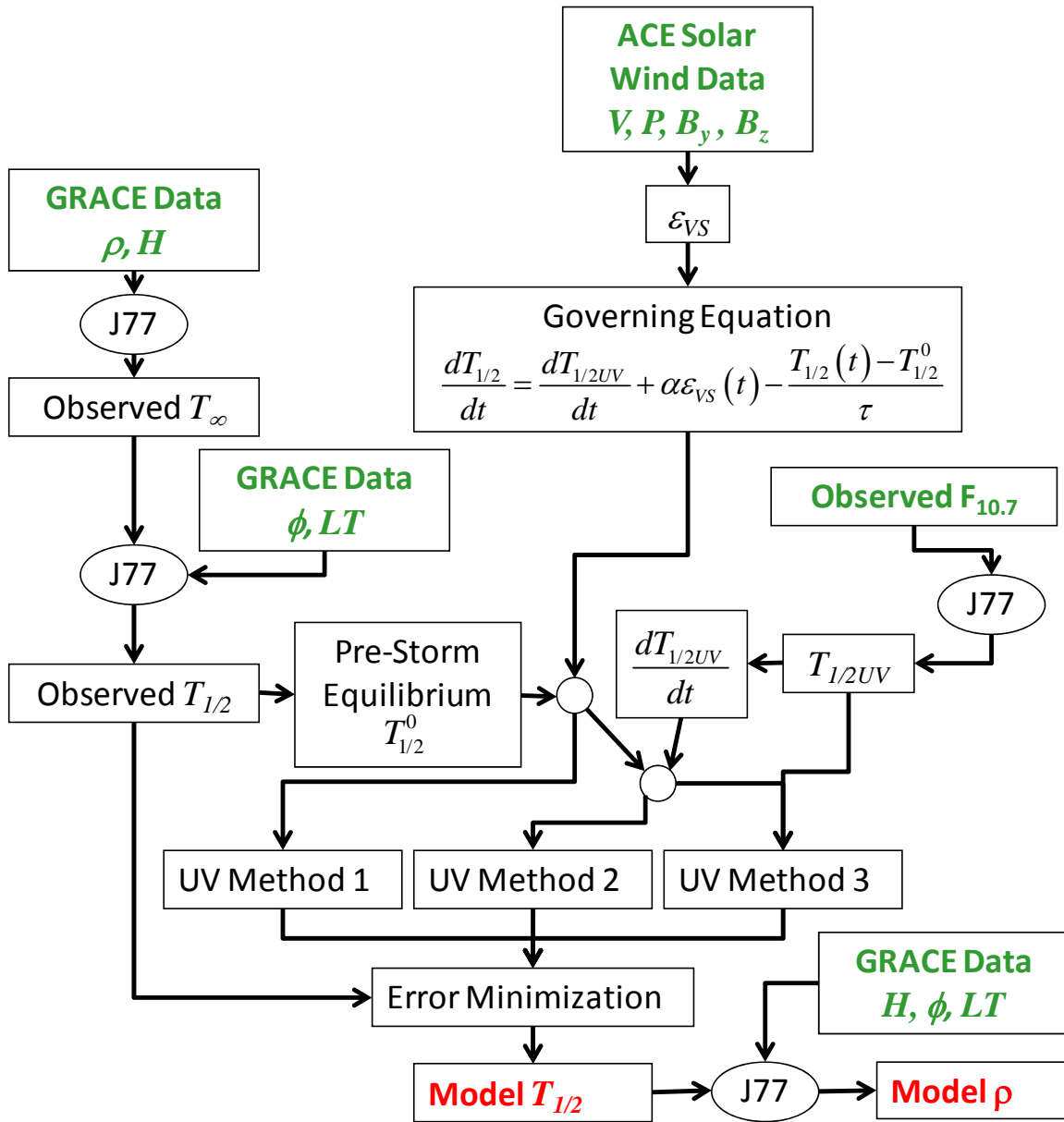
Figure 10: Schematic of the Driven-Dissipative model used in this Thesis. Green text indicates observed model inputs. Red text indicates model outputs.

Observed Data

Burke, 2011 conducted a study of 38 geomagnetic storms from 2002 through 2008 using the methods outlined above from Burke et al., 2009. The storms were selected based on the availability of the solar wind data necessary to compute magnetospheric electric field values. These same storm periods were used in this thesis, with one exception. One of the storms used by Burke, 2011 (Julian Date 168-170, 2003) did not have solar wind data available at the one-minute time cadence used for this thesis. This storm was replaced by a storm from Julian Date 94 - 98, 2004 which was not studied by Burke, 2011. The storm start times, end times, and storm types (CME or CIR-driven) for storms used in this thesis are listed in Table 1. The following sections outline how the observed data in the model was obtained.

Storm Period

The start of a geomagnetic storm is usually defined in part by an increase in solar wind speed and/or density coupled with a southward Z-component of the solar wind magnetic field (B_z south). Using the initial days listed in Burke, 2011 for each storm period as a starting point the time of this increase was determined for each storm. The storm starting time was defined as the last time the GRACE satellite crossed the equator on an ascending pass prior to the increase in solar wind speed and/or density. The end of the storm period was generally defined as the final day listed by Burke, 2011. In some cases, that time was clearly after both the magnetospheric electric field and GRACE-derived exospheric temperature had recovered to a state of quasi-equilibrium near pre-storm levels. In these cases the storm end time was adjusted backwards to match

38

Table 1: Storm Periods Studied

Year	Storm Start				Storm End				Storm Type
	Day	**Hour**	**Min**	**Sec**	**Day**	**Hour**	**Min**	**Sec**	
2002	246	18	16	59	248	0	0	0	CME
2002	250	13	35	35	252	0	0	0	CME
2002	272	23	56	57	275	16	48	0	CIR
2002	276	9	47	28	278	0	0	0	CIR
2002	296	22	24	0	299	0	0	0	CIR
2002	324	14	23	18	327	0	0	0	CIR
2003	149	12	22	43	151	0	0	0	CME
2003	229	14	1	55	232	0	0	0	CIR
2003	324	6	54	25	326	0	0	0	CME
2004	22	0	37	57	24	0	0	0	CME
2004	94	0	54	55	98	0	0	0	CIR
2004	204	9	53	59	210	0	0	0	CME
2004	208	22	10	40	210	0	0	0	CME
2004	243	1	12	42	246	0	0	0	CIR
2004	312	9	44	47	314	0	0	0	CME
2004	314	10	22	30	316	0	0	0	CME
2005	127	17	35	50	130	0	0	0	CIR
2005	135	4	20	33	136	0	0	0	CME
2005	148	4	20	25	152	0	0	0	CME
2005	163	8	4	12	165	0	0	0	CIR
2005	236	0	53	0	239	0	0	0	CME
2005	243	8	26	32	245	0	0	0	CIR
2006	98	10	5	11	100	19	33	36	CIR
2006	103	4	29	30	107	0	0	0	CIR
2006	348	14	1	20	350	0	0	0	CME
2007	142	7	30	53	148	9	36	0	CIR
2007	191	20	17	30	193	0	0	0	CIR
2007	195	7	18	0	197	0	0	0	CIR
2007	218	12	52	5	221	0	0	0	CIR
2007	298	9	50	7	305	0	0	0	CIR
2007	323	17	29	20	325	21	14	24	CIR
2007	351	3	12	50	356	0	0	0	CIR
2008	31	13	9	13	37	0	0	0	CIR
2008	68	9	55	30	71	0	0	0	CIR
2008	86	2	17	0	91	0	0	0	CIR
2008	166	17	38	35	170	0	0	0	CIR
2008	194	0	8	55	195	0	0	0	CIR
2008	247	2	40	2	250	0	0	0	CIR

observations. Temperatures derived from observed GRACE density and height values are

referred to as observed temperature values for the remainder of the thesis. Figure 11

shows an example of a typical storm period.
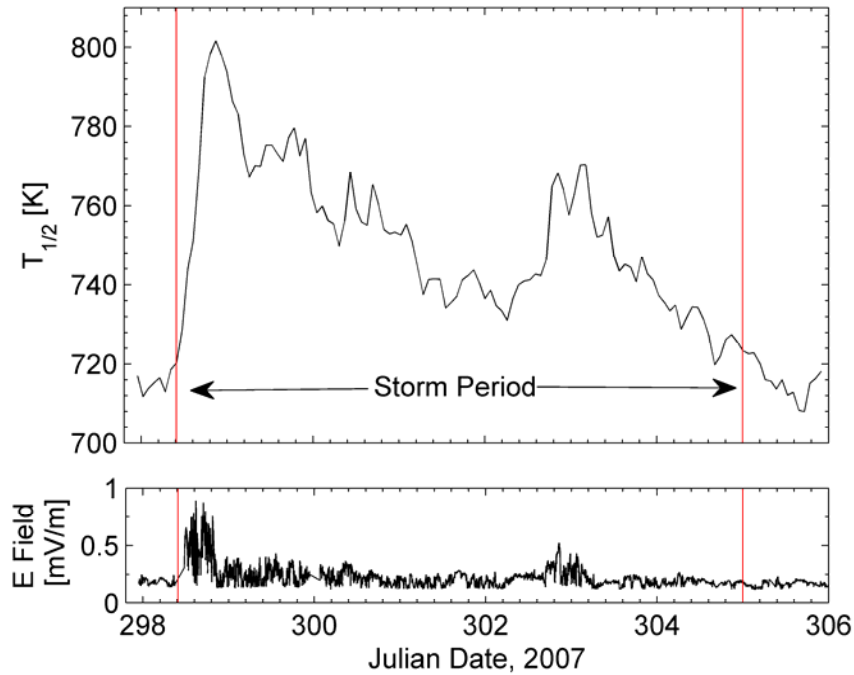
Figure 11: Example of a storm period, defined as the start time of the GRACE orbit just prior to the initial electric field rise until both the electric field and the observed $T_{1/2}$ have returned to quasi-equilibrium near their pre-storm values. Observed GRACE $T_{1/2}$ (top) and magnetospheric electric field data (bottom) are shown as functions of Julian date (JD), 2007 where JD is counted from 1 Jan, 2007. The red vertical lines indicate the storm start time (left) and storm end time (right).

Exospheric Temperature

Once the storm periods were determined, data from the GRACE A satellite was

used to calculate the exospheric temperature, T_∞. The GRACE A satellite was in a polar

orbit at altitudes from 455-534 km during the period from 2002-2008. The GRACE data

set used for this thesis was calibrated by Sutton, 2011 with thermospheric parameters

averaged into 3 degree latitude bins. For this research neutral density, altitude, latitude and local time were used. Burke et al., 2009 used an earlier calibrated version of GRACE data (Burke, 2011) that was not averaged into latitude bins. His approach was to orbit-average the density and altitude from raw GRACE data first, and then calculate the orbit-averaged T_∞ using Equations (6) and (7). Wise et al., 2012 showed that this method of orbit averaging produced inaccurate results. The GRACE satellite orbit is slightly non-circular with an apogee about 20km higher than perigee. Orbital dynamics dictate that the satellite moves slower near apogee than perigee. This results in underestimates of orbit-average density and orbit-average heights higher than the time-independent average. Combined, these factors lead to underestimates of orbit-averaged T_∞ when it is calculated from orbit-averaged heights and densities (Wise, et al., 2012).

Wise et al., 2012 showed that a more physically accurate way to calculate orbit-averaged T_∞ is to calculate T_∞ in each GRACE 3-degree latitude bin and then average the result. In this thesis I used the approach of Wise, 2012 and computed exospheric temperature for each latitude bin prior to the orbit averaging, resulting in an observed T_∞ for each GRACE latitude bin. The change in technique does impact the resulting observed orbit-average temperature values and results are shown in section IV.

The method to compute exospheric temperature used by Burke et al., 2009 (Equations (6) and (7)) is taken from Burke's (2008) quadratic fit to the J77 model. This fit was developed to be accurate only within the ranges of 300 – 500 km in altitude and 700 – 2000 K in T_∞ which leaves open the possibility that the fit is not sufficiently accurate over the entire temperature range present in the 38-storm sample listed in Table

41

1. To quantify and correct this possible source of error an interpolation/iteration technique was developed to produce an exospheric temperature that, coupled with the GRACE altitude, produces the observed GRACE density via the J77 model. To begin, tables of data from the J77 model were generated using a Fortran code written by David Huestis in 1999 and provided by John Wise at the Air Force Research Laboratory. Data tables list densities as a function of altitude for a given exospheric temperature. Tables were generated for exospheric temperatures from 500-2000K with a resolution of 100K, listing densities for altitudes of 300km-1000km with a resolution of 1km.

Data from the J77 tables were used to create a 3-D grid of data giving density for a specified T_∞ - altitude pair. The temperature and altitude ranges chosen ensure that all of the observed GRACE data fit inside the data grid. With the data grid as a basis, a density can be generated using any specified T_∞, altitude pair by interpolating between the data points. For this thesis, cubic spline interpolation (Press, et al., 2007) was used via MATLAB's interp2 function. To generate observed exospheric temperatures from observed GRACE heights and densities an iterative technique, the Nelder-Mead simplex direct-search method (Lagarias, et al., 1998), was used. Starting at an initial guess for T_∞, here 800K, the search method iterates over T_∞ values until a T_∞ is found that minimizes the relative error (to a tolerance of 10^{-4} %) between the observed density and the interpolated density when paired with the observed altitude. The Nelder-Mead method is detailed in Appendix B.

Thermospheric models like J70, J77 and HASDM use a global temperature parameter to account for the EUV contribution to the thermosphere's energy budget. The

42

J77 uses the arithmetic mean temperature, $T_{1/2}$, defined as the average of the daytime maximum T_∞ and the nighttime minimum T_∞ at a given time. While T_∞ characterizes the thermosphere at a specific location and time, $T_{1/2}$ is general parameter that removes the diurnal variation of T_∞ and characterizes the state of the thermosphere as a whole. The formula from the J77 model (Jacchia, 1977) shown in Equation (18) was used to convert the observed T_∞ values from the GRACE data into $T_{1/2}$.

$$T_{1/2} = \frac{T_\infty}{D(\delta, \phi, H)} \tag{18}$$

The conversion factor D is a function of solar declination angle (δ), latitude (ϕ) and solar hour angle (H) and given by Equation (19).

$$D = 1 + c_1 \frac{\delta}{\varepsilon} \sin(\phi) + c_2 \left(f(H) - \frac{1}{2} \right) \cos(\phi) \tag{19}$$

where:

$$f(H) = \cos^3 \left[\frac{1}{2}(H + \beta) \right] + c_3 \cos \left[3(H + \beta) + \chi \right]$$

$$c_1 = 0.15,\ c_2 = 0.24,\ c_3 = 0.08,\ \beta = -60^o,\ \varepsilon = 23.44^o,\ \chi = -75^o$$

Latitude was taken as the mean location of the GRACE satellite in each latitude bin. The hour angle H is simply the mean local time of each latitude bin, converted to an angle counted from local noon via the formula:

$$H = \left(Local\,Time(hours) - 12\right) \times 15^{o} \qquad (20)$$

The solar declination angle (δ) was calculated using the time of each data point via the method described by Meeus, 1991 outlined in Appendix A.

Once observed T_{∞} values were converted to $T_{1/2}$ via Equation (18) in each latitude bin, the observed $T_{1/2}$ data was orbit averaged. The start of each orbit was defined as the equator on each ascending pass of the GRACE satellite. The end of each orbit was defined as the point just before the equator on each ascending pass. All of the $T_{1/2}$ values for each orbit were averaged to produce a single value for each orbit, and the time for each orbit-averaged value was defined as the time of the start of the orbit. The resulting orbit-averaged $T_{1/2}$ values and times were used as the observed data the model attempts to replicate.

Magnetospheric Electric Field

The main source of energy for the thermosphere during geomagnetic storms is the solar wind which couples to the thermosphere via the magnetospheric electric field, ε_{VS}. Using solar wind data from the Advanced Composition Explorer (ACE) satellite, ε_{VS} can be calculated in near real-time using a version of the Volland-Stern model originally formulated by Ejiri, 1978 and modified by Burke, 2007. The ACE satellite is located at the L1 Lagrange point between the Sun and the Earth which is roughly one hour upstream of the Earth in the solar wind flow. For this thesis ACE data that had already been time shifted, meaning the time stamp on the data was adjusted by roughly one hour to account for the transit time to earth, was utilized. The exact amount of time adjustment

44

depends on the current solar wind velocity. This data is available at a one-minute time cadence from the NASA OMNIWeb. Solar wind pressure, P_{SW}, and velocity, V_{SW}, were obtained from the ACE Solar Wind Electron Proton Alpha Monitor (SWEPAM) while the Y (B_y) and Z (B_z) components of the solar wind magnetic field were obtained from the ACE Magnetic Field Experiment (MFE) sensor. All calculations and data use GSM coordinates, illustrated in Figure 2.

Using Burke's (Burke, 2007) formulation, the magnetospheric electric field magnitude can be calculated using the relation

$$\varepsilon_{VS} = \frac{\Phi_{PC}}{2L_Y R_E} \tag{21}$$

The denominator in Equation (21) gives the width of the magnetosphere in the Y direction. R_E is the radius of earth and L_Y is the distance to the magnetopause in the Y direction, in earth radii, calculated using the solar wind pressure with Equation (22).

$$L_Y = \frac{14.4}{\sqrt[6]{P_{SW}\left(nPa\right)}} \tag{22}$$

The numerator in Equation (21), Φ_{PC}, is the cross-polar cap electric potential. Siscoe et al., 2002 built on the Hill model (Hill, 1984) and developed a formula for Φ_{PC} using the magnetospheric saturation potential, Φ_S, and the magnetospheric convection potential, Φ_E as inputs.

$$\Phi_{PC} = \frac{\Phi_E \Phi_S}{\Phi_E + \Phi_S} \tag{23}$$

Equation (23) shows that Φ_S serves as a limiting value for Φ_{PC}. In other words, when

$\Phi_E \ll \Phi_S$, $\Phi_{PC} \approx \Phi_E$ while when $\Phi_E \gg \Phi_S$, $\Phi_{PC} \approx \Phi_S$ (Hill, et al., 1976).

Φ_S is the potential that drives region one currents in the magnetosphere which

create magnetic fields that weaken the earth's magnetic field at the magnetopause

(Siscoe, et al., 2002). It can be calculated using the solar wind dynamic pressure (P_{SW})

using the formula

$$\Phi_S = \frac{1600 \sqrt[3]{P_{SW}(nPa)}}{\Sigma_P(mho)} \tag{24}$$

where Σ_p is the effective Pedersen conductance of the polar cap, here approximated as a

constant $\Sigma_p = 10 \, mho$ (Burke, 2007). We see that increased solar wind pressure results

in a greater magnetospheric saturation potential.

Φ_E results from magnetic reconnection processes at the magnetopause

(Boudouridis, et al., 2004). It can be calculated using the solar wind velocity and

magnetic field data via Equation (25)

$$\Phi_E = \Phi_o + L_G V_{SW} B_T \sin^2\left(\frac{\theta}{2}\right) \tag{25}$$

where the first term, Φ_o, is a residual potential due to viscosity in the low-latitude

boundary layer (Burke, 2007), (Kennel, 1995). Burke found that Φ_o typically ranges

between 20 and 30 kV (Burke, et al., 1999) and for this research the value of Φ_o was set

at 25 kV. The second term in Equation (25), $V_{SW} B_T \sin^2 \frac{\theta}{2}$, gives the magnitude of the

interplanetary electric field as developed by Sonnerup, 1976, where V_{SW} is the solar

wind velocity, $B_T = \sqrt{B_Y^2 + B_Z^2}$ and $\theta = \cos^{-1} \frac{B_Z}{B_T}$, the interplanetary electric field clock

angle in the Y-Z plane. The interplanetary electric field multiplied by L_G, the width of the

space (in Earth radii) through which geoeffective solar wind streamlines must pass to

reach the dayside magnetopause (Burke, 2007), gives the interplanetary electric potential.

Typically L_G values between 3 – 4 Earth radii and in this research the approximation is

made that $L_G = 3.5$, a constant, as suggested by Burke et al., 1999.

Data from the ACE satellite is occasionally either bad or missing. When missing

or bad data made reliable electric field values impossible to calculate directly,

interpolation was used between the nearest good data points to fill in the gap and ensure

good electric field values existed for each minute during storm time. Because storm

periods were selected based on relatively good ACE data availability, the amount of

interpolation was kept to a minimum. None of the storms studied had contiguous gaps in

ACE data of longer than four hours and none of the storms studied had missing ACE data

at the time of peak observed temperatures. Figure 12 shows an example of the ACE solar

wind data and the magnetospheric electric field magnitude calculated using the above

formulation for a geomagnetic storm in July, 2004.
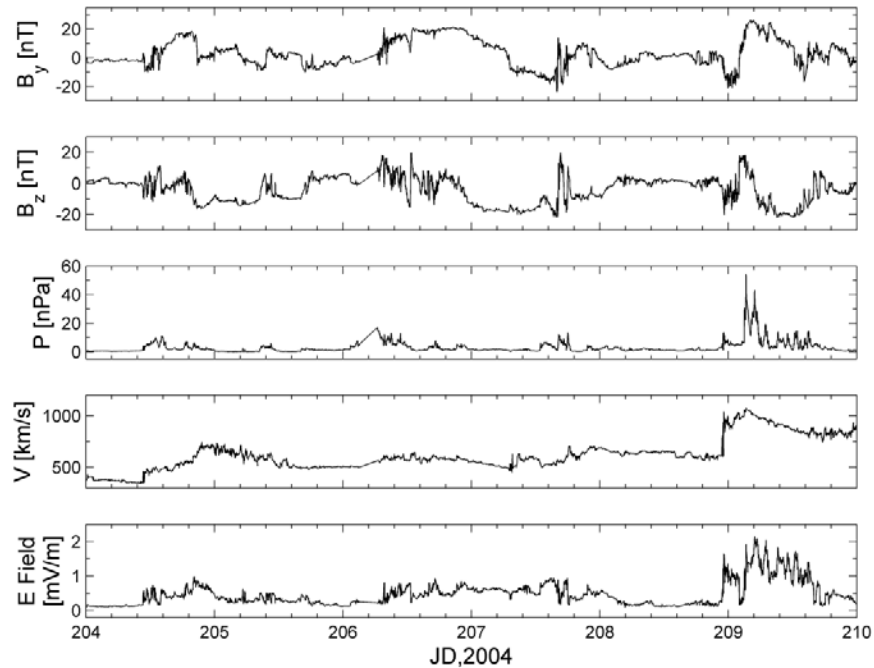
Figure 12: Illustration of ACE solar wind data and the resultant magnetospheric electric field magnitude. From top to bottom the figure shows the y and z components of the interplanetary magnetic field (B_y and B_z) in nano-Teslas, the solar wind pressure (P) in nano-Pascals, the solar wind velocity (V) in km/s, and the magnetospheric electric field magnitude (E field) in miliVolts/meter as functions of modified Julian date (JD), 2004 where JD is counted from 1 Jan, 2004.

Governing Equation

Burke's original model (Burke, et al., 2009) assumed that the UV contribution to the exospheric temperature was constant throughout the storm period. It is true that during storm time, the geomagnetic contribution to thermospheric energy and therefore exospheric temperature is much more variable than the UV contribution. However, since the sun's UV irradiance can change on short time scales as well, a more realistic model would allow the UV contribution to vary during storm time. Since the J77 model accounts for the UV contribution via the arithmetic mean temperature ($T_{1/2}$), $T_{1/2}$ is modeled via a new differential equation governing its time rate of change.

48

Since $T_{1/2}$ differs from T_∞ by only a conversion factor shown in Equation (18), $T_{1/2}$ can be expressed as the sum of UV and solar wind contributions just as T_∞ was by Burke in Equation (11).

$$T_{1/2} = T_{1/2\,UV} + T_{1/2\,SW} \qquad (26)$$

Likewise the time rate of change of $T_{1/2}$ is simply the sum of the time rates of change of its components.

$$\frac{dT_{1/2}}{dt} = \frac{dT_{1/2\,UV}}{dt} + \frac{dT_{1/2\,SW}}{dt} \qquad (27)$$

Just prior to storm time the thermosphere is taken to be at equilibrium with $\frac{dT_{1/2}}{dt} = 0$ and

$$T_{1/2} = T_{1/2}^0 = T_{1/2\,UV}^0 + T_{1/2\,SW}^0 \qquad (28)$$

Equation (28) expresses the pre-storm equilibrium arithmetic mean exospheric temperature ($T_{1/2}^0$) as the sum of the equilibrium UV and solar wind contributions. In general, outside geomagnetic storming periods, the UV contribution to thermospheric energy is much larger than the solar wind contribution (Figure 1), which indicates that $T_{1/2UV}^0 \gg T_{1/2SW}^0$ suggesting the approximation $T_{1/2UV}^0 = T_{1/2}^0$.

Using Burke's (Burke, et al., 2009) expression for $\frac{dT_{1/2SW}}{dt}$ given by Equation (13) and substituting $T_{1/2SW} = T_{1/2} - T_{1/2}^0$, Equation (27) becomes

$$\frac{dT_{1/2}}{dt} = \frac{dT_{1/2\,UV}}{dt} + \alpha \varepsilon_{VS}(t) - \frac{T_{1/2}(t) - T_{1/2}^0}{\tau} \qquad (29)$$

49

where α is a coupling constant linking the magnetospheric electric field (ε_{VS}) to $T_{1/2}$ and τ is a relaxation constant. Solving Equation (29) using Euler's method provides a model of $T_{1/2}$ as a function of time to compare with the observed data from GRACE.

UV contribution to $T_{1/2}$

Equation (29) shows that any solution for $T_{1/2}$ depends on the ways in which both $T_{1/2UV}$ and $T_{1/2}^0$ are treated. They can be treated as constants through the storm period or allowed to vary. If they are variable, a method of calculating their value must be selected. The following sections outline the three ways in which $T_{1/2UV}$ and $T_{1/2}^0$ are treated for this research.

Method One

The simplest way to treat $T_{1/2UV}$ and $T_{1/2}^0$ is to approximate them as constants through the storm period. This is the method Burke et al., 2009 used in their original model. In method one, $\frac{dT_{1/2UV}}{dt} = 0$ at all times and Equation (29) becomes

$$\frac{dT_{1/2}}{dt}(t) = \alpha\varepsilon_{VS}(t) - \frac{T_{1/2}(t) - T_{1/2}^0}{\tau} \tag{30}$$

Solving Equation (30) via the Euler method results in a time dependent formula for $T_{1/2}$ shown in Equation (31).

$$T_{1/2}(t + \Delta t) = T_{1/2}(t) + \Delta t \left[\alpha\varepsilon_{VS}(t) - \frac{T_{1/2}(t) - T_{1/2}^0}{\tau} \right] \tag{31}$$

50

In method one, $T_{1/2}^0$ was defined as the mean of the observed arithmetic mean exospheric temperature from the 8 GRACE orbits ($\cong$12 hrs) prior to the storm start time and considered constant throughout the storm. A time step (Δt) of 1 minute was used to match the cadence of the ACE-derived magnetospheric electric field data.

Method Two

In method two the pre-storm equilibrium temperature, $T_{1/2}^0$, was still considered to be constant throughout the storm period and defined identically to method one. However, $\frac{dT_{1/2UV}}{dt}$ was allowed to be non-zero in Equation (29). Solving Equation (29) with a non-zero $\frac{dT_{1/2UV}}{dt}$ via the Euler method with a one-minute time step results in the time-dependent expression for $T_{1/2}$ used in method two.

$$T_{1/2}\left(t+\Delta t\right)=T_{1/2}\left(t\right)+\Delta t\left[\frac{dT_{1/2UV}}{dt}\left(t\right)+\alpha_T\varepsilon_{VS}\left(t\right)-\frac{T_{1/2}\left(t\right)-T_{1/2}^0}{\tau}\right] \tag{32}$$

To account for the variation in the UV contribution to the exospheric temperature, the J77 model calculates $T_{1/2UV}$ as a function of the $F_{10.7}$ index using the formula

$$T_{1/2UV}\left(t\right)=5.48\left(F_{10.7a}\right)^{0.8}+101.8\left(F_{10.7}\right)^{0.4} \tag{33}$$

where $F_{10.7}$ is simply the daily value of the $F_{10.7}$ index and $F_{10.7a}$ is an 162-day averaged value of the $F_{10.7}$ index. Using the results of Equation (33), the time rate of change of $T_{1/2UV}$ was calculated for each minute during the storm period using Equation (34).

51

$$\frac{dT_{1/2\,UV}}{dt}(t) = \frac{T_{1/2\,UV}(next\ observation) - T_{1/2\,UV}(prior\ observation)}{24\,hrs} \tag{34}$$

Equation (34) results in a value for $\frac{dT_{1/2UV}}{dt}$ for each minute during the storm period with

units of $\frac{K}{hr}$. The J77 formulation for $T_{1/2UV}$ in Equation (33) results in values for $\frac{dT_{1/2UV}}{dt}$

that are constant, but not necessarily zero, for 24 hour periods between $F_{10.7}$ observations

at 20Z each day.

Method Three

In method three, $\frac{dT_{1/2UV}}{dt}$ was allowed to vary using Equations (33) and (34) in the

same way as method two. $T_{1/2}^0$ was also allowed to vary by approximating

$T_{1/2}^0 = T_{1/2UV}^{cor}$, where $T_{1/2UV}^{cor}$ is a corrected version of $T_{1/2UV}$. To obtain values for

$T_{1/2UV}^{cor}(t)$ at a one-minute time cadence, the J77 formula for $T_{1/2UV}$ was used (Equation

(33)) to calculate a value for $T_{1/2UV}$ at 20Z each day and then interpolated to produce a

value at each minute during the storm period. Because Equation (33) is a modeled input,

it does not always match the observed value of $T_{1/2}^0$, as defined in method one, at the

beginning of the storm period. To remove this discrepancy a correction factor, K, was

added to the modeled value of $T_{1/2UV}$ at each time

$$T_{1/2\,UV}^{cor}(t) = T_{1/2\,UV}(t) + K \tag{35}$$

where $T_{1/2UV}(t)$ is the result of Equation (33) after interpolation and K is given by

$$K = T_{1/2\,UV}^{0,\text{observed}} - T_{1/2\,UV}^{0,\text{modeled}} \tag{36}$$

In Equation (36) $T_{1/2UV}^{0,observed}$ is the observed pre-storm equilibrium temperature defined in

method one and $T_{1/2UV}^{0,modeled}$ is the modeled value of the exospheric temperature, using

Equation (33) and interpolation, at the start of the storm period.

The approximation $T_{1/2}^0 = T_{1/2UV}^{cor}$ results in a modified version of Equation (29)

to be used for method three, given by Equation (37).

$$\frac{dT_{1/2}}{dt}(t) = \frac{dT_{1/2\,UV}}{dt}(t) + \alpha \varepsilon_{VS}(t) - \frac{T_{1/2}(t) - T_{1/2\,UV}^{cor}(t)}{\tau} \tag{37}$$

Solving Equation (37) with Euler's method using a one-minute time step results in the

time-dependent expression for $T_{1/2}$ used in method three.

$$T_{1/2}(t + \Delta t) = T_{1/2}(t) + \Delta t \left[\frac{dT_{1/2\,UV}}{dt}(t) + \alpha \varepsilon_{VS}(t) - \frac{T_{1/2}(t) - T_{1/2\,UV}^{cor}(t)}{\tau} \right] \tag{38}$$

Orbit Averages

Because the observed $T_{1/2}$ data from GRACE that the model is attempting to

replicate is averaged over the period of an orbit, the modeled data needs to be averaged

over the same time periods to facilitate direct comparison. After modeled $T_{1/2}$ values are

calculated for each minute of the storm period using one of the three methods above the

modeled values were averaged over the same time periods defined earlier by the GRACE

orbits. The time stamp for each averaged value is taken to be the start of the average period, which is equivalent to the start of the GRACE orbit used for the observed data.

Coupling Constant and Relaxation Constant

The last piece of the model that must be determined is the value of the coupling constant, α, and the relaxation constant, τ, in Equations (31), (32), and (38) for methods one, two and three respectively. The values of both α and τ were considered constant through each storm period but were allowed to have different values for each storm period and for each method. To determine the optimal value of α and τ for each storm period, the MATLAB fminsearch function was used to minimize the relative root-mean-squared (RMS) error, defined by Equation (39), between the observed and modeled values of $T_{1/2}$ by adjusting the values of α and τ .

$$Relative\, T_{1/2}\; RMS\; Error = \sqrt{\frac{1}{N}\sum \frac{\left(T_{1/2}^{\;observed} - T_{1/2}^{Model}\right)^2}{\left(T_{1/2}^{\;observed}\right)^2}} \qquad (39)$$

Here $T_{1/2}^{observed}$ denotes the orbit-averaged observed $T_{1/2}$ values derived from GRACE data, $T_{1/2}^{Model}$ denotes the orbit-averaged model $T_{1/2}$ values using one of the methods described above and N is the number of data points during the storm period. The MATLAB fminsearch function uses the Nelder-Mead simplex direct search method (Lagarias, et al., 1998) to minimize a given function. The algorithm is outlined in Appendix B. Using this procedure optimal values for α and τ were determined for each storm period and each method, along with the resulting relative RMS error.

54

Density Conversion

  The main purpose of the driven-dissipative model is to show the relevance of using the magnetospheric electric field to model the energy input to the thermosphere during geomagnetic storming. This is accomplished by modeling orbit-averaged $T_{1/2}$. However, since there are no published temperature errors for current thermospheric models such as HASDM, the temperature errors from the driven-dissipative model cannot be directly compared to existing thermospheric models. In order to facilitate comparisons with published mean HASDM density errors of 17% during geomagnetic storming (Marcos et al., 2010) the model $T_{1/2}$ results must be used to generate model density values. In an operational application, this would be done by using the driven-dissipative method or model $T_{1/2}$ output in a current thermospheric model such as HASDM or JB08. For the purpose of assessing the relationship between $T_{1/2}$ errors and density errors, the J77 model can be used to generate model densities from model $T_{1/2}$ values.

  The model used in this thesis is designed to minimize the error between observed and modeled orbit-average $T_{1/2}$ values, not the error between modeled and observed $T_{1/2}$ at any given point and time. Observed $T_{1/2}$ values reflect the GRACE satellite's latitude while model $T_{1/2}$ values do not exhibit this same variation. Instead they are generated by the Equation (38) which produces $T_{1/2}$ as a function of time that, while not matching the latitudinal variation of the observed $T_{1/2}$, results in orbit-average values very close to those observed. This relationship is shown in Figure 13. The observed $T_{1/2}$ values (blue line) vary as a function of latitude (bottom plot) while the modeled $T_{1/2}$ values (red line)

do not. Despite this difference, orbit-averaged observed $T_{1/2}$ values (blue x's) agree well

with model orbit-averaged $T_{1/2}$ values (red dots).
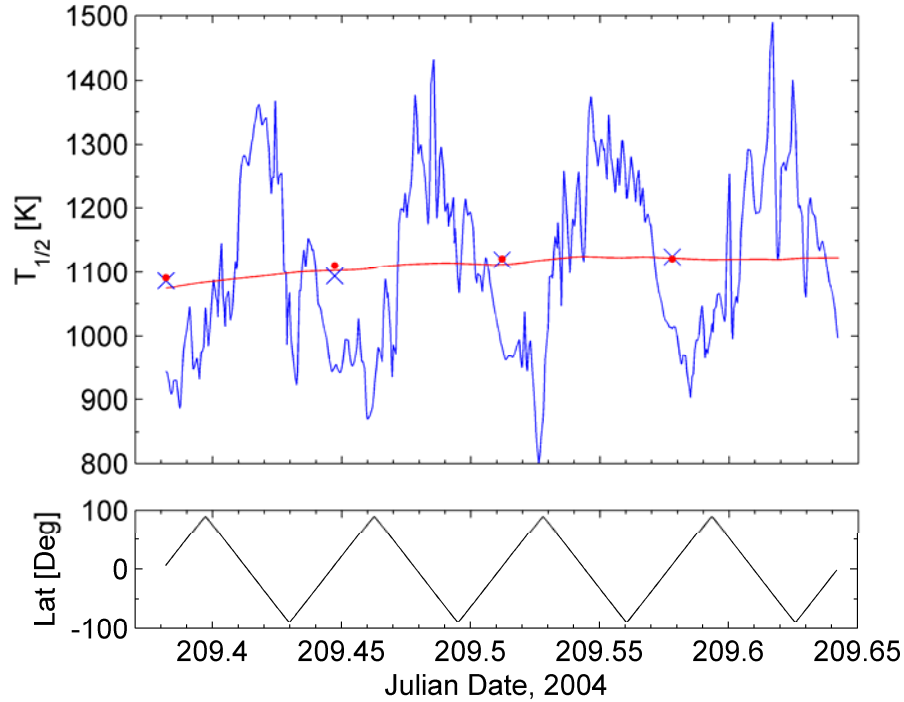
Figure 13: Illustration of the latitudinal dependence of observed (blue) and modeled (red) $T_{1/2}$ values. The top plot shows observed $T_{1/2}$ values in each GRACE latitude bin (blue line) and raw modeled $T_{1/2}$ values at a one minute time cadence (red line). Orbit-averaged observed $T_{1/2}$ values are shown as blue x's and orbit-averaged model $T_{1/2}$ values are shown as red dots. The bottom plot shows that Latitude of the GRACE satellite as a function of Julian Date, 2004.

Since the model is not formulated to accurately model $T_{1/2}$ in each GRACE

latitude bin, the model cannot be expected to accurately model density in each GRACE

latitude bin. This means that the orbit-averaging method used previously, where values

were computed for each latitude bin and then averaged over an orbit, cannot be used

when converting model $T_{1/2}$ into model density values. Instead, to generate orbit-average

model densities, orbit-average model $T_{1/2}$ values are used. Since the J77 model tables list

56

density as a function of T_∞ and height, model orbit-averaged $T_{1/2}$ is converted to model orbit-averaged T_∞ via Equation (40)

$$\overline{T}_{\infty,\text{mod}} = \overline{T}_{1/2,\text{mod}} \cdot \overline{D} \tag{40}$$

where $\overline{T}_{\infty,mod}$ is the modeled orbit-averaged T_∞, $\overline{T}_{1/2,mod}$ is the modeled orbit-averaged $T_{1/2}$, and $\overline{D}$ is the observed orbit-averaged conversion factor from the J77 model calculated via Equation (19).

Once $\overline{T}_{\infty,mod}$ was calculated it was paired with the corresponding observed GRACE orbit-averaged height to generate model orbit-averaged density via interpolation within the J77 model tables. Using this process, model orbit-averaged density was calculated for each storm and then compared to the observed GRACE orbit-averaged density to calculate the relative density RMS error via Equation (41)

$$Relative\ Density\ RMS\ Error = \sqrt{\frac{1}{N}\sum \frac{\left(\overline{\rho}_{ob} - \overline{\rho}_{\text{mod}}\right)^2}{\overline{\rho}_{ob}{}^2}} \tag{41}$$

where $\overline{\rho}_{ob}$ is the observed orbit-averaged density, $\overline{\rho}_{mod}$ is the modeled orbit-averaged density and N is the number of data points.

57

IV. Analysis and Results

Chapter Overview

Section IV begins with a comparison of the method used by Burke et al., 2009 to derive observed exospheric temperatures from GRACE data with the method developed for this thesis. Second, results are presented using the three model methods for the 38 storms in the sample. Results from three individual storms are presented in detail and the results of the different methods are compared. Model results are compared with the results from Burke, 2011 and differences are discussed. Next, values for α and τ determined for each storm are fit as functions of $F_{10.7a}$ in an effort to make the model operationally useful. Results of the fits are presented. To test general applicability, the model is applied to two storms outside the original sample of 38. Finally, model temperature values are converted to model density values and the resulting errors are compared with published HASDM density errors.

Observed Data

Before running the model, observed temperature values need to be determined from GRACE data. As discussed in section III, Burke's approach (2009) was to calculate orbit-averaged values of height and density from raw GRACE data and then calculate an orbit-averaged T_∞ value. Wise et al., 2012 showed that calculating orbit-averaged T_∞ from orbit-averaged density and height data produces an inaccurate result due to the fact that GRACE orbits are slightly non-circular. Instead, the more accurate approach is to average GRACE density and altitude into 3-degree latitude bins, calculate T_∞ for each

58

GRACE latitude bin, and then orbit-average the resulting values. Wise's approach to orbit-averaging values is applied here.

After calculating orbit-averaged density and height values, Burke et al., 2009, applied the quadratic fit to the J77 model given in equations (6) and (7) to calculate the orbit-averaged T_∞ values. This fit was developed to provide good results for heights within the range from 300 to 500 km and for T_∞ from 700 to 2000 K (Burke, 2008). For the storms sampled in this thesis, GRACE heights range from 455-534 km and T_∞ ranged from roughly 500K – 1400K. Since the GRACE data for the storm sample does not fit entirely within the range treated well by the quadratic fit a test was run to determine if the quadratic fit would produce accurate results for all storms. To compare the results of Burke's quadratic fit with the J77 model, T_∞ was calculated for each GRACE latitude bin in 2004 using Burke's quadratic fit given in equations (6) and (7) and using the interpolation/iteration technique with J77 model tables described in section III. Resulting values of T_∞ were then orbit averaged. While the J77 table interpolation/iteration technique is much more computationally intensive than the quadratic fit, it produces a more accurate representation of the true J77 model output because it includes a maximum error tolerance described in section III.

Figure 14 shows the orbit-averaged exospheric temperature values resulting from Burke's quadratic fit (red) and the J77 interpolation/iteration technique (black) for all of 2004. Burke's fit exhibits significantly less variation than the J77 interpolation/iteration method, especially when temperatures drop below 850K or rises above 1000K.

59
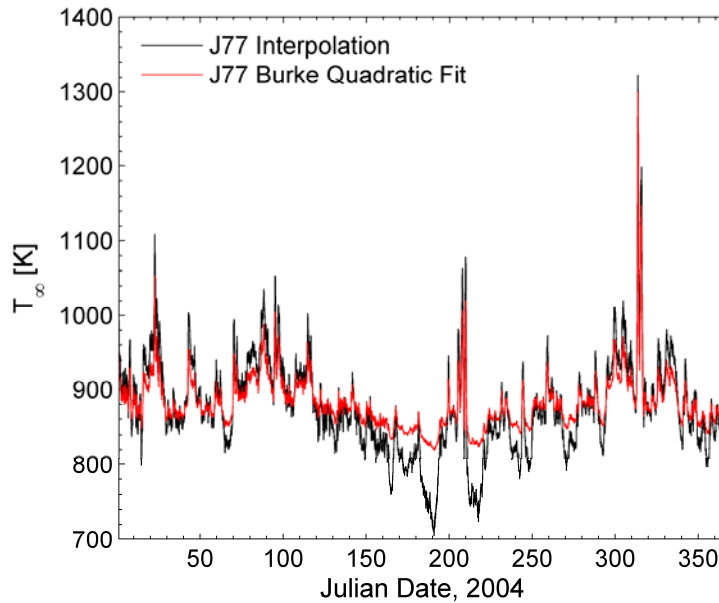
Figure 14: Comparison of the orbit-averaged exospheric temperature resulting from Burke's quadratic fit to the J77 model (red) and the J77 interpolation/iteration method developed for this thesis (black) as a function of Julian Date, 2004 where the date is counted from 1 January, 2004.

Figure 15 shows the quadratic fit results ($T_{\infty,Burke}$), plotted as a function of the interpolation/iteration results ($T_{\infty,Interp}$). If the methods produced equivalent results, all data would fall along the line with a slope of one and a y-intercept of zero shown as a black dashed line. Burke's fit only closely matches the J77 tables in a narrow range around 850K. Above this value Burke's fit produces temperatures lower than the J77 tables and below this value Burke's fit produces temperatures significantly higher than J77 tables. Because the quadratic fit does not closely match the J77 interpolation/iteration technique over the whole range of temperatures, and departs significantly for the low temperatures below 850K that are common near solar min from 2006-2008, the J77 interpolation/iteration technique was used to generate the observed GRACE temperatures

used in this thesis. T_∞ was calculated for each GRACE latitude bin and converted to $T_{1/2}$ using Equation (18). The temperature values were then orbit-averaged.
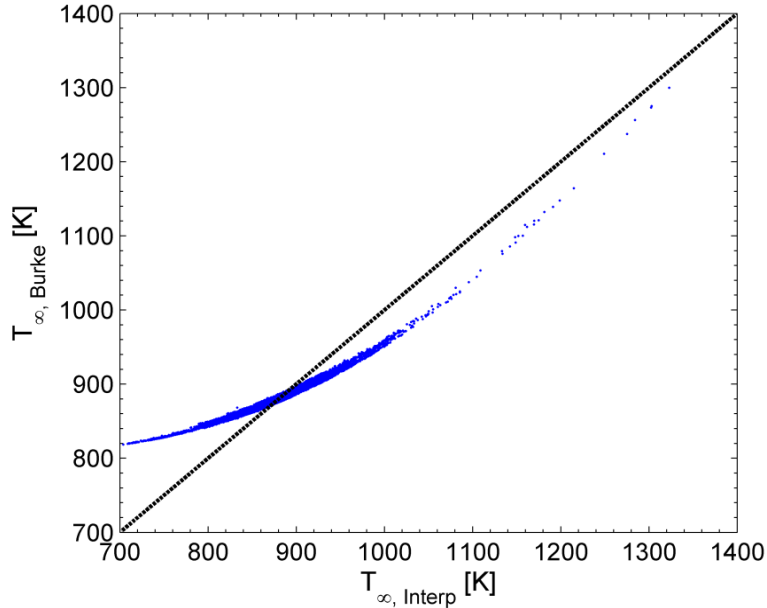
Figure 15: Orbit-averaged exospheric temperature from Burke's J77 quadratic fit ($T_{\infty,Burke}$) plotted as a function of orbit-averaged exospheric temperature from the J77 interpolation/iteration method ($T_{\infty,Interp}$) is shown with blue dots. Data shown is from 2004. The dotted black line has a slope of 1 and a y-intercept of 0.

Model Results

Using the observed orbit-average $T_{1/2}$ values calculated from GRACE data via the J77 interpolation/iteration technique, the model was run using methods one, two and three described in section III for each storm period listed in Table 1. Table 2 shows the model results. The columns from left to right list the year of the storm, the starting day of the storm, the minimum value of the Dst index during the storm period, the value of the $F_{10.7a}$ index on the first day of the storm, the value of the pre-storm equilibrium temperature ($T_{1/2}^0$), and the change in $T_{1/2UV}$ over the storm period ($\Delta T_{1/2UV}$) defined as the difference between the value of $T_{1/2UV}$ at the end of the storm period and $T_{1/2}^0$. All of

these values are the same for each method. Next values for the coupling constant (α) with units of $\frac{K \cdot m}{hr \cdot mV}$, relaxation constant ($\tau$) with units of hrs, and the relative $T_{1/2}$ RMS error (RMS) in percent resulting from each method for each storm are listed.

Table 2: Model Results

Year	Start Day	Min Dst	$F_{10.7a}$	$T_{1/2}{}^0$	Δ $T_{1/2UV}$	Method 1			Method 2			Method 3		
						α	τ	RMS	α	τ	RMS	α	τ	RMS
2002	246	-109	179.0	1214.4	-0.07	39.47	6.80	1.087%	39.61	6.78	1.088%	39.61	6.79	1.087%
2002	250	-181	179.1	1273.2	21.58	67.28	3.64	1.828%	67.82	3.55	1.884%	68.38	3.32	2.332%
2002	272	-176	175.7	1134.5	-5.49	37.93	5.95	1.932%	37.11	6.12	1.921%	36.40	6.18	1.901%
2002	276	-146	175.0	1141.2	31.96	28.65	7.64	0.745%	27.22	7.43	0.750%	31.33	4.97	1.018%
2002	296	-98	174.4	1158.4	18.04	31.95	4.23	1.980%	38.61	3.40	2.066%	36.54	3.55	2.619%
2002	324	-128	174.0	1116.8	-24.16	25.44	4.25	2.631%	26.79	4.18	2.654%	27.02	5.30	2.040%
2003	149	-144	128.8	983.3	-49.18	41.42	3.20	3.715%	37.96	3.68	3.563%	36.02	4.39	2.174%
2003	229	-148	127.7	937.2	-10.75	41.35	6.98	3.599%	42.59	6.85	3.626%	41.79	7.43	3.444%
2003	324	-422	129.2	983.4	17.93	71.14	4.41	3.939%	69.68	4.45	3.960%	70.56	4.18	4.486%
2004	22	-149	126.0	1044.2	-32.74	26.29	5.08	2.122%	26.73	5.26	2.084%	26.29	6.46	1.763%
2004	94	-112	120.8	885.1	-22.38	37.23	7.49	1.452%	36.87	7.71	1.403%	35.46	8.23	1.468%
2004	204	-197	106.4	876.0	-117.63	31.45	7.16	4.456%	30.72	7.82	4.279%	35.32	10.03	3.003%
2004	208	-197	107.7	856.2	-26.60	33.99	6.72	1.603%	34.47	6.84	1.586%	33.62	7.47	1.554%
2004	243	-126	109.1	793.8	7.17	44.63	5.58	2.270%	43.32	5.72	2.331%	41.13	5.76	2.338%
2004	312	-373	109.9	970.0	-10.76	61.12	7.05	1.739%	61.07	7.11	1.746%	60.05	7.34	1.691%
2004	314	-289	110.3	1122.4	-84.39	63.56	2.96	2.731%	59.20	3.34	2.746%	44.58	5.22	1.941%
2005	127	-127	93.5	914.9	28.97	46.38	5.88	2.354%	48.74	5.47	2.476%	50.14	5.11	3.048%
2005	135	-263	94.0	904.3	3.49	52.88	7.33	2.070%	52.73	7.28	2.056%	52.81	7.19	2.077%
2005	148	-138	94.2	793.7	6.43	26.89	11.96	2.242%	27.39	11.63	2.153%	29.48	10.77	2.164%
2005	163	-106	95.3	830.2	-37.58	30.27	8.27	3.027%	30.13	9.04	2.989%	28.84	11.08	2.610%
2005	236	-216	94.8	802.7	-31.30	46.59	5.33	3.401%	47.46	5.37	3.430%	44.87	6.72	1.926%
2005	243	-131	94.7	797.1	-19.41	47.31	5.33	2.669%	46.68	5.55	2.586%	45.55	6.08	2.076%
2006	98	-80	81.2	839.3	-8.75	22.99	11.51	1.548%	24.20	11.11	1.508%	24.19	12.09	1.483%
2006	103	-111	81.5	816.6	-12.25	31.61	9.09	2.587%	31.62	9.20	2.543%	31.31	9.78	2.336%
2006	348	-146	80.0	788.2	-19.73	35.52	8.81	2.104%	35.35	9.18	2.103%	34.44	9.84	1.961%
2007	142	-63	75.8	725.7	-16.93	20.98	8.11	2.312%	21.88	7.92	2.336%	20.32	10.41	1.686%
2007	191	-39	74.6	758.6	0.63	22.51	12.28	0.830%	22.43	12.28	0.825%	22.43	12.18	0.826%
2007	195	-45	74.5	767.6	-7.36	29.67	8.74	1.058%	30.39	8.71	1.041%	29.99	9.35	0.973%
2007	218	-34	74.0	709.3	-3.11	25.63	9.16	0.973%	25.58	9.26	1.005%	24.87	9.83	0.940%
2007	298	-52	71.5	715.8	-1.67	30.55	5.58	1.571%	30.69	5.56	1.564%	30.90	5.59	1.521%
2007	323	-63	69.9	697.7	-1.70	24.09	12.96	1.973%	23.89	13.15	1.967%	23.79	13.22	1.953%
2007	351	-38	70.5	821.4	-30.61	22.20	5.25	2.470%	22.28	5.48	2.467%	24.32	7.58	1.425%
2008	31	-44	70.3	708.2	-5.25	18.16	13.73	1.308%	18.40	13.64	1.253%	18.64	13.99	1.181%
2008	68	-72	70.4	711.4	1.24	17.99	11.46	1.391%	18.53	11.05	1.404%	18.56	11.21	1.423%
2008	86	-43	70.8	731.7	-13.79	23.28	14.90	0.964%	24.74	14.19	0.905%	25.89	14.53	0.791%
2008	166	-40	70.5	714.7	-3.87	28.66	8.46	0.776%	28.81	8.49	0.798%	27.80	9.29	0.693%
2008	194	-40	69.9	681.9	-1.89	25.57	7.42	0.793%	25.79	7.46	0.792%	25.70	7.70	0.783%
2008	247	-51	69.3	645.1	-3.59	18.47	12.39	1.204%	18.24	12.73	1.198%	17.83	13.28	1.161%

Table 3 lists the mean and standard deviation of α, τ, and the relative $T_{1/2}$ RMS error for each method. The mean values of α, τ and relative RMS error are very similar between methods one and two. The only difference between these two methods is the factor $\frac{dT_{1/2UV}}{dt}$ in Equation (32). Since $\frac{dT_{1/2UV}}{dt}$ is calculated using the 24-hr change in the $F_{10.7}$ index via Equations (33) and (34) it is generally a small term resulting in little difference between methods one and two. Method three has mean alpha values lower than methods one and two and mean tau values slightly higher. The mean relative RMS error for method three is 10% less than that of method one.

Table 3: Model Statistics

	Mean α	Std Dev α	Mean τ	Std Dev τ	Mean RMS	Std Dev RMS	Lowest RMS Storms Number	Lowest RMS Storms Percentage
Method 1	35.03	13.90	7.71	3.07	2.04%	0.94%	7	18%
Method 2	35.15	13.50	7.74	3.01	2.03%	0.93%	4	11%
Method 3	34.65	12.87	8.25	3.05	1.84%	0.80%	27	71%

Figure 16 shows histograms of relative $T_{1/2}$ RMS error values (top), α values (bottom left), and τ values (bottom right) for each of the three methods. Relative RMS error values for methods one and two have a diffuse peak from 1.5 – 2.5%, and a range of 0.76% - 4.46%. The standard deviation is very similar for the two methods: 0.94% for method one and 0.93% for method two. Method three has a stronger relative RMS error peak between 1.5% - 2% but a larger overall range from 0.69% - 4.49%. In general the method three errors are more tightly packed, with a standard deviation of 0.80%.
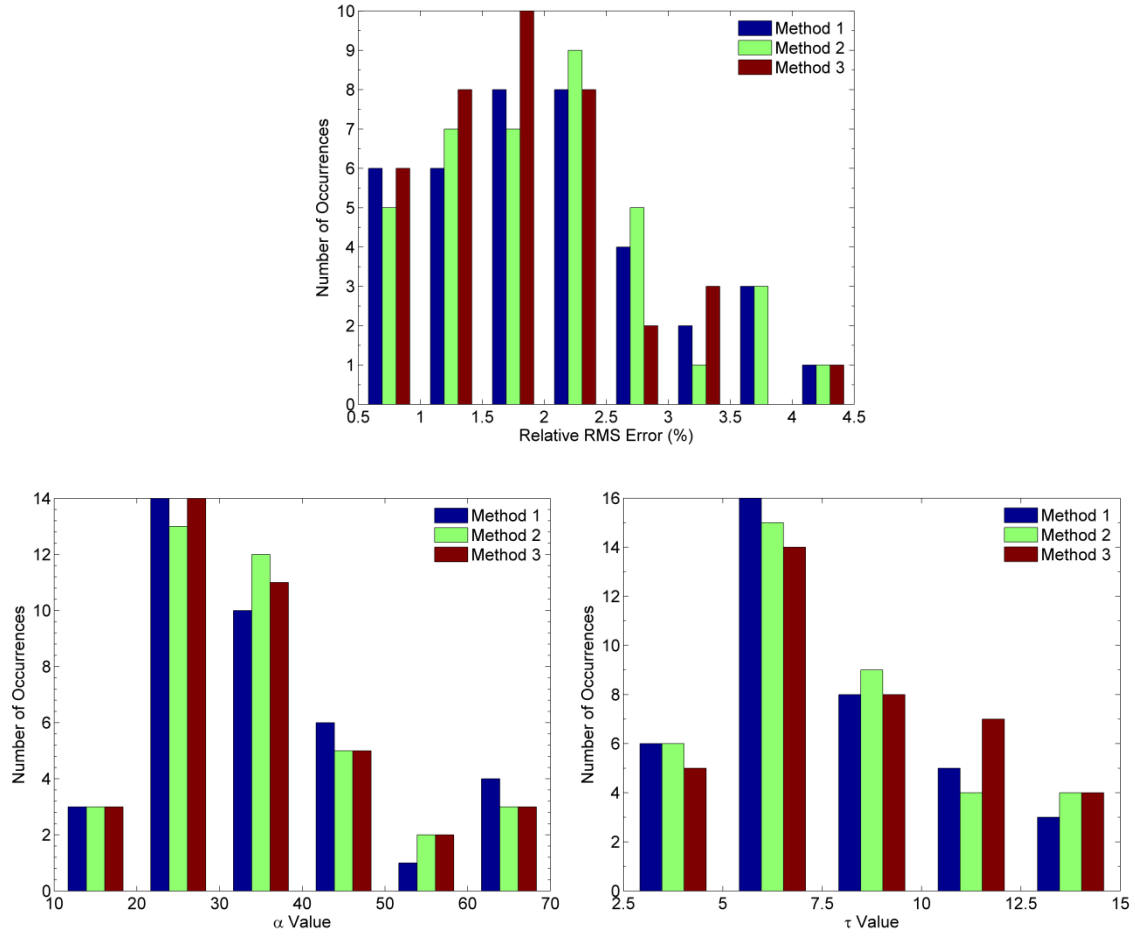
Figure 16: Histograms showing relative T$_{1/2}$ RMS errors (top), α values (bottom left), and τ values (bottom right) for method one (blue), method 2 (green), and method 3 (maroon). Bars for methods 1-3 indicate values which fall between adjacent labels on the x axis. For example, the bottom left histogram shows that methods 1, 2, and 3 each had 3 storms with α values between 10 and 20.

Coupling constant values range from roughly 17 - 68 for all methods with values

most frequently falling between 20 and 30. Higher α values amplify the impact of ε_{VS} on

T$_{1/2}$ in the model due to the term $\alpha\varepsilon_{VS}(t)$ in Equations (31), (32), and (38) for methods

one, two, and three respectively. Therefore, storms with higher temperature rises will

require higher alpha values in order to model them accurately. α values for method three

are slightly more closely spaced than those of methods one and two as evidenced by the slightly smaller standard deviation of 12.87 for method three vs. 13.90 for method one and 13.50 for method two.

The relaxation constant controls how quickly $T_{1/2}$ recovers to near pre-storm levels after ε_{VS} returns to normal. Storms with a faster recovery result in lower τ values. Relaxation constant values ranged from roughly 3 – 15 for all methods with values falling most frequently between 5 – 7.5. The range in τ values was significantly smaller than the range in α values indicating that the recovery period of geomagnetic storms is less variable than the main phase. The spread in τ values was similar for all methods, with standard deviations just over 3 hours.

It should be noted that the seemingly small difference in mean $T_{1/2}$ errors between method three (1.84%) and method one (2.04%) is significant due to its impact on density errors. Small changes (or errors) in thermospheric temperatures result in large changes (or errors) in thermospheric densities. A brief example from the J77 model illustrates this point. If the observed exospheric temperature is taken to be 700K, a 1.84% error in T_{∞} (matching the mean method three $T_{1/2}$ error) would generate a density error of 13.58% at an altitude of 500 km. If instead the 2.04% $T_{1/2}$ error from method one were applied, the resulting density error would increase to 15.14% at 500 km. In this case the 0.2% increase in temperature error produces a 1.56% increase in density error illustrating that the slight increase in temperature accuracy produced by method three is operationally relevant. Density results will be discussed in further detail later in the document.

Individual Storms

Figure 17 shows the $T_{1/2}$ results of the model for the CME storm from Julian Date (JD) 204-210, 2004. This storm period actually includes three distinct CMEs hitting the earth in rapid succession as evidenced by the magnetospheric electric field data shown in the bottom plot. The start of the storm period is defined as the time the first CME hits on JD 204, indicated by the vertical red line. The second and third CMEs can be seen in the abrupt rises in electric field magnitude on JD 206 and just prior to JD 209. For this storm, method three was significantly better than methods one or two, producing a relative
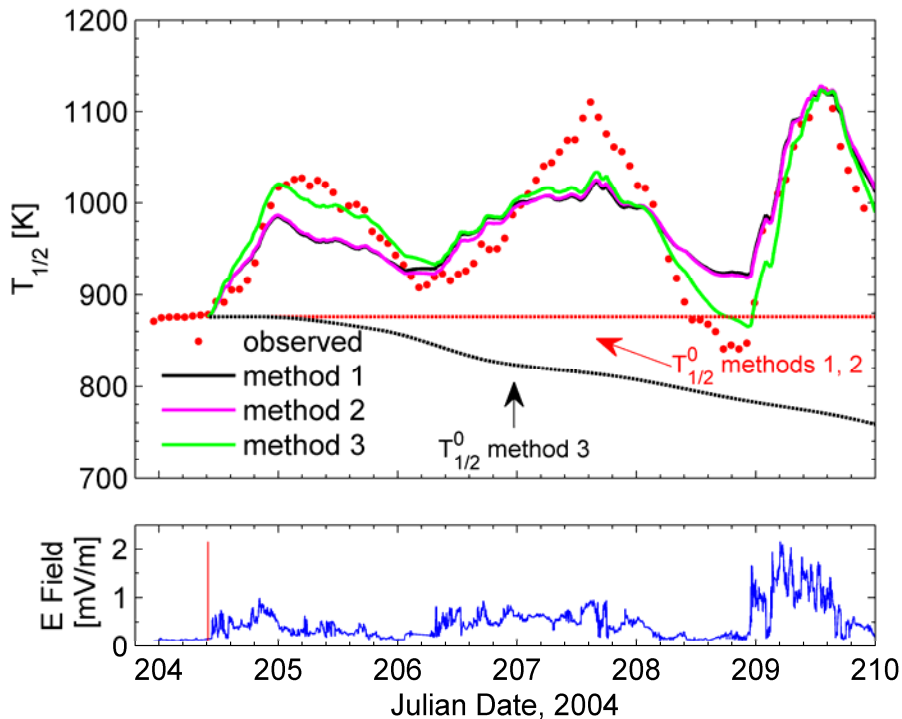
Figure 17: Model results for the CME storm from Julian Date 204-210, 2004. The top plot shows observed GRACE $T_{1/2}$ (red dots), along with model $T_{1/2}$ results for methods one (black), two (pink), and three (green). The dotted red line shows the pre-storm equilibrium temperature for methods one and two and the black dotted line shows the results of the approximation $T^0_{1/2} \approx T_{1/2UV}$ used for method 3. The bottom plot shows the electric field values calculated from ACE data as a function of time. The red vertical line indicates the storm starting time.

66

$T_{1/2}$ RMS error of 3.00% compared with 4.46% for method one and 4.28% for method two. Method three clearly outperformed the other two methods especially in fitting the $T_{1/2}$ peak from the first CME right around JD 205 and during the $T_{1/2}$ minimum just prior to the third CME at the end of JD 208.

The large differences between method three and methods one and two for this storm are due to the relatively large change in $T_{1/2UV}$ during the storm period from a pre-storm equilibrium value of 876.00 K down to 758.37 K by the end of the storm as shown by the dotted black line in Figure 17. Method one ignores this change entirely by treating $T_{1/2UV}$ as a constant value through the storm. Method two takes the change into account partially through the $\frac{dT_{1/2UV}}{dt}$ term in equation (32) but does not allow $T_{1/2}^0$ to vary with $T_{1/2UV}$ during the storm period. For this storm, while the overall $\Delta T_{1/2UV}$ is -117.63K over the storm period, the rate of change $\frac{dT_{1/2UV}}{dt}$ remains small, never dropping below -1.79 K/hr. By not allowing $T_{1/2}^0$ to vary with $T_{1/2UV}$ during the storm, methods one and two result in an awkward situation on JD 208, when observed GRACE $T_{1/2}$ values drop below the supposed UV contribution to $T_{1/2}$. This means that if methods one and two were to be accurate during this period, they would have to produce a negative value for $T_{1/2SW}$, the amount of temperature rise due to the solar wind, which is an unphysical result.

Method three avoids this situation by taking into account the change in $T_{1/2UV}$ during the storm period by approximating $T_{1/2}^0 \approx T_{1/2UV}$ which results in Equation (38). Allowing $T_{1/2UV}$ to decrease through the storm period by definition (Equation (26))

increases $T_{1/2SW}$. This results in a higher α value for method three for this storm, 35.32, than methods one and two, 31.45 and 30.72, respectively. Similarly, the decrease in $T_{1/2UV}$ during the storm period results in an increased τ value for method three, 10.03, compared with methods one and two, 7.16 and 7.82, respectively. The decreasing $T_{1/2UV}$ plays a role similar to the relaxation constant and helps the modeled $T_{1/2}$ recover after ε_{VS} decreases. Since the decreasing $T_{1/2UV}$ performs a similar role to the relaxation constant, method three results in a higher τ value.

Figure 18 shows the results of methods one, two and three for the CIR storm from JD 351-356, 2007. The overall $T_{1/2}$ increase for this storm over the pre-storm equilibrium value of 821K is about 60K. Similarly to the CME storm in Figure 17, this CIR has a decreasing $T_{1/2UV}$ throughout the storm period. Methods one and two produce virtually identical results, due to the fact that the $\frac{dT_{1/2UV}}{dt}$ for this storm is very small, never dropping below -0.32 K/hr. Method three accounts for the drop in $T_{1/2UV}$ of about 30K resulting in a relative RMS error of only 1.43% compared with 2.47% for methods one and two. The drop in $T_{1/2UV}$ also results in higher α and τ values compared with methods one and two for the same reasons as the CME storm.

Method three produced larger errors than method one or method two for 11 storms in the sample. Figure 19 shows the results for one of these storms, the CME-storm from JD 250-252, 2002. For this storm method 1 produced the lowest RMS error. Unlike the two previous storms, in this CME $T_{1/2UV}$ increases throughout the storm period. This causes τ for method three to be lower than methods one or two, resulting in the

68
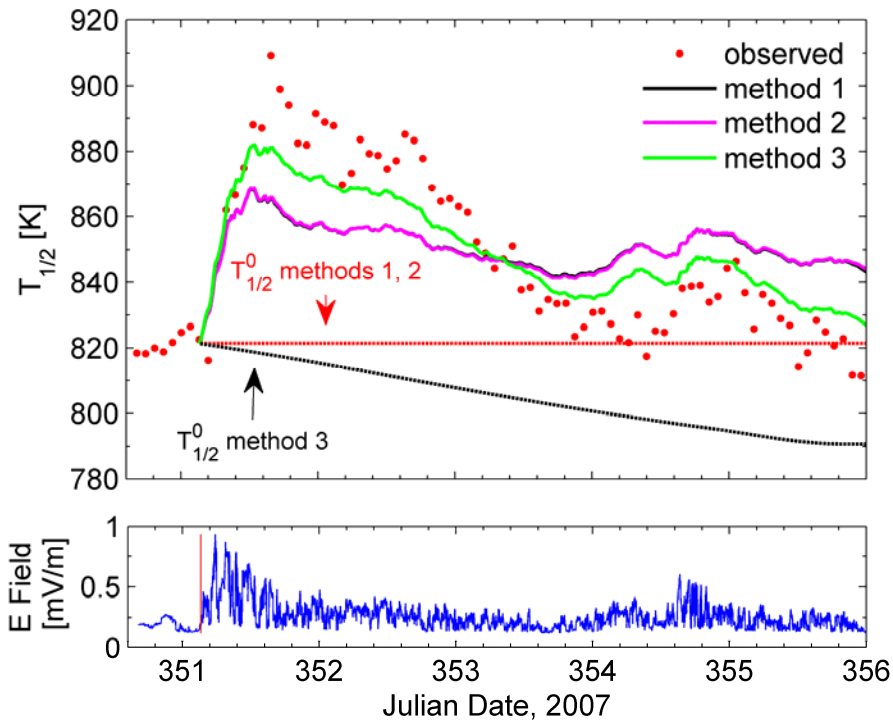
Figure 18: Model results for the CIR storm from JD 351-356, 2007. The top plot shows observed GRACE $T_{1/2}$ (red dots), along with model $T_{1/2}$ results for methods one (black), two (pink), and three (green). The dotted red line shows the pre-storm equilibrium $T_{1/2}$ for methods one and two and the black dotted line shows the results of the approximation $T_{1/2}^0 \approx T_{1/2UV}$ used for method 3. The bottom plot shows magnetospheric electric field values. The red vertical line indicates the storm start time.

decreased accuracy near the peak of the storm. In addition, method three models the

recovery phase of the storm worse than methods one or two because the increasing $T_{1/2UV}$

increases the method three model $\frac{dT_{1/2}}{dt}(t)$ in Equation (37) during a time when observed
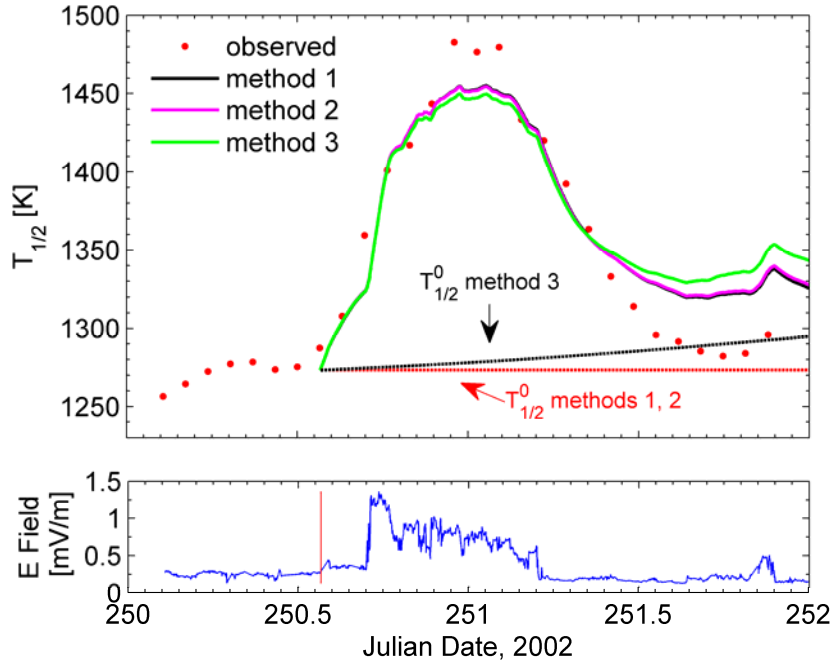
$T_{1/2}$ is decreasing .

69

Figure 19: Model results for the CME from JD 250-252, 2002. The top plot shows observed GRACE $T_{1/2}$ (red dots), along with model $T_{1/2}$ results for methods one (black), two (pink), and three (green). The dotted red line shows the pre-storm equilibrium $T_{1/2}$ for methods one and two and the black dotted line shows the results of the approximation $T_{1/2}^0 \approx T_{1/2UV}$ used for method three. The bottom plot shows magnetospheric electric field values. The red vertical line shows the storm start time.

Method Comparison

Overall, method three produced the lowest errors most frequently among the 38 storms tested. Table 3 shows that method three produced the lowest relative RMS error for 27 of the 38 storms studied (71%), while methods one and two only had the lowest error for 7 storms (18%) and 4 storms (11%), respectively. The method that produced the lowest error for a given storm was strongly dependent on the nature of the change (either increasing or decreasing) in $T_{1/2UV}$ over the storm period.

Figure 20 shows the model method that produced the lowest relative $T_{1/2}$ RMS error as a function of the change in $T_{1/2UV}$ ($\Delta T_{1/2UV}$) over the storm period. $\Delta T_{1/2UV}$ was

70
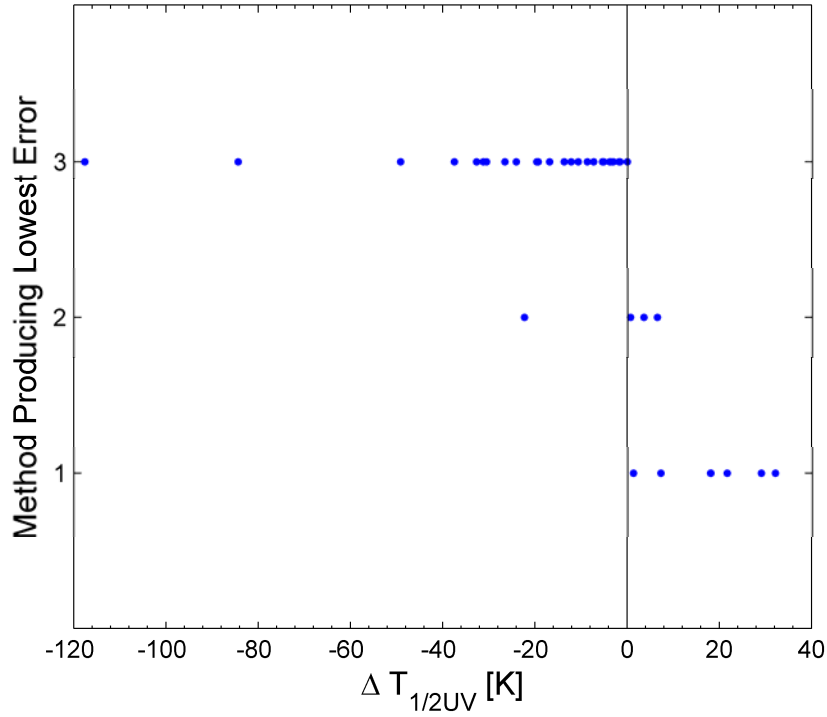
Figure 20: Model method producing the lowest relative $T_{1/2}$ RMS error as a function of the change in $T_{1/2UV}$ ($\Delta T_{1/2UV}$) over the storm period.

defined as the difference between the value of $T_{1/2UV}$ at the end of the storm period and the pre-storm equilibrium temperature. The majority of the storms (28 of 38) had a decrease in $T_{1/2UV}$ over the storm period. Method three produced the lowest error for 27 of those 28 storms. A negative $\Delta T_{1/2UV}$ allows method three to accurately characterize the recovery period of the storm with a larger τ value than methods one and two because some of the decrease in $T_{1/2}$ is accounted for by the decreasing $T_{1/2UV}$ at the end of the storm period. This larger τ value in turn means that the peak of the storm is more accurately modeled because a larger τ tends to increase $\frac{dT_{1/2}}{dt}(t)$, Equation (37), during the growth phase of the storm when $T_{1/2UV}$ is still near the pre-storm equilibrium level.

The single storm with a negative $\Delta T_{1/2UV}$ that was not modeled best by method three was the CIR storm from JD 94-98, 2004. For this storm $T_{1/2UV}$ rose above the pre-storm equilibrium temperature on JD 95-96 before dropping below on JD 97. Method two was the best method for this storm.

Method three did not produce the lowest error for any of the 10 storms with a positive $\Delta T_{1/2UV}$. Storms with higher values of $\Delta T_{1/2UV}$ tended to be modeled by method one best while all three of the storms with positive $\Delta T_{1/2UV}$ values for which method two produced the best results had $\Delta T_{1/2UV} < 6.5K$. Positive $\Delta T_{1/2UV}$ forced the τ value for method three to decrease, resulting in an underestimate of the peak $T_{1/2}$ values of the storm. In addition, the increase in $T_{1/2UV}$ caused method three to model the recovery phase of the storm worse than method one. Both of these problems are clearly illustrated in the JD 250, 2002 CME shown in Figure 19.

Comparison with Burke, 2011

Burke, 2011 determined α values for 37 of the 38 storms listed in Table 1. To compare Burke's 2011 results with current results, Burke's α values need to be divided by a storm-average value of the conversion factor D, from Equation (19), to account for the fact that he modeled T_∞ instead of $T_{1/2}$. The storm average value of D was generally near 0.95. After conversion, Burke's (2011) results have a mean α value of $36.07 \frac{K \cdot m}{hr \cdot mV}$ and a standard deviation of $17 \frac{K \cdot m}{hr \cdot mV}$. Burke (2011) treated $T_{\infty UV}$ as a constant in his model similarly to method one here. Burke's mean α and standard deviation of α are higher than those resulting from method one, shown in Table 3.

72

There are several reasons for the difference. First, Burke (2011) assumed τ was constant over all storms. The value of 6.84 hrs (after conversion) was determined from the single storm of JD 204-210, 2004 by Burke et al., 2009 using a different calibration of GRACE data. Allowing τ to change between storms impacts the value of α. In addition, Burke, 2011 used one-hour averaged ACE data to calculate ε_{VS} values and a time-step of 1 hr when applying Equation (31) rather than the 1 minute time step used here. Further, Burke 2011 used slightly different start and end times for the storm periods than used here, used the quadratic fit to the J77 model in Equations (6) and (7) to calculate observed T_∞, and used a different method to calculate the pre-storm equilibrium temperature; namely using the value of T_∞ at the start time of the storm rather than averaging over the 12 hours prior. Finally, Burke, 2011 used trial and error to determine the best value for α in an effort to align modeled T_∞ with the observed peak. In this thesis, the Nelder-Mead simplex direct search method was applied in order to rigorously determine the best α and τ values. Out of all these procedural differences, the method of determining α and τ values for each storm has the biggest impact on results.

To quantify the impact of using a rigorous method to determine optimum α and τ values the model was re-run for the storm of JD 204-210, 2004 using Equation (31) from method one and matching Burke's procedures as closely as possible. One-hour ACE data was used to calculate ε_{VS} and a one-hour time step was used in Equation (31). In addition T_∞ was modeled instead of $T_{1/2,}$ Burke's pre-storm equilibrium temperature was used

($T_\infty{}^0$ = 810K), and Burke's quadratic fit and orbit-averaging technique was used to determine observed GRACE T_∞.

Figure 21 shows a contour plot of relative T_∞ RMS errors as a function of α and τ values for the JD 204-210, 2004 storm. Contour plots were generated by running the model (method one here) for a 100x100 grid of α and τ values and computing the relative RMS error resulting from each α and τ pair. The α and τ values from Burke, 2011 (point A) result in a relative T_∞ RMS error of 3.82% compared with a relative T_∞ RMS error of 2.58% resulting from optimal α and τ values (point C) determined by using the
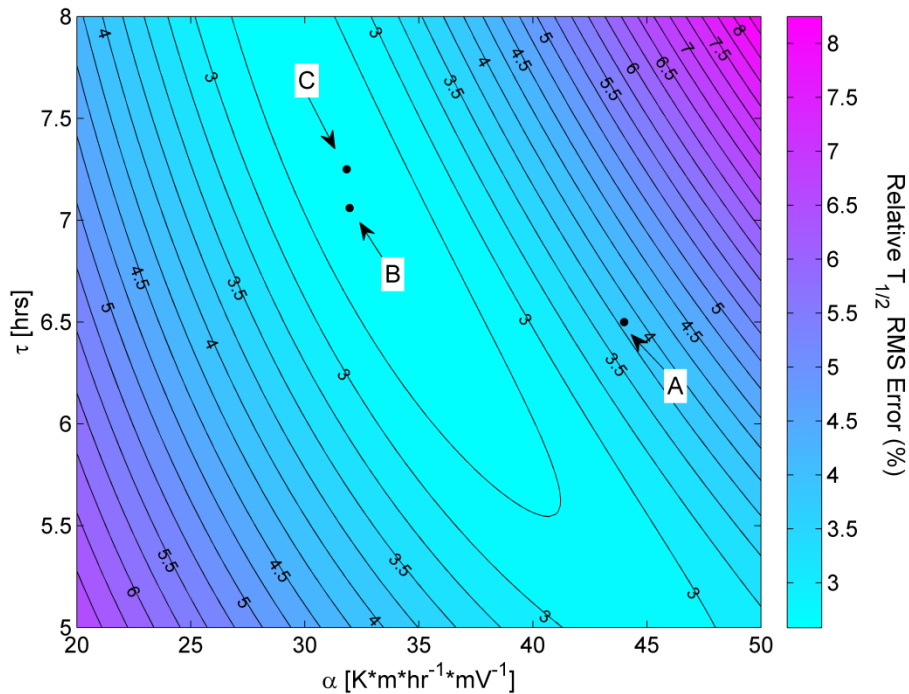
Figure 21: Contour plot of relative RMS errors (%) in T_∞ resulting from different α and τ values using the procedures from Burke, 2011 for the CME storm from JD 204-210, 2004. Point A shows the α and τ values reported by Burke, 2011. Point B shows the α and τ values that result from using the Nelder-Mead simplex direct search method to minimize the error between the peak observed GRACE T_∞ and the modeled value. Point C shows the α and τ values resulting from using the Nelder-Mead simplex direct search method to minimize the relative RMS error in T_∞ over the entire storm period.

74

Nelder-Mead simplex direct search method to minimize the relative RMS error. Point B

shows the α and τ values resulting from the Nelder-Mead method applied to minimize

the error between the peak observed GRACE T_∞ and the modeled value. This is the error

Burke (2011) was trying to minimize via trial and error.

The contour plot shows that the relative RMS error is a relatively shallow

function of τ within the range of 5 – 8 hrs and α within the range of 30 to 45 $\frac{K \cdot m}{hr \cdot mV}$.

Because of this the difference between Burke's α and τ values (44.00 $\frac{K \cdot m}{hr \cdot mV}$,6.50 hrs) and

the optimal values (31.83$\frac{K \cdot m}{hr \cdot mV}$,7.25 hrs) only decreases relative RMS error from 3.82%

to 2.58%. This shows that while Burke's trial and error method came close to the optimal

values, the more rigorous approach produces superior results and helps explain the

difference between the method one α values and Burke's results. The fact that relative

RMS error is a relatively shallow function of α and τ near the minimum also suggests

that it is possible to produce acceptable results with α and τ values different than the

optimal values.

Solar Cycle Dependence of α and τ

Burke, 2011 suggested that the values for α might vary throughout the solar cycle

as a function of $F_{10.7a}$. Since the relative RMS error is a shallow function of α and τ near

the minimum, it is reasonable to expect that the model will produce low errors with

values of α and τ that are different than the optimal values for each storm. In order to test

this, best-fit curves were constructed to produce α and τ as functions of the $F_{10.7a}$ value,

the 162-day running average of the $F_{10.7}$ index used in the J77 model, at the start of each

storm period shown in Table 2. Since F10.7a is a 162-day average, it changes very little

over the 1- 6 day storm periods used in this Thesis. Least-Squares fits were constructed

using data from method three because it proved to produce the lowest errors of the three

methods for most of the storms in the sample.

Figure 22 shows method three α values as a function of $F_{10.7a}$ for all storms. A

linear fit, shown in black, produces a tenuous correlation of R = 0.21. Robinson and

Vondrak, 1984 showed that both the ion-electron production rate, which impacts particle

precipitation, and ionospheric conductance, which impacts joule heating, depend on

$\sqrt{F_{10.7}}$ (Burke, 2011). Since α accounts for the energy transfer from the magnetosphere

to the thermosphere via joule heating and particle precipitation in the driven-dissipative

model, it is reasonable to fit α as a quadratic function of $\sqrt{F_{10.7a}}$ (Burke, 2011). The

quadratic fit of α to $\sqrt{F_{10.7a}}$, shown in red, produces a correlation of R = 0.40 which is

much improved over the linear fit. Figure 23 shows τ as a function of $F_{10.7a}$ for all storms

using method three. Again, a quadratic least-squares fit was constructed of τ as a function

of $\sqrt{F_{10.7a}}$. The correlation of R = 0.53 is higher than the correlation for α.
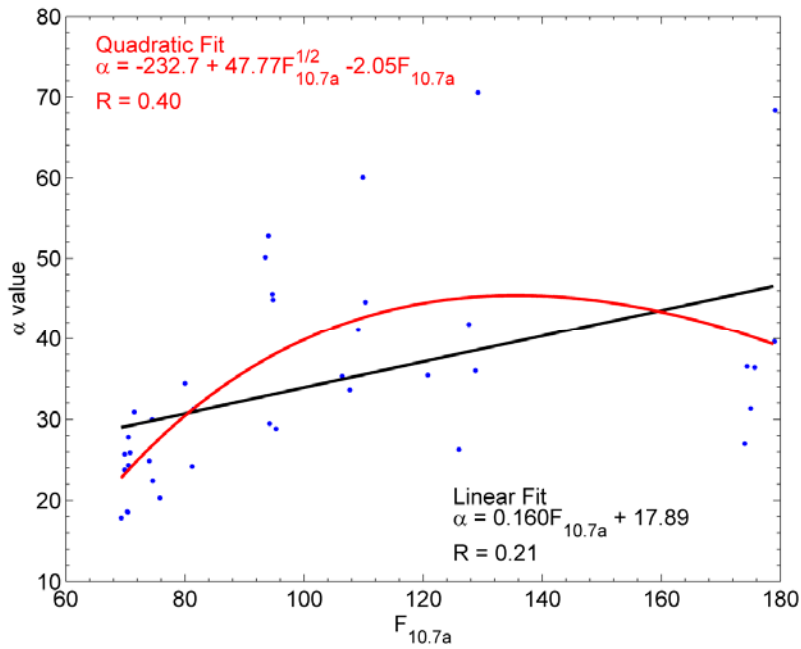
Figure 22: Coupling constant (α) as a function of $F_{10.7a}$ shown with blue dots. The black line and text show the best linear fit to the data. The red line and text show the best fit of α as a quadratic function of $\sqrt{F_{10.7a}}$.

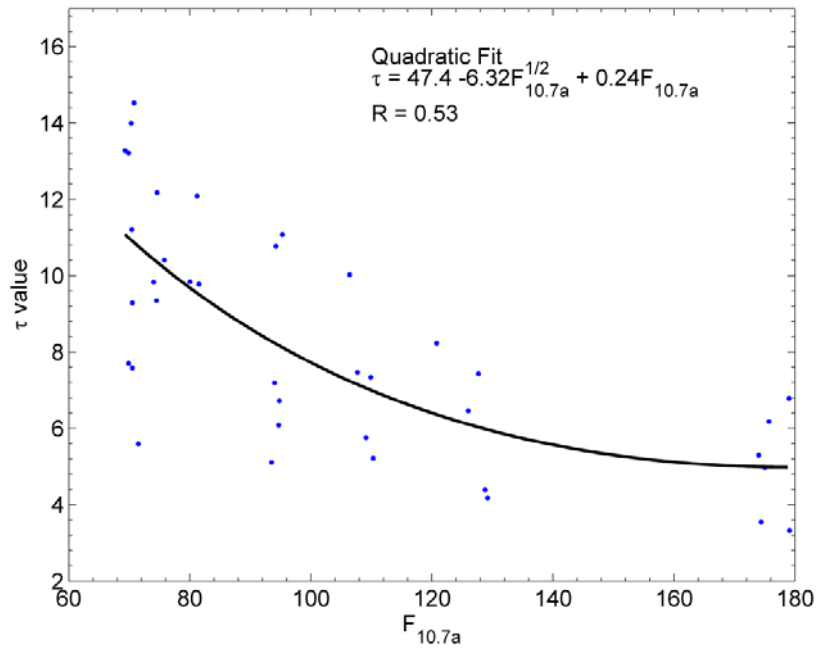**Figure 23: Relaxation constant (τ) as a function of $F_{10.7a}$ shown with blue dots. The black line shows the best fit of τ as a quadratic function of $\sqrt{F_{10.7a}}$.**

77

Outliers

Figure 22 highlights the fact that three storms have significantly higher values of α than the others. The JD 250, 2002 CME has an α value of 68.38, the JD 324, 2003 CME has an α value of 70.56 and the JD 312, 2004 CME has an α value of 60.05. All other storms have $\alpha < 53$. The high α values for the 2003 and 2004 storms are due to the fact that they were by far the strongest storm in the sample. For the 2003 storm, the minimum Dst value was an extreme -422 nT and it had $T_{1/2}$ rise of 536 K over the pre-storm equilibrium value. The 2004 storm had a minimum Dst value of -389 nT and a $T_{1/2}$ rise of 538K. These $T_{1/2}$ rises are 270K larger than the next highest rise in the sample. The high α values for the JD 324, 2003 CME and the JD 314, 2004 CME are a result of the large storm-time rise in $T_{1/2}$.

In contrast, the JD 250, 2002 storm has a minimum Dst of -181 nT and a storm-time rise in $T_{1/2}$ of 210K. While this is a large rise in $T_{1/2}$, there were 11 storms in the sample which had a larger $T_{1/2}$ rise yet a smaller α. The JD 250, 2002 CME had such a high α value because its storm time $T_{1/2}$ rise resulted from a relatively weak ε_{VS} signature with a maximum of 1.37 mV/m shown in Figure 19. For comparison, the JD 204, 2004 storm shown in Figure 17 had a $T_{1/2}$ rise 18% higher than JD 250, 2002 yet the maximum ε_{VS} value was 58% higher. The JD 250, 2002 storm had a temperature rise that was disproportionately larger than the solar wind energy contribution, modeled with the $\alpha\varepsilon_{VS}$ term, would indicate. For this storm, the extra energy came from a spike in solar EUV energy shown in Figure 24.

78

Figure 24 plots five-minute average EUV (26-34 nm) flux (black line), as measured by the Solar and Heliospheric Observatory (SOHO) satellite, as a function of JD, 2002 for the time period of the JD 250, 2002 CME. Daily $F_{10.7}$ (solid red line and x's) and $F_{10.7a}$ (dotted red line with x's) values are also shown. The blue vertical line indicates the storm start time. A large spike in EUV flux, due to a solar flare, is clearly seen just after the storm start time. Since the model accounts for EUV energy with the daily $F_{10.7}$ index, it does not capture variations on such short time scales as the flare seen during this storm. As a result, the model has to account for this EUV flare energy by attributing it to the solar wind contribution, $\alpha\varepsilon_{VS}$. Since ε_{VS} is small for this storm, the only way to increase the solar wind contribution is by increasing the α value.
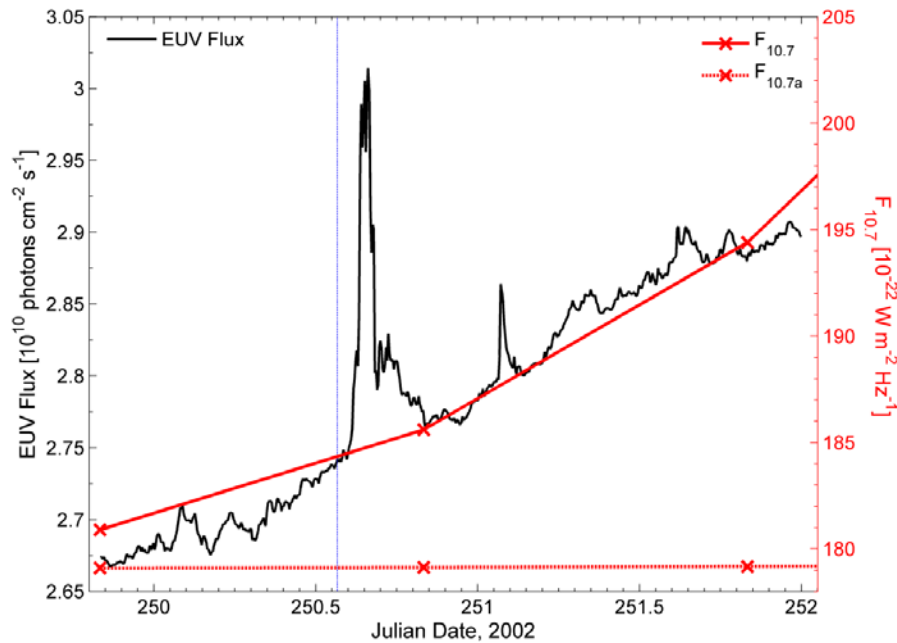

Figure 24: Five-minute average Solar EUV flux (26-34 nm) measured by the SOHO satellite (black) shown as a function of JD, 2002. Daily F10.7 (solid red line and x's) and F10.7a values (dotted red line and x's) are also shown. The blue line indicates the start time of the JD 250, 2002 CME storm.

Impact of Storm Type

Since CME-driven storms have features distinctly different than CIR-driven storms, their response to solar cycle changes may not be equivalent. To test this, least-squares fits of α and τ to $\sqrt{F_{10.7a}}$ were constructed for each storm type separately. Of the 38 storms in the sample, 25 were CIR storms and 13 were CME storms. Table 1 lists the storm type of each storm. Figure 25 shows α as a quadratic function of $\sqrt{F_{10.7a}}$ for CME storms (blue) and CIR storms (red). The value of α for CME storms exhibits a very low correlation, R = 0.12, and is nearly a straight line. CME storms generally had higher α values than CIR storms. In fact all storms with $\alpha > 50$ are CMEs while all of the storms with $\alpha < 25$ are CIR storms. CIR storms are fit much better as a function of $\sqrt{F_{10.7a}}$ with a correlation of R = 0.60, much improved from the all-storms fit. The CIR storms are fit better because both CIR occurrence and $F_{10.7}$ index both exhibit a 27-day period linked to solar rotations. Since CME occurrence is irregular with no characteristic spacing, CMEs are not as well correlated with $F_{10.7}$ measurements (Borovsky and Denton, 2006).

Figure 26 shows τ as a quadratic function of $\sqrt{F_{10.7a}}$ for CME storms (blue) and CIR storms (red). Both best fit curves are similar, with correlations of R=0.47 and R=0.51 for CIRs and CMEs, respectively. The correlations are worse for both storm types than the correlation of the all storms fit indicating that τ is not strongly dependent on storm type. In general, τ values are higher for CIR storms. All storms with $\tau > 11$ are CIR-driven.
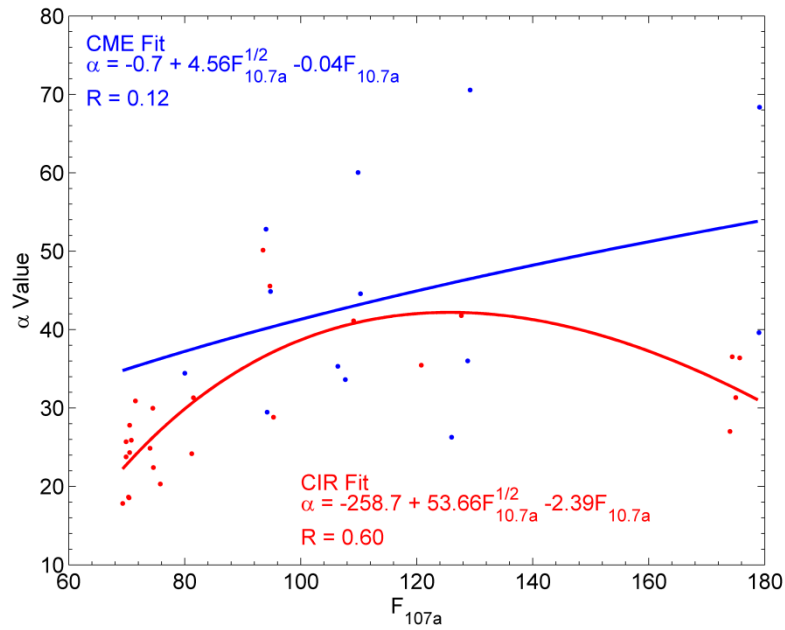
Figure 25: Coupling constant (α) as a function of $F_{10.7a}$. Best fits of α as a quadratic function of $\sqrt{F_{10.7a}}$ are shown. CME storms are shown in blue, CIR storms in red.
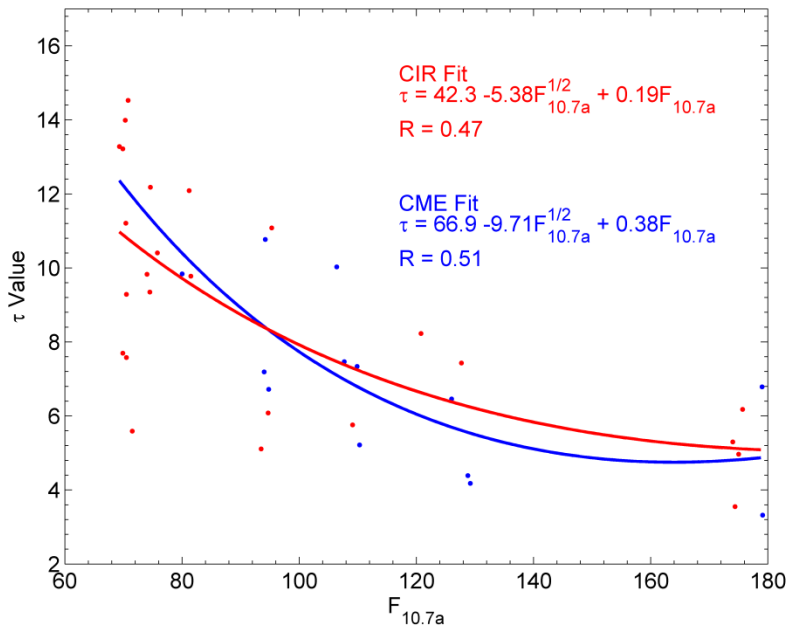
Figure 26: Relaxation constant (τ) as a function of $F_{10.7a}$. Best fits of τ as a quadratic function of $\sqrt{F_{10.7a}}$ are shown. CME storms are shown in blue, CIR storms in red.

81

Best Fit α and τ Results

All 38 storms were run with all storm fit α and τ values determined with the

quadratic equations shown in Figure 22 and Figure 23 using method three procedures. In

addition, CME storms were run using the CME fit α and τ values and CIR storms were

run using CIR fit α and τ values determined using functions shown in Figure 25 and

Figure 26. Table 4 shows the mean $T_{1/2}$ relative RMS errors, calculated using Equation

(39), that result from method three using optimal α and τ values for each storm listed in

Table 2, along with relative RMS errors that result from the all storms fit, CME fit, and

CIR fit α and τ values. Column 2, labeled All Storms Mean, shows that the mean $T_{1/2}$

RMS error increased from 1.84% to 3.15% for all 38 storms when using the all storms fit

α and τ values. For CME and CIR storms, errors increased from the optimal values when

both the all storms fit and the storm specific fit was applied. For both storm types, the

storm type specific fit values of α and τ produced a lower average RMS error than the all

storms fit. Applying best-fit curves to determine α and τ for each storm also created more

spread in the relative $T_{1/2}$ RMS error values.

Table 4: Relative $T_{1/2}$ RMS Error Results using Best Fit α and τ values with Method Three

	All Storms		CME Storms		CIR Storms	
	Mean	Std Dev	Mean	Std Dev	Mean	Std Dev
Optimal α and τ	1.84%	0.80%	2.17%	0.83%	1.67%	0.75%
All Storms Fit α and τ	3.15%	1.68%	4.37%	2.00%	2.52%	1.06%
CME-Fit α and τ			4.01%	1.77%		
CIR-Fit α and τ					2.24%	1.01%

Table 4 shows standard deviations of the relative RMS error for each of the different fits. In all cases, the standard deviation increased over the value for the optimal α and τ case. Figure 27 shows histograms of the relative $T_{1/2}$ RMS error for all storms (top), CME storms (bottom left) and CIR storms (bottom right). In the all storm histogram we see the all storm fit error values are spread over a much larger range than
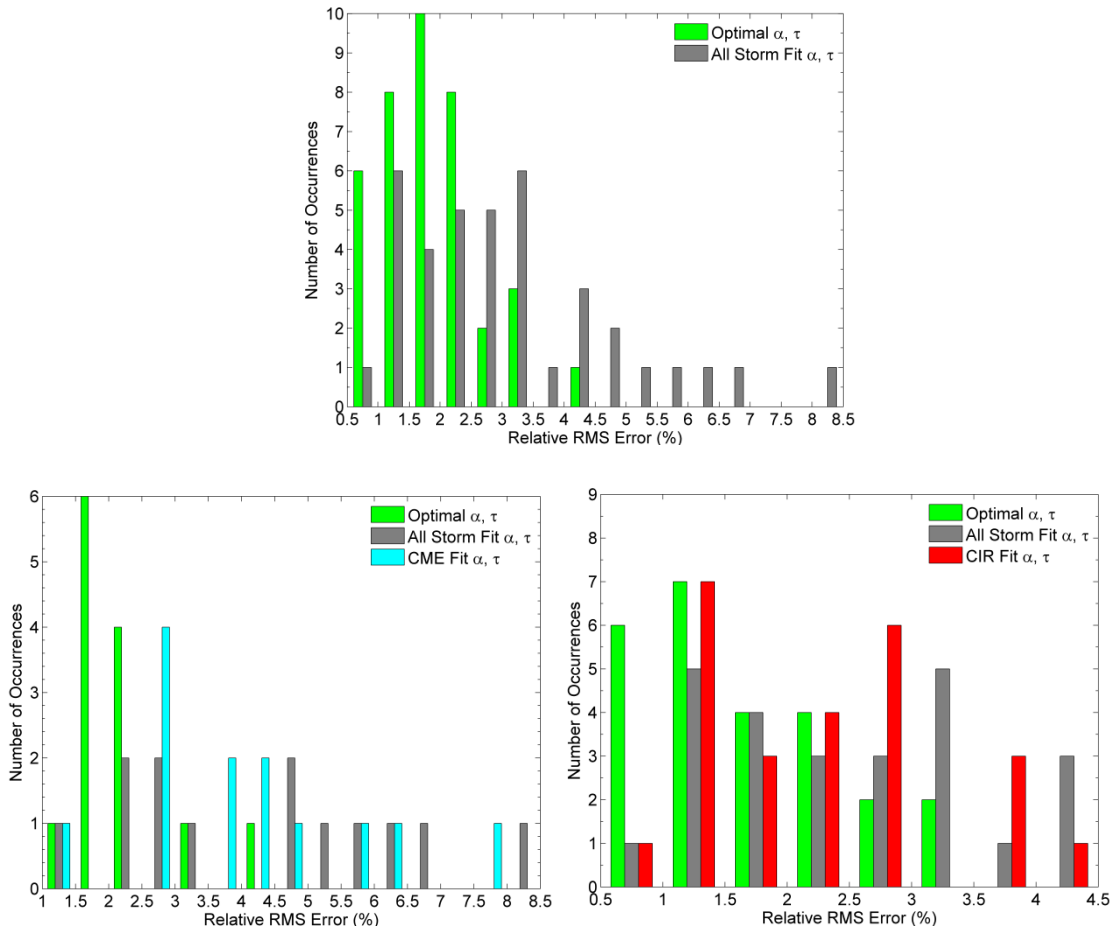
Figure 27: Histograms showing relative $T_{1/2}$ RMS errors from method three using best-fit α and τ values for all storms (top), CME storms (bottom left), and CIR storms (bottom right). Errors for optimal α and τ values are shown in green, errors for all storm fit α and τ values are shown in gray, errors for CME-fit α and τ values are shown in blue, and errors for CIR-fit α and τ values are shown in red. Bars show the number of storms which resulted in a relative $T_{1/2}$ RMS error between the adjacent values of the x-axis.

83

the optimal error values. The maximum error using optimal α and τ values lies between

4 – 4.5% while the maximum error using all storm fit α and τ values lies between

8 - 8.5%. Similar patterns are seen for CME storms and CIR storms. The spread is most

significant for CME storms, where the standard deviation more than doubles from 0.83%

for the optimal case to 2.00% for the all storm fit case.

Individual Storms

Table 5 shows the results of the all storms fit and the CME fit α and τ values

applied to the CME storm of JD 204-210, 2004. The optimal α and τ for this storm are

included for comparison. In this case, the CME fit produced a higher error than the all-

storms fit. This is not surprising as the correlation for the CME-fit function for α was

very low (R = 0.12). α and τ values resulting from the all storms fit and the CME fit are

very similar for this storm, resulting in the similar model $T_{1/2}$ curves for these two cases

seen in Figure 28 as the solid pink (all storms fit) and black (CME fit) lines. Both the

best fit α and τ values produce model $T_{1/2}$ curves that are below the optimal one (shown

in green) resulting in decreased accuracy especially during the second and third $T_{1/2}$

peaks on JD 207 and JD 209. The best fit α values are higher than the optimal value,

suggesting that model $T_{1/2}$ increase more rapidly when ε_{VS} increases, however the best fit

τ values are lower than the optimal case which indicates a quicker recovery time and

decreases the modeled increase in $T_{1/2.}$ For this storm, the decrease in τ wins out and

causes the model $T_{1/2}$ for the all storm and CME fit cases to lag below the optimal case

during the peaks on JD 205 and 207.

Table 5: Results for JD 204-210, 2004 CME

	α	τ	Relative $T_{1/2}$ RMS Error
Optimal	35.32	10.03	3.00%
All Storms Fit	41.93	7.74	3.30%
CME Fit	42.08	7.17	3.76%
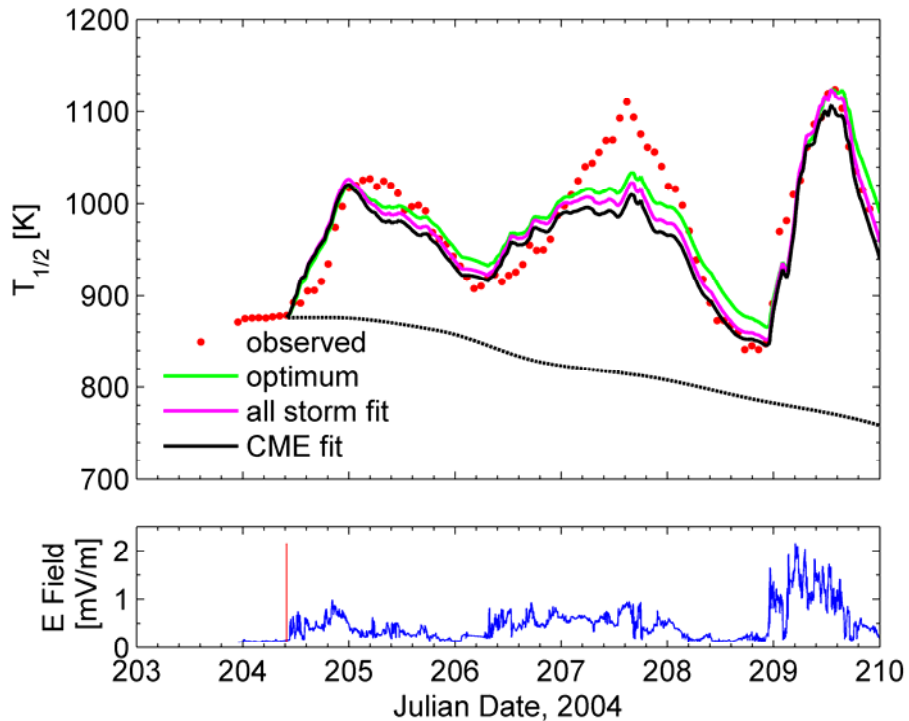
Figure 28: Model results for the CME storm from Julian Date 204-210, 2004. The top plot shows observed GRACE $T_{1/2}$ (red dots), along with method three model $T_{1/2}$ using optimal α and τ values (green), all storms fit α and τ values (pink), and CME fit α and τ values (black). The the black dotted line shows $T_{1/2UV}$. The bottom plot shows the electric field values calculated from ACE data as a function of time. The red vertical line indicates the storm starting time.

A contour plot of relative $T_{1/2}$ RMS errors (%) as a function of α and τ is shown in Figure 29 for the JD 204-210, 2004 CME storm. As expected, relative RMS error is a relatively shallow function of α and τ around the minimum, shown as point A

85

corresponding to the optimal α and τ values for this storm. Points B and C correspond to

α and τ values calculated using the all storms fit and the CME fit, respectively. Even

though these values are not very close to the minimum, the relative RMS error for both is

still less than four percent.
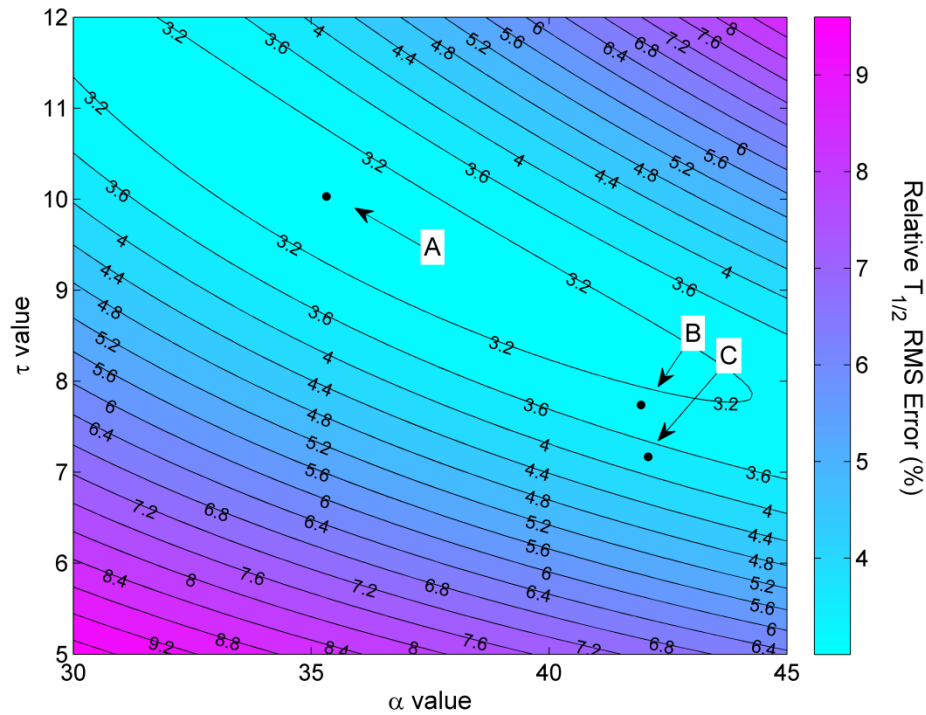
Figure 29: Contour plot of relative $T_{1/2}$ RMS errors (%) as a function of α and τ for the JD 204-210, 2004 CME storm using method three. Point A shows the optimal α and τ values, point B shows the all storms fit α and τ values, and point C shows the CME fit α and τ values.

Table 6 shows the results of the all storms fit and the CIR fit α and τ values

applied to the CIR storm of JD 351-356, 2007. The optimal values of α and τ are

included for comparison. For this storm the CIR-fit produced a lower relative RMS error

than the all-storms fit. Best fit α values for this storm are very close to the optimal value

while best fit τ values are $3 - 3.5$ hrs higher than the optimal value. The increased τ value

indicates that the best fit models should result in higher $T_{1/2}$ values, especially after ϵ_{VS}

decreases, because higher τ values equate to a longer e-fold recovery time.

Table 6: Results for JD 351-356, 2007 CIR

	α	τ	Relative $T_{1/2}$ RMS Error
Optimal	24.32	7.58	1.43%
All Storms Fit	23.84	11.26	2.76%
CIR Fit	23.32	10.53	2.24%

Figure 30 shows the model results for the JD 351-356, 2007 CIR storm and as

expected, both the all storm fit and the CIR fit α and τ values have $T_{1/2}$ curves that are

higher than the optimal case resulting in the increased errors shown in Table 6. As with

the JD 204, 2004 CME, here the all storm fit and the storm specific fit α and τ values are

similar leading to the small difference between the all storm and CIR fit $T_{1/2}$ curves.

A contour plot of relative $T_{1/2}$ RMS error (%) as a function of α and τ is shown

for the JD 351-356, 2007 CIR in Figure 31. Point A shows the location of the minimum

error resulting from optimum α and τ values while points B and C show the locations of

the all storm fit and CIR fit α and τ values, respectively. Again, the error is a relatively

shallow function of α and τ around the minimum. Any α, τ pair within the ranges of $20 <$

$\alpha < 28$ and $5 < \tau < 10$ results in a relative RMS error of less than 3% for this storm.
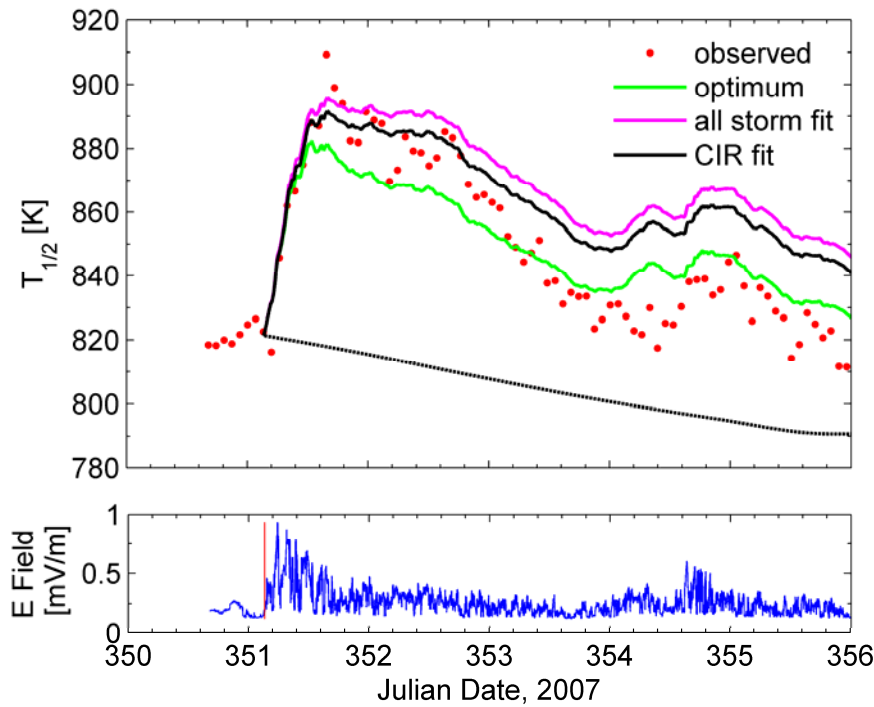
Figure 30: Model results for the CIR storm from Julian Date 351-356, 2007. The top plot shows observed GRACE $T_{1/2}$ (red dots), along with method three model $T_{1/2}$ using optimal α and τ values (green), all storms fit α and τ values (pink), and CIR fit α and τ values (black). The black dotted line shows $T_{1/2UV}$. The bottom plot shows the electric field values calculated from ACE data as a function of time. The red vertical line indicates the storm starting time.

General Applicability

The results of the model using best fit α and τ values indicate that relatively low errors can be obtained using model parameters determined without prior knowledge of storm-time $T_{1/2}$ values. To test this conjecture the model with best-fit α and τ values was applied to two storms, one CME and one CIR, outside the original sample of 38 storms that were used to determine the best fit α and τ curves. Due to the constraints of GRACE data availability, both test storms were within the same time frame of the original storms
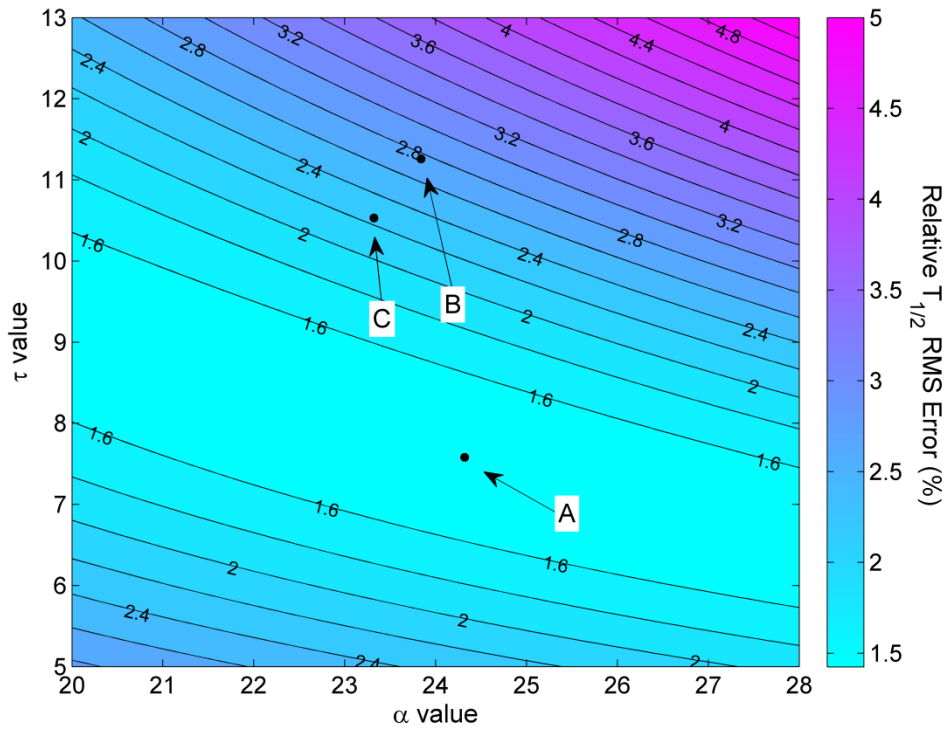
Figure 31: Contour plot of relative $T_{1/2}$ RMS errors (%) as a function of α and τ for the JD 351-356, 2007 CIR storm using method three. Point A shows the optimal α and τ values, point B shows the all storms fit α and τ values, and point C shows the CME fit α and τ values.

(2002-2008). Test storms were selected based on the availability of ACE data needed to calculate storm time ε_{VS} values. Table 7 shows from left to right the year, start time, end time, minimum Dst index during the storm period, $F_{10.7a}$ value on day one of the storm, the pre-storm equilibrium temperature ($T_{1/2}{}^{0}$), $\Delta T_{1/2UV}$ for each storm period, and the storm type for each of the test storms.

Table 7: Test Storm Data

Year	Storm Start				Storm End				Min Dst	$F_{10.7a}$	$T_{1/2}{}^{0}$	$\Delta\ T_{1/2UV}$	Storm Type
	Day	Hour	Min	Sec	Day	Hour	Min	Sec					
2003	308	3	36	0	309	6	0	0	-69	132.06	1049.4	-24.39	CME
2004	42	4	48	0	45	0	0	0	-109	123.46	928.5	-20.16	CIR

Table 8 shows the results for the JD 308-309, 2003 CME. Although the relative $T_{1/2}$ RMS error for both the all storms fit and CME-fit α and τ values are more than double the optimal error, they are also less than the average error for CME storms in the original sample. This indicates that the best fit α and τ values are reasonable even outside the original sample.

Table 8: Results for JD 308-309, 2003 CME

	α	τ	Relative $T_{1/2}$ RMS Error
Optimal	39.01	4.46	0.98%
All Storms Fit	45.54	6.47	2.89%
CME Fit	46.42	5.50	2.17%

Figure 32 shows the $T_{1/2}$ curves resulting from the optimal, all storms fit, and CME fit α and τ values. Both fits cause the model to overestimate the peak $T_{1/2}$ value and do not recover as fast as the observed $T_{1/2}$. The CME fit has slightly lower errors than the all storms fit due to its lower τ value, which causes $T_{1/2}$ to drop faster during the recovery period and close the gap between the modeled and observed $T_{1/2}$.

Figure 33 shows a contour plot of the relative $T_{1/2}$ RMS error as a function of α and τ for the JD 308, 2003 storm. The errors for this storm are more sensitive to changes in τ compared to the storms shown previously. However, within the range of $3 < \tau < 6$, α can take any value between 35 and 48 and still produce an error of less than 3%.

Figure 32: Model results for the CME storm from Julian Date 308-309, 2003. The top plot shows observed GRACE $T_{1/2}$ (red dots), along with method three model $T_{1/2}$ using optimal α and τ values (green), all storms fit α and τ values (pink), and CME fit α and τ values (black). The black dotted line shows $T_{1/2UV}$. The bottom plot shows the electric field values as a function of time. The red vertical line shows storm start time.
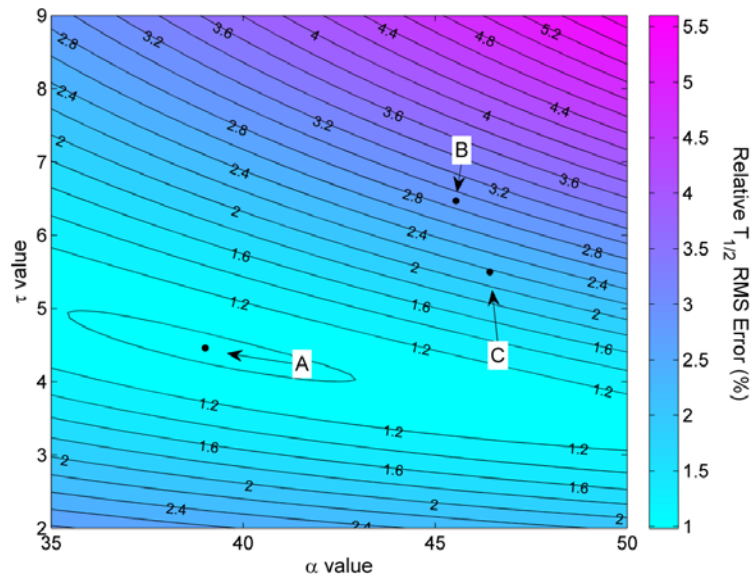
Figure 33: Contour plot of relative $T_{1/2}$ RMS errors (%) as a function of α and τ for the JD 308-309, 2003 CME storm using method three. Point A shows the optimal α and τ values, point B shows the all storms fit α and τ values, and point C shows the CME fit α and τ values.

91

Results from the CIR test storm are shown in Table 9. Again, the relative $T_{1/2}$

RMS error for both the all storms fit and the CIR fit α and τ values are less than or equal

to the average errors for CIR storms in the original sample. The CIR storm fit produces

lower errors than the all storms fit for this storm. The $T_{1/2}$ curves produced by each model

run are shown in Figure 34. The CIR fit model actually matches the peak $T_{1/2}$ value just

Table 9: Results for JD 42-45, 2004 CIR

	α	τ	Relative $T_{1/2}$ RMS Error
Optimal	28.74	8.56	1.05%
All Storms Fit	44.99	6.81	2.52%
CIR Fit	42.46	5.98	1.43%

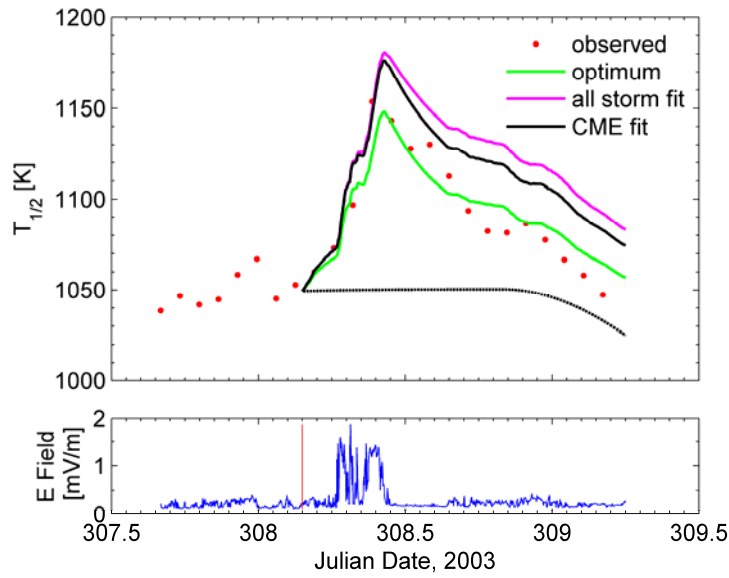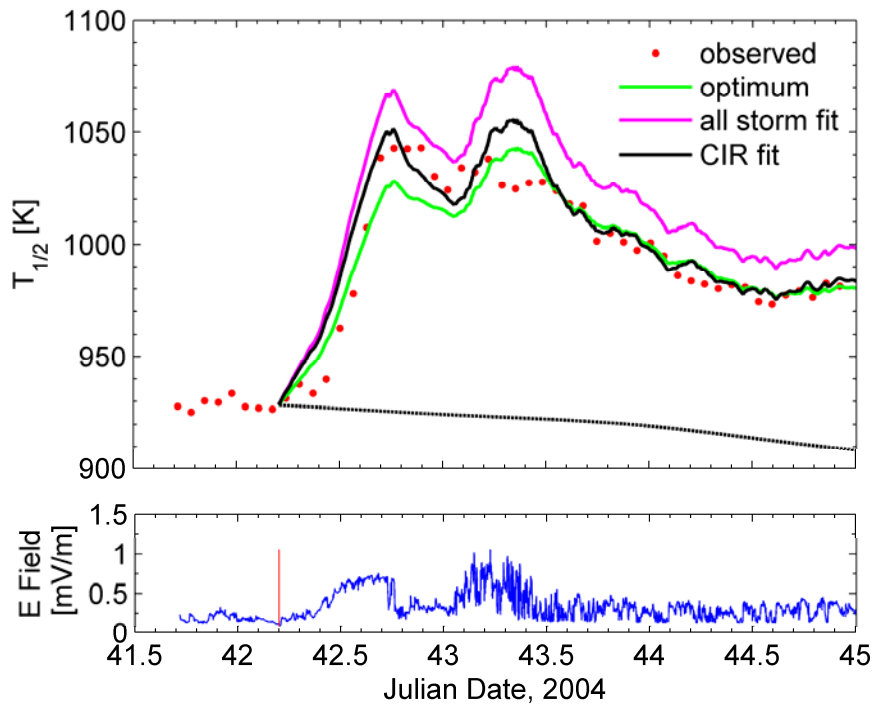**Figure 34: Model results for the CIR from JD 42-45, 2004. The top plot shows observed $T_{1/2}$ (red dots), along with method three model $T_{1/2}$ using optimal α and τ values (green), all storms fit α and τ values (pink), and CIR fit α and τ values (black). The black dotted line shows $T_{1/2UV}$. The bottom plot shows the electric field values calculated from ACE data. The red vertical line indicates the storm start time.**

after JD 42.5 more accurately than the optimal case. The increase in error is due to the modeled $T_{1/2}$ over-reacting to the second ε_{VS} peak on JD 43 resulting in over-estimates of $T_{1/2}$. The higher α and τ values of the all storms fit cause the all-storm fit model to produce higher $T_{1/2}$ at all times compared with the CIR fit. A notable feature of this storm is the fact that the best fit α and τ values are significantly different than the optimal values yet the relative RMS errors do not increase drastically. Figure 35 shows the relative $T_{1/2}$ RMS error as a function of α and τ. There is a very broad range of α and τ values which result in errors of less than 3% for this storm and both best fit models fall within the range.
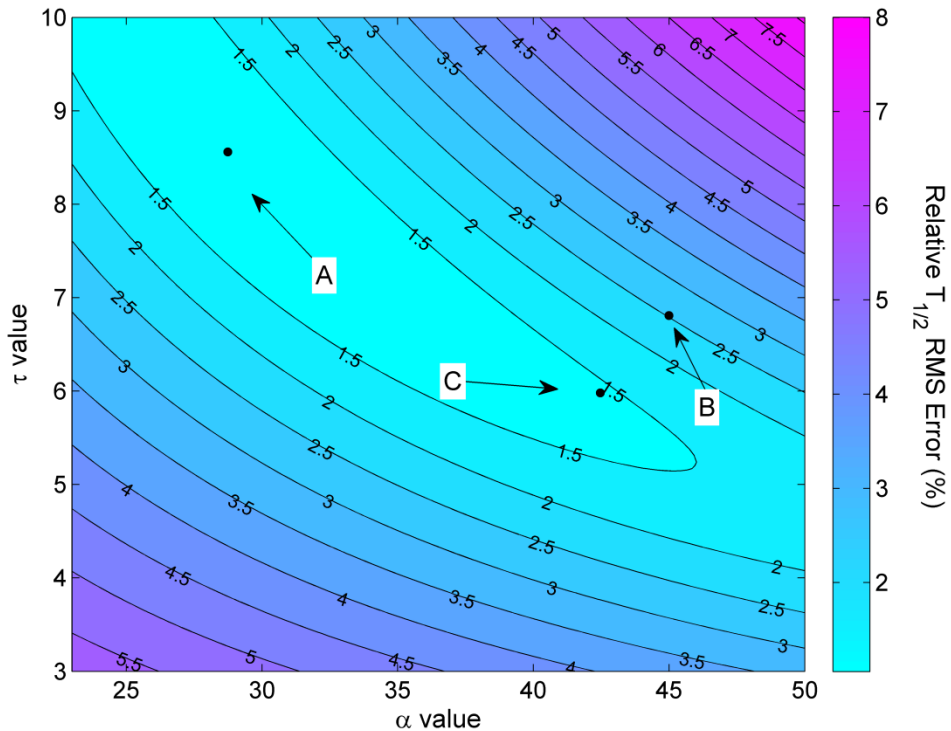
Figure 35: Contour plot of relative $T_{1/2}$ RMS errors (%) as a function of α and τ for the JD 42-45, 2004 CIR storm using method three. Point A shows the optimal α and τ values, point B shows the all storms fit α and τ values, and point C shows the CIR fit α and τ values.

Density Errors

      In order to compare the results of the driven-dissipative model to published

HASDM density errors, model $T_{1/2}$ values are used to calculate model densities. Using

the methods described in section III, model orbit-averaged densities were computed for

each storm in the 38-storm sample and relative density RMS errors for each storm were

calculated. In general, higher temperature errors should result in higher density errors.

Figure 36 shows the relative RMS error in model orbit-average density plotted as a

function of relative RMS error in model orbit-average $T_{1/2}$. In general, the errors follow

the expected trend with high $T_{1/2}$ errors resulting in high density errors. However, there

are three outlier storms with density errors greater than 13% resulting from $T_{1/2}$ errors of

less than 1.5%.
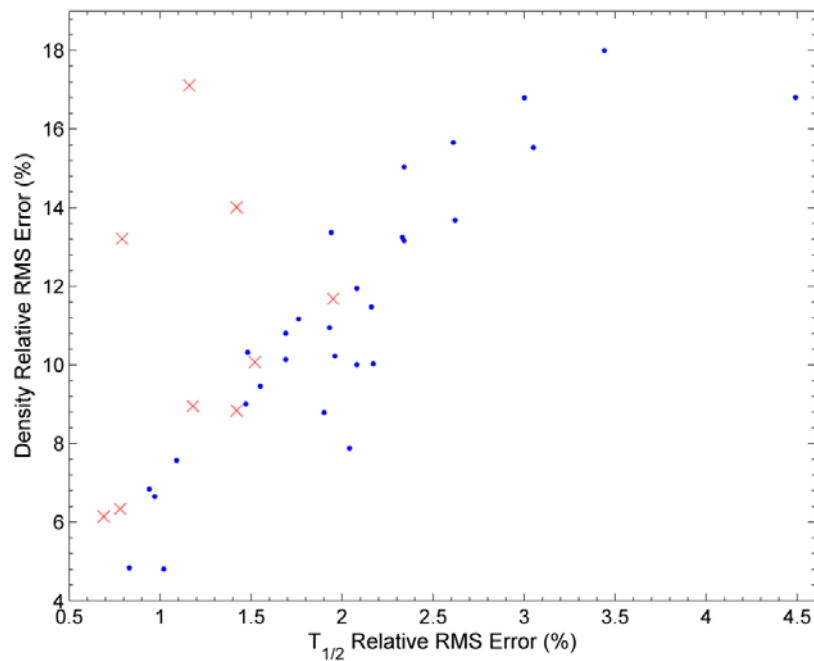
Figure 36: Model relative orbit-average density RMS error plotted as a function of relative orbit-average $T_{1/2}$ RMS errors. Blue dots show storms from 2002 – JD 290, 2007. Red x's show storms from JD 290, 2007 – 2008.

94

The outlier storms are caused in part by differences in the orbit-average

techniques used when computing observed GRACE orbit-averaged $T_{1/2}$ and model orbit-

averaged density. Figure 37 illustrates the two different techniques as applied to

exospheric temperature. Observed GRACE orbit-averaged $T_{1/2}$ was calculated via the

bin-averaging technique where the J77 model is applied to calculate a temperature in

each latitude bin prior to orbit-averaging. Producing observed orbit-averaged temperature

values via the bin- averaging technique is mathematically preferable to the whole-orbit

technique because the latter technique is akin to calculating an average of averages.

These techniques are not equivalent and produce slightly different results. The average

relative RMS difference between the orbit-averaged T_∞ produced by the two techniques

was small for most storms, ranging between 0.20% and 3.07% with an average of

1.33%. Figure 38 shows the results of the two techniques for the storm with the largest

difference between the two. Temperature values calculated via the bin-averaging

technique (blue) are lower than those generated from whole-orbit technique (green) for

this storm and all storms in the sample.

Bin-Averaging Technique

| 3-Degree Latitude Bin ρ, H | → | Generate $T_\infty(\rho, H)$ via J77 for each Latitude Bin | → | Average T_∞ Over Each Orbit | → | Output $\bar{T}_\infty$ |

Whole-Orbit Technique

| 3-Degree Latitude Bin ρ, H | → | Average ρ, H Over Each Orbit | → | Generate $\bar{T}_\infty(\bar{\rho}, \bar{H})$ via J77 for each orbit | → | Output $\bar{T}_\infty$ |
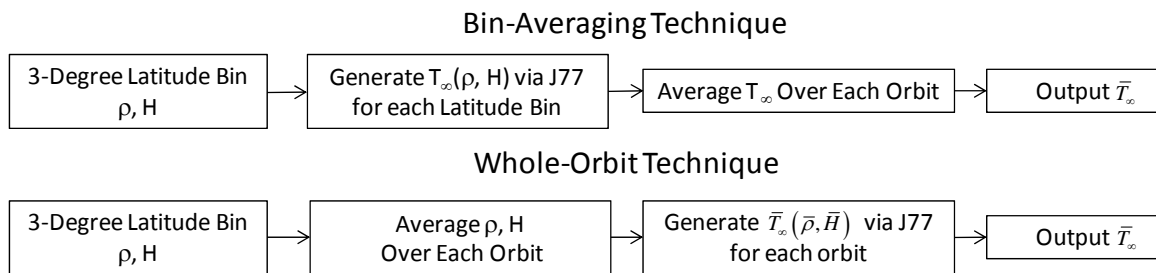
Figure 37: Diagram outlining two different orbit-averaging techniques. ρ is the mass density, H is the height above sea level, and T_∞ is the exospheric temperature. Orbit-average values are indicated by $\bar{\rho}, \bar{H}$, and $\bar{T}_\infty$.
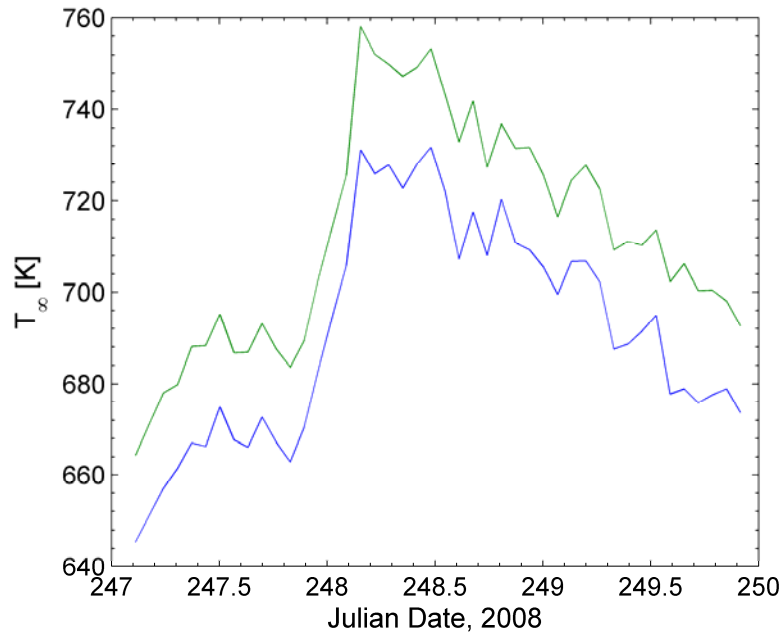
Figure 38: Orbit-Average exospheric temperature as a function of Julian Date, 2008. T_∞ values calculated via bin-averaging are shown in blue. T_∞ values calculated via the whole-orbit technique are shown in green.

Ideally, to ensure consistency, the bin-averaging technique would be applied to calculated model orbit-averaged densities from modeled $T_{1/2}$ values. This would require calculation of a model density in each latitude bin and then the results would be averaged over entire orbits. As discussed in section III, the current model is not formulated to accurately produce exospheric temperatures in specific latitude bins. Therefore, it is not meaningful to apply the bin-averaging technique to produce orbit-averaged model densities. Instead, the whole-orbit technique is used to calculate model orbit-averaged densities from model orbit-averaged T_∞ and observed orbit-averaged height values.

The result of this mixing of techniques is a built-in model density error caused by the difference between the two techniques. If the model performed perfectly and

96

produced model $T_{1/2}$ values equivalent to the observed $T_{1/2}$ values calculated using the

bin-averaging technique, the orbit-average model densities resulting from the whole-orbit

technique would be lower than the observed orbit-averaged densities. Since the difference

between the T_{∞} produced by the two techniques is small for most storms, the resulting

density errors are not contaminated significantly. However, for two of the outlier storms

(JD 86, 2008 and JD 247, 2008) the relative T_{∞} RMS difference between the two

techniques was greater than 2.4% resulting in model density values that were

significantly lower than the observed values despite the fact that the $T_{1/2}$ errors for these

storms were quite small.

The third outlier (JD 351, 2007) had a relatively small difference between

exospheric temperatures calculated with the two different orbit averaging techniques

which suggests that there is another factor influencing the density errors for outlier

storms. All of the outlier storms fell at the end of the sample period, at the end of 2007

and into 2008. This matches the time period of the last solar minimum (solar cycle

23/24), which was centered in November, 2008 (Emmert, et al., 2010). EUV flux and

thermospheric density during the last solar min were markedly lower than all five other

solar mins observed since the start of the space age (Solomon et al., 2010). This is likely

to impact the driven-dissipative model because it is based on the J77 model, which was

built using fits to observed data from satellite drag measurements. In addition, the driven-

dissipative model accounts for EUV flux by using the $F_{10.7}$ index. During the last solar

min, observed EUV flux decreased by 15% compared with averages from the previous

five solar mins while $F_{10.7}$ values were only down by 5% (Chen et al., 2011). This

indicates a change in the relationship between $F_{10.7}$ and EUV flux which could impact the model through Equation (33).

Emmert, et al., 2010, studied whether the changes in thermospheric densities during the last solar min could be modeled by solely changing exospheric temperatures. A model density profile was constructed using a Bates-Walker diffusive equilibrium profile (Walker, 1965). This type of profile is similar to the one used in the J77 model. Perturbing exospheric temperature alone did not result in a model density profile which matched the average density profile observed in 2008 – 2009. Instead, changes to exospheric temperature and thermospheric composition were both needed to produce a model density profile which matched observations (Emmert, et al., 2010). This suggests that the driven-dissipative model, which only perturbs temperatures, will not perform well during the last solar min.

Emmert et al., 2010 found that the difference between observed thermospheric density departed from 1986 – 2007 climatology by more than 10% beginning in November, 2007. To eliminate the impact of the last solar min on model density results, all storms from November, 2007 through 2008 (shown as red x's in Figure 36) were discarded. This removed all outlier storms and resulted in the expected trend of increasing $T_{1/2}$ errors resulting in increasing density errors as shown by the blue dots in Figure 36.

After discarding storms during the last solar min density errors resulting from the driven-dissipative model compare favorably with HASDM. This is significant because the model results include the built-in error introduced by the difference between orbit-

averaging techniques. Table 10 shows the mean and standard deviation of the relative

density RMS errors for the 29 storms from the original sample, defined in Table 1,

occurring from 2002 – October, 2007. Results are shown for all storms and separated by

storm type for the optimal α and τ values as well as the all storms fit α and τ values and

the storm type (CME or CIR) fit α and τ values. The optimal and all storms fit mean

density errors of 11.18% and 18%, respectively, compare favorably with the mean

HASDM storm-time error of 17%. Optimal errors for the CME and CIR storms are also

well below HASDM errors. Density errors resulting from best fit α and τ values for CIR

storms are less than HASDM mean errors while for CMEs, best fit α and τ values result

in mean density errors slightly higher than mean HASDM storm-time errors.

Table 10: Relative Density RMS Error resulting from Best Fit α and τ Values for 29 storms from 2002 – October 2007

	All Storms		CME Storms		CIR Storms	
	Mean	Std Dev	Mean	Std Dev	Mean	Std Dev
Optimal α and τ	11.18%	3.52%	11.69%	2.72%	10.77%	4.10%
All Storms Fit α and τ	18.00%	9.78%	22.28%	11.96%	14.53%	5.96%
CME-Fit α and τ			20.23%	7.51%		
CIR-Fit α and τ					12.47%	5.23%

Figure 36, along with comparisons between mean $T_{1/2}$ errors shown in Table 4

and mean density errors shown in Table 10, illustrates that for any given storm density

errors are much higher than temperature errors. The increase in error is due to the fact

that small changes in temperature result in large changes in density within the J77 model.

Figure 39 shows the observed orbit-averaged density for the JD 204, 2004 CME (red

dots) along with model densities resulting from optimal α and τ values (green line), all

storm fit α and τ values (blue line), and CME fit α and τ values (black line). Similar to

the $T_{1/2}$ results shown for this storm in Figure 28, the all storm fit and CME fit α and τ

values result in densities that are lower than both observed and optimal model values for

the second and third peaks on JD 207 and 209. For this storm the observed orbit-average

densities range from 2.17 x 10^{-16} to 10.72 x 10^{-16} g/cm^3, an increase of 394%. In contrast,

observed orbit-average $T_{1/2}$ values for this storm, shown in Figure 28, range from 841.18

to 1124.4K, an increase of only 34%. In other words relatively small changes (or errors)

in temperature values result in large changes (or errors) in density values. This sensitivity

explains the difference between model temperature and model density errors.
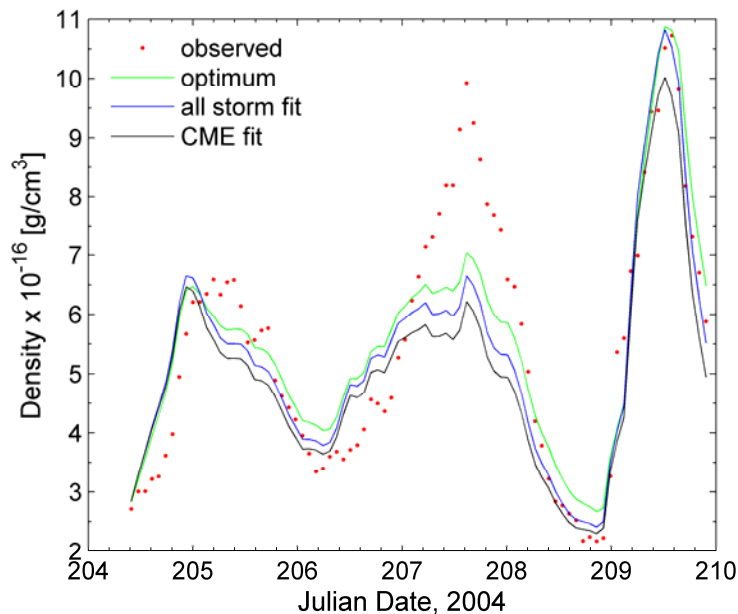
Figure 39: Model density results for the CME storm from Julian Date 204-210, 2004. Observed GRACE orbit-average density is shown by red dots, along with model density values resulting from optimal α and τ values (green line), all storm fit α and τ values (blue line), and CME fit α and τ values (black line).

100

Model density errors were also computed for the two test storms outside of the original sample, defined in Table 7. Table 11 shows the relative density RMS error resulting from optimal, all storm fit, and storm type (CME or CIR) fit α and τ values for these two storms. As expected, density errors are higher than $T_{1/2}$ errors but still low compared to the mean HASDM storm-time density error of 17%.

Table 11: Relative Density RMS Error resulting from Best Fit α and τ Values for Two Test Storms

	JD 308-309, 2003 CME	JD 42-45, 2004 CIR
Optimal	4.51%	6.20%
All Storms Fit	11.86%	15.38%
Storm Type Fit	8.19%	8.97%

V. Conclusions and Recommendations

Conclusions of Research

This project has produced conclusions in three main areas. First, the impact of the EUV term in the driven-dissipative model was explored. It was found that over the entire 38 storm sample, method three procedures (allowing both the time rate of change of $T_{1/2UV}$, $\frac{dT_{1/2UV}}{dt}$, and approximating $T_{1/2UV}(t) = T_{1/2}{}^{0}$) were on average slightly more accurate than methods one and two. Method three had a mean relative $T_{1/2}$ RMS error 1.84% compared to 2.04% and 2.03% for methods one and two, respectively. The impact of the treatment of the UV contribution was strongly dependent on the character of the change in $T_{1/2UV}$ over the storm period. Method three produced the smallest relative $T_{1/2}$ RMS error for 27 of the 28 storms in the sample that had decreasing $T_{1/2UV}$ profiles. In contrast method one, which treated $T_{1/2UV}$ as a constant, produced the smallest relative $T_{1/2}$ RMS error for seven of the 10 storms with increasing $T_{1/2UV}$ profiles. Method two, which allowed $\frac{dT_{1/2UV}}{dt}$ to vary but treated $T_{1/2}{}^{0}$ as a constant, produced results very similar to method one for all storms. In general, for the declining phase of the solar cycle, the full treatment of the UV contribution used in method three is the most accurate variation of the driven-dissipative model.

The second conclusion of this thesis is that the two empirical parameters in the driven-dissipative model exhibit solar cycle dependence and can be determined as quadratic functions of $\sqrt{F_{10.7a}}$, where the $F_{10.7a}$ value used is the value at the start of the storm period. This is important because it provides a way to determine model parameters

102

without any prior knowledge of the storm to be modeled. Using best-fit model parameters degraded model accuracy slightly, but the mean relative $T_{1/2}$ RMS error for all storms remained small at less than 3.2%. Around the minimum, relative $T_{1/2}$ RMS error is a shallow function of the model parameters allowing departures from the optimal values without significantly increasing errors. Model accuracy was improved slightly by separating storms by type (CME or CIR) and determining model parameters separately as functions of $\sqrt{F_{10.7a}}$ for each storm type. The general applicability of the model and the model parameter fits was established by applying them to two test storms outside the original sample of 38 which resulted in errors similar to those within the original sample.

The final conclusion of this research is that the driven-dissipative model, as formulated in method three, can be used in conjunction with the J77 model to produce model density values with accuracies similar to those currently produced by HASDM. Mean relative density RMS errors for the model averaged 11.18% when optimal model parameters were used and 18% when the model parameters determined by the all-storms fit functions of $\sqrt{F_{10.7a}}$ were used. These values compares favorably to HASDM's mean error of 17% during geomagnetic storming conditions. Of course the current formulation of the driven-dissipative model uses observed solar wind data as the driver, which helps produce accurate results. Still, the comparison with HASDM is significant because while the driven-dissipative model does not use observed density data to correct the model in near real-time as HASDM does, it is still able to produce comparable density errors. This suggests that future research could further improve the driven-dissipative model.

Recommendations for Future Research

In addition to producing several satisfying conclusions, this project suggests several promising avenues of future research. First, the set of 38 storms used in this thesis all occurred during the declining phase of the solar cycle from 2002-2008. Since the results indicate that the most accurate method of treating $T_{1/2UV}$ depends strongly on the character of the $T_{1/2UV}$ change over the storm period it would be useful to expand the storm sample to cover an entire solar cycle. This would likely result in a storm sample that is more evenly split between storms with increasing and decreasing $T_{1/2UV}$ changes and provide a more rigorous test of the three methods of treating $T_{1/2UV}$ used in this thesis. Currently, the ability to test storms over an entire solar cycle is limited by the availability of the GRACE data used as ground truth in the model.

A second avenue of research is related to the current formulation's use of the J77 model as a basis. The J77 model was used in the current formulation to be consistent with Burke's earlier work (2009, 2011). Current cutting edge models such as HASDM and JB08 are based on Jacchia's 1970 model instead of J77. This suggests that it may be useful to reformulate the driven-dissipative model to use J70 as a basis instead of J77. Doing this should provide two main advantages. First, it would allow experimentation with different formulas to account for the UV contribution to thermospheric temperature. Using the J70 model as a basis would allow the driven-dissipative model to easily use the J70, HASDM, or JB08 formulations for T_{0UV} which could result in improved accuracy. Second, using the J70 model as a basis could allow the method or the output from the driven-dissipative model to be integrated with HASDM and/or JB08 in order move from

a model temperature to a model density value. Doing so could eliminate the built-in error that results from the current model's method of converting from model $T_{1/2}$ to model density and also take advantage of the use of observed data in both HASDM and JB08 to improve accuracy.

A final recommendation for future research would be to move toward replacing the observed solar wind data used as a driver in the current formulation with input from a current solar wind model. While this would almost certainly degrade accuracy, it is necessary to make the driven-dissipative model useful in an operational sense. Determining how much the use of a model input changes the results would be important in assessing the potential of the driven-dissipative model for use in real-world forecasting applications.

Appendix A – Solar Declination Angle Calculation

This appendix outlines the procedure from Meeus, 1991 used to calculate the solar declination angle. All angle formulas presented here are in decimal degrees. Let Y denote the year of the data point, m the month number of the data point, and D the day of the month including decimals (for example the 5th day of the month at 12Z would mean $D = 5.5$). If $m \leq 2$, replace Y with Y-1 and m with m-2. Adopting the notation where INT( ) denotes the integer part of the argument within the parenthesis, the Julian date (JD) is calculated via the formula

$$JD = INT\left(365.25\left(Y + 4716\right)\right) + INT\left(30.6001\left(m+1\right)\right) + D + B - 1524.5 \tag{42}$$

Where B is given by:

$$B = 2 - A + INT\left(\frac{A}{4}\right)$$

with

$$A = INT\left(\frac{Y}{100}\right)$$

Next a time T is calculated.

$$T = \frac{JD - 2451545}{36525} \tag{43}$$

Using T the values for the geometric mean longitude of the sun (L_o), the mean anomaly of the sun (M), the longitude of the ascending mode of the Moon's mean orbit on the

ecliptic (Ω), the mean obliquity of the elliptic (ε_o), the mean longitude of the sun (L) and

the mean longitude of the Moon (L') are calculated in decimal degrees.

$$L_o = 280.46645 + 36000.76983T + 0.0003032T^2 \tag{44}$$

$$M = 357.5291 + 35999.0503T - 0.0001559T^2 - 0.00000048T^3 \tag{45}$$

$$\Omega = 125.04452 - 1934.136261T + 0.0020708T^2 + \frac{T^3}{450000} \tag{46}$$

$$\varepsilon_o = 23.439291111 - 0.0130041667T - 1.639 \times 10^{-7} T^2 + 5.036 \times 10^{-7} T^3 \tag{47}$$

$$L = 280.4665 + 36000.7698T \tag{48}$$

$$L' = 218.3165 + 481267.8813T \tag{49}$$

Using these values a true obliquity (ε) is calculated.

$$\varepsilon = \varepsilon_o + \Delta\varepsilon \tag{50}$$

Where $\Delta\varepsilon$, the nutation of the obliquity, is given by Equation (51).

107

$$\Delta\varepsilon = 2.5556\times10^{-3}\cos\left(\Omega\right)+1.5833\times10^{-4}\cos\left(2L\right)+...$$
$$2.7778\times10^{-5}\cos\left(2L'\right)-2.5\times10^{-5}\cos\left(2\Omega\right)$$

(51)

Next the sun's equation of center (C) is calculated based on the time T and the mean anomaly of the sun M

$$C = (1.914600 - 0.004817T - 0.000014T^2)\sin(M)+...$$
$$(0.019993 - 0.000101T)\sin(2M)+0.000290\sin(3M)$$

(52)

which leads to the sun's true longitude (Θ).

$$\Theta = L_o + C$$

(53)

Finally, the apparent longitude of the sun, λ, is calculated

$$\lambda = \Theta - 0.00569 - 0.00478\sin\left(\Omega\right)$$

(54)

leading to the solar declination angle (δ).

$$\delta = \sin^{-1}\left(\sin\left(\varepsilon\right)\sin(\lambda)\right)$$

(55)

Appendix B – The Nelder-Mead Simplex Direct Search Method

MATLAB's fminsearch function uses the Nelder-Mead simplex direct search method (Lagarias, et al., 1998) to minimize a given function by adjusting the specified variables. For this research the function to be minimized is the RMS error function given in Equation (39), denoted here as f(x) and the variables to be adjusted are the coupling constant, α, and the relaxation constant, τ, denoted here as the two element vector x. The number of elements in the vector x is denoted by n, here n=2. The algorithm is started by providing initial values of the vector x, denoted as x_o. Here the initial values were set at $\alpha_o = 44 \frac{K \cdot m}{hr \cdot mV}$ and $\tau_o = 5.4\ hrs$. To start the algorithm an initial simplex is created around x_o by adding 5% to each value of x_o one at a time, resulting in n+1 vectors defining the vertices of the initial simplex.

Once a simplex is defined, the vertices x_i are ordered based on their function value such that $f(x_1) < f(x_2) < \cdots < f(x_{n+1})$. During each step in the search iteration the worst point, x_{n+1}, is discarded and replaced by a new point via one of the methods outlined below. The iteration continues until the values of the cost function converge to a user-defined tolerance. For this research the tolerance was defined as 10^{-6}.

Reflection

A reflected point, x_r, is generated using the formula
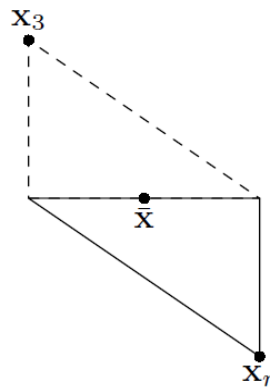
$$x_r = 2\overline{x} - x_{n+1} \tag{56}$$

where

$$\overline{x} = \frac{\sum_{i=1}^{n} x_i}{n} \qquad (57)$$

After the point x_r is generated the function value, $f(x_r)$, is calculated. If

$f(x_1) \leq f(x_r) < f(x_n)$ the point x_r is accepted to replace x_{n+1}, creating a new simplex,

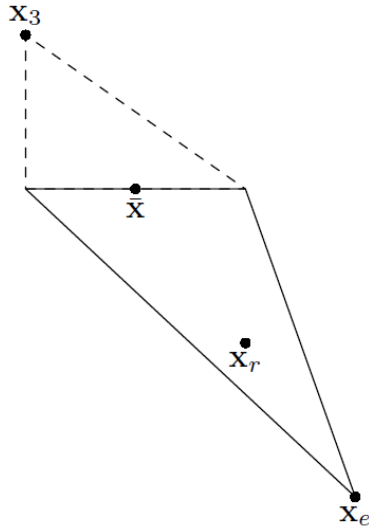and the iteration starts over. Figure 40 shows the simplices after a reflection step.

Figure 40: Nelder-Mead simplices after a reflection. The original simplex is shown with a dashed line (Lagarias, et al., 1998).

Expansion

If $f(x_r) < f(x_1)$ an expansion point, x_e, is calculated using the formula

$$x_e = \overline{x} + 2(\overline{x} - x_{n+1}) \qquad (58)$$

and the resulting function value $f(x_e)$ is calculated. If $(x_e) < f(x_r)$, the point x_e is

accepted to replace x_{n+1} and the iteration starts over. If $(x_e) > f(x_r)$, the point x_r is

accepted to replace x_{n+1} and the iteration starts over. Figure 41 shows the simplices after

an expansion step.

Figure 41: Nelder-Mead simplices after an expansion. The original simplex is shown with a dashed line (Lagarias, et al., 1998).

Contraction

If $f(x_r) \geq f(x_n)$, a contraction is performed between the point $\bar{x}$ and the point x_{n+1} or x_r that produces the lowest function value. If $f(x_r) < f(x_{n+1})$ an outside contraction is performed by calculating the point x_c

$$x_c = \bar{x} + \frac{(x_r - \bar{x})}{2} \tag{59}$$

and the resulting function value, $f(x_c)$. If $f(x_c) < f(x_r)$, the point x_c is accepted to replace x_{n+1} and the iteration starts over. If $f(x_c) \geq f(x_r)$, a shrink is performed using procedures in the next section. Figure 42 shows the simplices after an outside contraction.
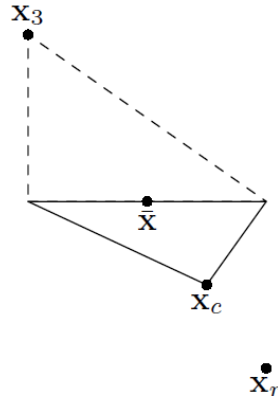
Figure 42: Nelder-Mead simplices after an outside contraction. The original simplex is shown with a dashed line (Lagarias, et al., 1998).

If $f(x_r) \geq f(x_{n+1})$ an inside contraction is performed by calculating the point x_{cc}

$$x_{cc} = \overline{x} + \frac{\left(x_{n+1} - \overline{x}\right)}{2} \tag{60}$$

and the resulting function value, $f(x_{cc})$. If $f(x_{cc}) < f(x_{n+1})$, the point x_{cc} is accepted to replace x_{n+1} and the iteration starts over. If $f(x_{cc}) \geq f(x_{n+1})$, a shrink is performed using procedures in the next section. Figure 43 shows the simplices after an inside contraction.
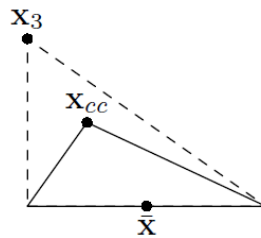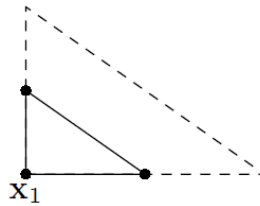

Figure 43: Nelder-Mead simplices after an inside contraction. The original simplex is shown with a dashed line (Lagarias, et al., 1998).

112

Shrink

If none of the previous methods used to identify a new point to replace x_{n+1} in a

the new simplex were successful a new simplex is calculated by performing a shrink

using the formula

$$v_i = x_1 + \frac{x_i - x_1}{2} \tag{61}$$

where i=2…n+1. The points are ordered by increasing values of $f(v_i)$ and the new

simplex is defined by the best point in the old simplex, x_1, along with the new values v_i

where again i = 2…n+1. Figure 44 shows the simplices after a shrink.

**Figure 44: Nelder-Mead simplices after a shrink. The original simplex is shown
with a dashed line (Lagarias, et al., 1998).**

Schematic

Figure 45 shows a schematic depicting the Nelder-Mead simplex direct search

method described above. The bold text in each box depicts the condition that must be

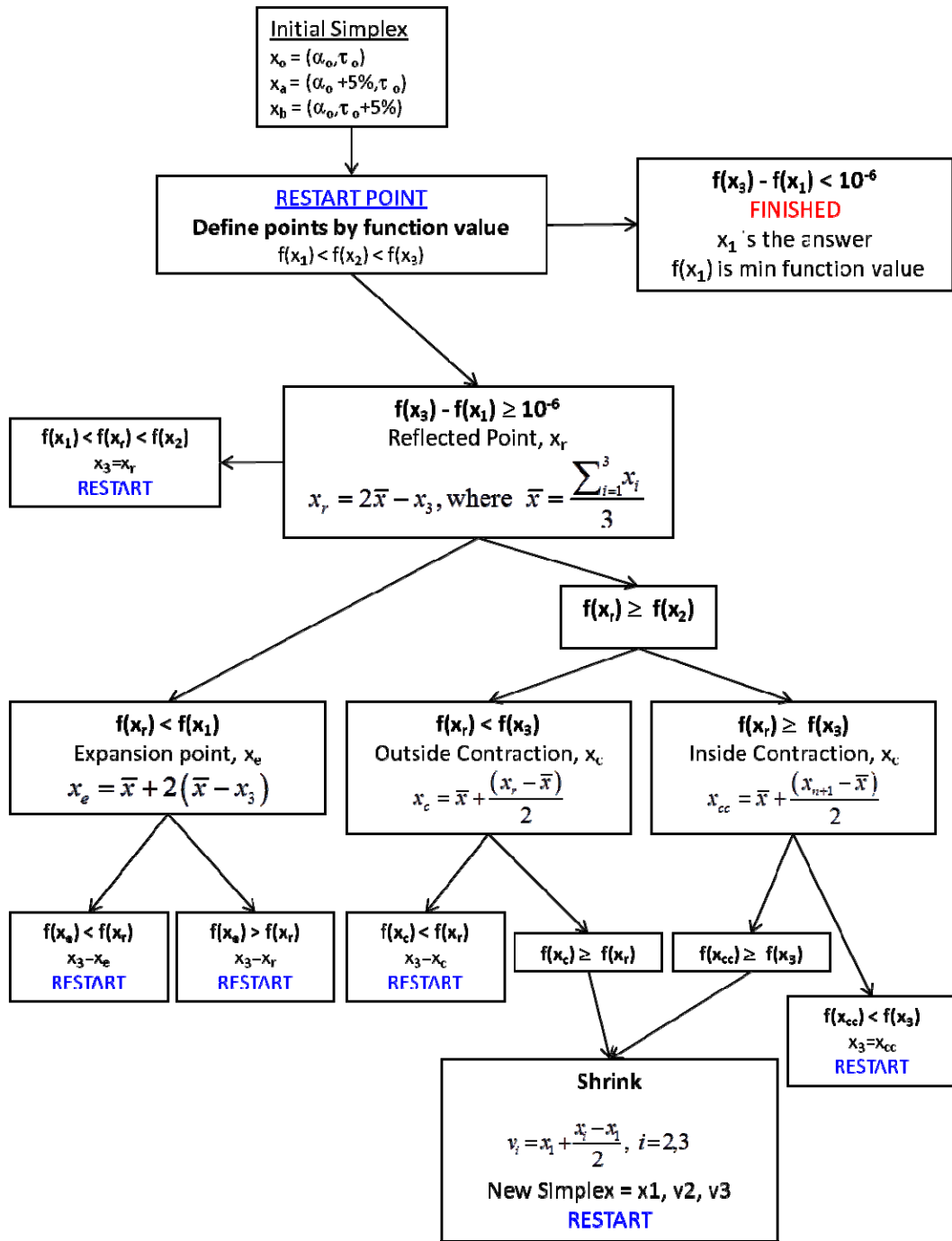satisfied in order to perform the action listed in the box.

Initial Simplex
$x_o = (\alpha_o, \tau_o)$
$x_a = (\alpha_o + 5\%, \tau_o)$
$x_b = (\alpha_o, \tau_o + 5\%)$

RESTART POINT
Define points by function value
$f(x_1) < f(x_2) < f(x_3)$

$f(x_3) - f(x_1) < 10^{-6}$
FINISHED
x_1 is the answer
$f(x_1)$ is min function value

$f(x_1) < f(x_r) < f(x_2)$
$x_3 = x_r$
RESTART

$f(x_3) - f(x_1) \geq 10^{-6}$
Reflected Point, x_r
$$x_r = 2\bar{x} - x_3, \text{where } \bar{x} = \frac{\sum_{i=1}^{3} x_i}{3}$$

$f(x_r) \geq f(x_2)$

$f(x_r) < f(x_1)$
Expansion point, x_e
$$x_e = \bar{x} + 2(\bar{x} - x_3)$$

$f(x_r) < f(x_3)$
Outside Contraction, x_c
$$x_c = \bar{x} + \frac{(x_r - \bar{x})}{2}$$

$f(x_r) \geq f(x_3)$
Inside Contraction, x_c
$$x_{cc} = \bar{x} + \frac{(x_{n+1} - \bar{x})}{2}$$

$f(x_e) < f(x_r)$
$x_3 = x_e$
RESTART

$f(x_e) > f(x_r)$
$x_3 = x_r$
RESTART

$f(x_c) < f(x_r)$
$x_3 = x_c$
RESTART

$f(x_c) \geq f(x_r)$

$f(x_{cc}) \geq f(x_3)$

$f(x_{cc}) < f(x_3)$
$x_3 = x_{cc}$
RESTART

Shrink
$$v_i = x_1 + \frac{x_i - x_1}{2}, \; i = 2,3$$
New Simplex = x1, v2, v3
RESTART

Figure 45: Schematic of the Nelder-Mead simplex direct search method used by MATLAB's fminsearch function, described by (Lagarias, et al., 1998). Schematic is shown for a function of 2 variables, as used in this thesis. The bold text in each box depicts the condition that must be satisfied in order to perform the action listed in the box.

Bibliography

Bailey, S. M., Barth, C. A., and Solomon, S. C. "A Model of Nitric Oxide in the Lower Thermosphere," *Journal of Geophysical Research*, 107: 1205 (2002).

Borovsky, J. E., and Denton, M. H. "Differences Between CME-Driven Storms and CIR-Driven storms," *Journal of Geophysical Research*, 111: A07S08 (2006).

Boudouridis, A., Zesta, E., Lyons, L., and Anderson, P. "Evaluation of the Hill-Siscoe Transpolar Potential Saturation Model during a Solar Wind Dynamic Pressure Pulse," *Geophysical Research Letters*, 31: L23802 (2004).

Bowman, B. R., Tobiska, W. K., Marcos, F. A., Huang, C. Y., Lin, C. S., and Burke, W. J. "A New Empirical Thermospheric Density Model JB2008 Using New Solar and Geomagnetic Indices," *AIAA/AAS Astrodynamics Specialist Conference*, Honolulu, Hawaii: American Institute of Aeronautics and Astronautics, p. 6438, (2008).

Bruinsma, S., and Biancale, R. "Total Densities Derived from Accelerometer Data," *Journal of Spacecraft and Rockets*, 40: 230-236 (2003).

Bruinsma, S., Forbes, J. M., Nerem, R. S., and Zhang, X. "Thermosphereic Density Response to the 20-21 November 2003 Solar and Geomagnetic Storm From CHAMP and GRACE Accelerometer Data," *Journal of Geophysical Research*, 111: A06303 (2006).

Bruinsma, S., Tamagnan, D., and Biancale, R. "Atmospheric Densities Derived from CHAMP/STAR Accelerometer Observations," *Planetary Space Science*, 52: 297-312 (2004).

Burke, W. J. "Penetration Electric Fields: A Volland-Stern Approach," *Journal of Atmospheric, Solar, and Terrestrial Physics*, 69: 1114-1126 (2007).

Burke, W. J. "Solar Cycle Dependence of Solar Wind Energy Coupling to The Thermosphere," *Journal of Geophysical Research*, 116: A06302 (2011).

Burke, W. J. (2008). "Stormtime Energy Budgets of the Global Thermosphere," in *Mid-Latitude Ionospheric Dynamics and Disturbances*. Ed. P. Kintner. Washington, D.C.: American Geophysical Union, Vol. 181, pp. 235-246 (2008).

Burke, W. J., Gentile, L. C., and Hagan, M. P. "Thermospheric Heating by High-Speed Streams in the Solar Wind," *Journal of Geophysical Research*, 115: A06318 (2010).

Burke, W. J., Lin, C. S., Hagan, M. P., Huang, C. Y., Weimer, D. R., Wise, J. O., et al. "Storm Time Global Thermosphere: A Driven-Dissipative Thermodynamic System," *Journal of Geophysical Research*, 114: A06306 (2009).

Burke, W., Weimer, D. R., and Maynard, N. "Geoeffective Interplanetary Scale Sizes Derived from Regression Analysis of Polar Cap Potentials," *Journal of Geophysical Research*, 104: 9989-9994 (1999).

Burton, R. K., McPherron, R. L., and Russell, C. "An Empirical Relationship between Interplanetary Conditions and Dst," *Journal of Geophysical Research*, 80, 4204 (1975).

Chen, Y., Liu, L., and Wan, W. "Does the $F_{10.7}$ Index Correctly Describe Solar EUV Flux during the Deep Solar Minimum of 2007-2009?" *Journal of Geophysical Research*, 116, A04304 (2011).

Ejiri, M. "Trajectory Traces of Charged Particles in the Magnetosphere," *Journal of Geophysical Research*, 83: 4798 (1978).

Emmert, J. T., Lean, J. L., and Picone, J. M. "Record-Low Thermospheric Density during the 2008 Solar Minimum," *Geophysical Research Letters*, 37, L12102 (2010).

Helmholtz Centre Potsdam GFZ, "Indices of Global Geomagnetic Activity: Kp Sites List," Retrieved 24 Sep, 2012, from http://www-app3.gfz-potsdam.de/kp_index/kp_sites.html

Hill, T. W. "Magnetic Coupling between Solar Wind and Magnetosphere: Regulated by Ionospheric Conductance?" *EOS Transactions American Geophysical Union,* 65: 1047 (1984).

Hill, T. W., Dessler, A. J., and Wolf, R. A. "Mercury and Mars: The Role of Ionospheric Conductivity in the Acceleration of Magnetospheric Particles," *Geophysical Research Letters*, 3: 429-432 (1976).

Huang, C. Y., and Burke, W. J. "Transient Sheets of Field-Aligned Current Observed by DMSP during the Main Phase of a Magnetic Superstorm," *Journal of Geophysical Research*, 109: A06303 (2004).

Jacchia, L. G. "New Static Models of the Thermosphere and Exosphere with Empirical Temperature Profiles," *Smithsonian Astrophysical Observatory Special Report*, 313: 1-88 (1970).

Jacchia, L. G. "Thermospheric Temperature, Density, and Composition: New Models," *Smithsonian Astrophysical Observatory Special Report*, 375 (1977).

Kennel, C. F. *Convection and Substorms: Paradgims of Magnetospheric Phenomenology*. New York: Oxford University Press, 1995.

Knecht, D. J., and Shuman, B. M. "The Geomagnetic Field." In *Handbook of Geophysics and Space Environment* (pp. 4-1 - 4-37). Hanscom AFB, MA: Air Force Research Laboratory, 1985.

Knipp, D. J., Tobiska, W. K., and Emery, B. A. "Direct and Indirect Thermospheric Heating Sources from Solar Cycles 21-23," *Solar Physics*, 224: 495-505 (2004).

Lagarias, J. C., Reeds, J. A., Wright, M. H., and Wright, P. E. "Convergence Properties of the Nelder Mead Simplex Method in Low Dimensions," *SIAM Journal of Optimization*, 9: 112-147 (1998).

Lei, J., Thayer, J. P., Forbes, J. M., Sutton, E. K., and Nerem, R. S. "Rotating Solar Coronal Holes and Periodic Modulation of the Upper Atmosphere," *Geophysical Research Letters*, 35: L10109 (2008).

Lu, G., Baker, D. N., McPherron, R. L., Farrugia, C. J., Lummerzheim, D., Ruohoniemi, J. M., et al. "Global Energy Deposition during the January 1997 Magnetic Cloud Event," *Journal of Geophysical Research*, 103: 11685-11694 (1998).

Marcos, F. A., Burke, W. J., and Lai, S. T. "Thermospheric Space Weather Modeling," *38th AIAA Plasmadynamics and Lasers Conference*: Miami, FL (2007).

Marcos, F. A., Huang, C. Y., Lin, C. S., Retterer, J. M., and Delay, S. H. "Evaluation of Recent Thermospheric Neutral Density Models," Kirtland AFB, NM: Air Force Research Laboratory (2010).

Meeus, J. *Astronomical Algorithms.* Richmond, VA: Willmann-Bell Inc., 1991.

Mlynczak, M. G., Martin-Torres, F. J., Crowley, G., Kratz, D. P., Funke, B., Lu, G., et al. "Energy Transport in the Thermosphere during the Solar Storms of April 2002," *Journal of Geophysical Research* , 110: A12S25 (2005).

Mueller, S., Luhr, H., and Rentz, S. "Solar and Magnetospheric Forcing of the Low Latitude Thermospheric Mass Density as Observed By CHAMP," *Annuls of Geophysics*, 27: 2087-2099 (2009).

Mursula, K., and Zeiger, B. "The 13.5-Day Periodicity in the Sun, Solar Wind, and Geomagnetic Activity: The Last Three Solar Cycles," *Journal of Geophysical Research*, 101: 27077 (1996).

NASA. NASA OMNIWeb. Retrieved 8 August, 2012 from High Resolution Omni: http://omniweb.gsfc.nasa.gov/form/omni_min.html

Owens, J. K., Vaughan, W. W., Niehuss, K. O., and Minow, J. "Space Weather, Earth's Neutral Upper Atmosphere (Thermosphere), and Spacecraft Orbital Lifetime/Dynamics," *IEEE Transactions on Plasma Science*, 28: 1920-1930 (2000).

Paetzold, H. K., and Zschorner, H. "An Annual and a Semiannual Variation of the Upper Air Density," *Pure Applied Geophysics*, 48: 85-92 (1961).

Pawlowski, D. J., and Ridley, A. J. "Modeling the Thermospheric Response to Solar Flares," *Journal of Geophysical Research*, 113: A10309 (2008).

Press, W. H., Teukolsky, S. A., Vetterling, W. T., and Flannery, B. P. *Numerical Recipes: The Art of Scientific Computing* (3rd Edition). Cambridge: Cambridge University Press, 2008.

Prölss, G. W. *Physics of the Earth's Space Environment: An Introduction*. Berlin: Springer-Verlag, 2004.

Qian, L., and Solomon, S. C.. "Thermospheric Density: An Overview of Temporal and Spatial Variations," *Space Science Review*, (August, 2011).

Robinson, R. M., and Vondrak, R. R. "Measurements of the E Region Ionization and Conductivity Produced by Solar Illumination at High Latitudes," *Journal of Geophysical Research*, 89: 3951-3956 (1984).

Schunk, R. W., and Nagy, A. F. *Ionospheres: Physics, Plasma Physics, and Chemistry*. Cambridge, England: Cambridge University Press, 2009.

Sharma, R. D., Dothe, H., Von Esse, F., Kharchenko, V. A., Sun, Y., and Dalgarno, A. "Production of Vibrationally and Rotationally Excited NO in the Night Time

Terrestrial Thermosphere," *Journal of Geophysical Research*, 101: 19707-19713 (1996).

Siscoe, G. L., M., E. G., Sonnerup, B. U., Maynard, N. C., Schoendorf, K. D., Siebert, K. D., et al. "Hill Model of Transpolar Potential Saturation: Comparison with MHD Simulation," *Journal of Geophysical Research*, 107: 1075 (2002).

Solomon, S. C., Woods, T. N., Didkovsky, L. V., Emmert, J. T., and Qian, L. "Anomalously Low Solar Extreme-Ultraviolet Irradiance and Thermospheric Density during Solar Mimimum", *Geophysical Research Letters*, 37, L16103 (2010).

Sonnerup, B. U. "Magnetopause Reconnection Rate," *Journal of Geophysical Research*, 79: 1546 (1974).

Storz, M. F., Bowman, B. R., Branson, J. I., Casali, S. J., and Tobiska, W. K. "High Accuracy Satellite Drag Model (HASDM)," *Advances in Space Research*, 36: 2497-2505 (2005).

Sutton, E. K. *Accelerometer-Derived Atmospheric Densities from the CHAMP and GRACE Satellites: Version 2.3*, AFRL Technical Memo; DTIC # ADA537198, 2011

Tapley, B. D., Bettadpur, S., Watkins, M., and Reigber, C. "The Gravity Recovery and Climate Experiment: Mission Overview and Early Results," *Geophysical Research Letters*, 31: L09607 (2004).

Tascione, T. F. *Introduction to the Space Environment* (2nd Edition). Malabar, Florida: Krieger Publishing Company, 1994.

Temmer, M., Vrsnak, B., and Veronig, A. M. "Periodic Appearance of Coronal Holes and the Related Variation of Solar Wind Parameters," *Solar Physics*, 241: 371-383 (2007).

Thayer, J. P., and Semeter, J. "The Convergence of Magnetospheric Energy Flux in the Polar Atmosphere." *Journal of Atmospheric and Solar-Terrestrial Physics*, 66: 807-824 (2004).

Tobiska, W. K., Woods, T., Eparvier, F., Viereck, R., Floyd, L., Bouwer, D., et al. "The SOLAR2000 Empirical Solar Irradiance Model and Forecast Tool," *Journal of Atmospheric and Solar-Terrestrial Physics*, 62: 1233-1250 (2000).

Walker, J. C. G. "Analytic Represenation of Upper Atmosphere Densities Based on Jacchia's Static Diffusion Models," *Journal of Atmospheric Sciences*, 22, 462-463 (1965).

Webb, D. F. "The Solar Cycle Variation of the Rates of CMEs and Related Activity," *Advanced Space Research*, 11: 37 (1991).

Weimer, D. R. "Improved Ionospheric Electrodynamic Models and Application to Calculating Joule Heating Rates," *Journal of Geophysical Research*, 110: A05306 (2005).

Weimer, D. R., Bowmann, B. R., Sutton, E. K., and Tobiska, W. K. "Predicting Global Average Thermospheric Temperature Changes Resulting from Auroral Heating," *Journal of Geophysical Research*, 116: A01312 (2011).

Wilson, G. R., Weimer, D. R., Wise, J. O., and Marcos, F. A. "Response of the thermosphere to Joule heating and particle precipitation," *Journal of Geophysical Research*, 111: A10314 (2006).

Wise, J. O., Burke, W. J., and Sutton, E. K. "Globally Averaged Exospheric Temperatures Derived from CHAMP and GRACE Accelerometer Measurements," *Journal of Geophysical Research*, 117: A04312 (2012).

Wright, D. "Space Debris," *Physics Today*, 60: 35-40 (2007).

Vita

Captain William R. Frey graduated as valedictorian from Saint Mary's Central Catholic High School in Sandusky, Ohio. He entered the University of Michigan in Ann Arbor, Michigan where he graduated Summa Cum Laude with a Bachelor of Science degree in Atmospheric, Oceanic and Space Sciences in April, 2005. Upon graduation he was commissioned as a Second Lieutenant in the USAF through AFROTC Detachment 390 at the University of Michigan. His first assignment was to the 15th Operational Weather Squadron, Scott Air Force Base, Illinois where he served as Lead Forecaster and Flight Commander. In August, 2008 he was assigned to the 100th Operations Support Squadron, RAF Mildenhall, England as staff weather officer and, later, weather Flight Commander. While stationed at RAF Mildenhall, he earned a Master of Arts degree in International Relations from the University of Oklahoma and deployed in support of Operation Enduring Freedom to Al Udeid Air Base, Qatar as the weather Flight Commander for the 379th Expeditionary Operations Support Squadron. In May, 2011, he entered the Graduate School of Engineering and Management, Air Force Institute of Technology. Upon graduation, he will be assigned as the Air Force Weather Agency's Chief Liaison Officer to the National Oceanic and Atmospheric Administration's Space Weather Prediction Center in Boulder, Colorado.

REPORT DOCUMENTATION PAGE

1. REPORT DATE *(DD-MM-YYYY)* 21-03-2013	2. REPORT TYPE Master's Thesis	3. DATES COVERED *(From – To)* Mar 2012 – Mar 2013

4. TITLE AND SUBTITLE	5a. CONTRACT NUMBER
Modeling the Thermosphere as a Driven-Dissipative Thermodynamic System	
	5b. GRANT NUMBER
	5c. PROGRAM ELEMENT NUMBER
6. AUTHOR(S)	5d. PROJECT NUMBER N/A
Frey, William R., Captain, USAF	5e. TASK NUMBER
	5f. WORK UNIT NUMBER

7. PERFORMING ORGANIZATION NAMES(S) AND ADDRESS(S)	8. PERFORMING ORGANIZATION REPORT NUMBER
Air Force Institute of Technology Graduate School of Engineering and Management (AFIT/EN) 2950 Hobson Way, Building 640 WPAFB OH 45433-7765	AFIT-ENP-13-M-11

9. SPONSORING/MONITORING AGENCY NAME(S) AND ADDRESS(ES)		10. SPONSOR/MONITOR'S ACRONYM(S) AFRL/RVBXI , AFWA
Air Force Research Laboratory, RVBXI Chin S. Lin, PhD 3550 Aberdeen Ave SE Kirtland AFB, NM 87117 (505)-846-7803, DSN 246-7803 Chin.Lin@kirtland.af.mil	Air Force Weather Agency Robb Randal, Lt Col, PhD, USAF 101 Nelson Drive Offutt AFB, NE 68113-4020 (402)-294-9747, DSN 271-9747 robb.randall@offutt.af.mil	11. SPONSOR/MONITOR'S REPORT NUMBER(S)

12. DISTRIBUTION/AVAILABILITY STATEMENT
DISTRIBUTION STATEMENT A: APPROVED FOR PUBLIC RELEASE; DISTRIBUTION UNLIMITED.

13. SUPPLEMENTARY NOTES
This material is declared a work of the U.S. Government and is not subject to copyright protection in the United States.

14. ABSTRACT

Thermospheric density impacts satellite position and lifetime through atmospheric drag. More accurate specification of thermospheric temperature, a key input to current models such as the High Accuracy Satellite Drag Model (HASDM), can decrease model density errors. Building on Burke et al.'s driven-dissipative model (2009) the arithmetic mean temperature, $T_{1/2}$, defined by Jacchia, 1977 (J77), is modeled using the magnetospheric electric field as a driver. Three methods of treating the UV contribution to $T_{1/2}$ ($T_{1/2\,UV}$) are tested. Two model parameters, the coupling and relaxation constants, are adjusted for 38 storms from 2002 - 2008 to minimize modeled $T_{1/2}$ errors. Observed $T_{1/2}$ values are derived from densities and heights measured by the GRACE satellite. It is found that allowing $T_{1/2\,UV}$ to vary produces the lowest errors for 27 of 38 storms in the sample and 27 of 28 storms with decreasing UV contributions. Treating $T_{1/2UV}$ as a constant produces the lowest errors for 7 of 10 storms with increasing UV contributions. The coupling and relaxation constants are fit well as quadratic functions of $\sqrt{F_{10.7a}}$. By using the J77 model to convert the model $T_{1/2}$ to density values, the driven-dissipative model produces density errors slightly lower than HASDM storm time errors.

15. SUBJECT TERMS
Thermosphere, Geomagnetic Storm, Satellite Drag, Solar Wind

16. SECURITY CLASSIFICATION OF:			17. LIMITATION OF ABSTRACT	18. NUMBER OF PAGES	19a. NAME OF RESPONSIBLE PERSON Capt Matthew B. Garvin, PhD (ENP)
a. REPORT U	b. ABSTRACT U	c. THIS PAGE U	UU	135	19b. TELEPHONE NUMBER *(Include area code)* (937) 255-6565, x 4693 (matthew.garvin@afit.edu)